PHD

Structural Health Monitoring Systems for Impacted Isotropic and Anisotropic Structures

Ciampa, Francesco

Award date:
2012

Awarding institution:
University of Bath

Structural Health Monitoring Systems for Impacted Isotropic and Anisotropic Structures

Francesco Ciampa

Department of Mechanical Engineering

University of Bath

Thesis submitted as partial fulfilment for

the degree of Doctor of Philosophy

May 2012

Non aetate verum ingenio apiscitur sapientia
"Not by age but by capacity is wisdom acquired"
Titus Maccius Plautus, Trinummus,
Roman comic dramatist (254 BC - 184 BC)

Acknowledgements

First of all, I would like to express my gratitude to Dr. Michele Meo for suggesting the following work and serving as my graduate advisor over the past three years. I appreciate very much his contributions of time, ideas, and enthusiastic encouragement to make my PhD experience productive and stimulating. Especially his insight into cross-disciplinary research and his insistence of pursuing excellence have influenced me greatly, and surely my future academic career will benefit much from it.

I gratefully acknowledge the funding sources that made my PhD work possible. I was funded by Airbus UK and I would like to thank Dr. Christophe Paget for his superb guidance, support and generosity in meeting with me to discuss various aspects of my research. My work was also supported by Great Western Research.

I am truly grateful toward all the people at the University of Bath that contributed with their expertise and work to the realisation of this research, but also for their invaluable humour and friendship. In particular, I would like to thank all of my colleagues: Francesco Amerini, Ettore Barbieri, Fulvio Pinto, Umberto Polimeno, Stefano Angioni, Tieman Postma, Amit Visrolia, Gian-Piero Malfense Fierro, Simon Pickering, Giovanni de Angelis and Mikael Amura. I would also like to acknowledge Andrea Marini for his encouragement and advisory support during my research.

My time life in Bath was made brighter and more colourful in large part due to the many friends and groups that became a part of my life. I am grateful for time spent with roommates and friends, but also for many other people and memories.

Lastly, but not least, this thesis is dedicated to my lovely wife Erika

and my parents. They have been a constant source of love, concern, support and strength during all these years. Thank you.

Abstract

This thesis investigates the development of ultrasonic Structural Health Monitoring (SHM) systems, based on guided waves propagation, for the localization of low-velocity impacts and the detection of damage mechanisms in isotropic and anisotropic structures. For the identification of the impact point, two main *passive* techniques were developed, an *algorithm-based* and an *imaging-based* method. The former approach is based on the differences of the stress waves measured by a network of piezoelectric transducers surface bonded on plate-like structures. In particular, four piezoelectric sensors were used to measure the antisymmetrical A_0 Lamb mode in isotropic materials, whilst six acoustic emission sensors were employed to record the wave packets in composite laminates. A joint time-frequency analysis based on the magnitude of the Continuous Wavelet Transform was used to determine the time of arrivals of the wave packets. Then, a combination of unconstrained optimization technique associated to a local Newton's iterative method was employed to solve a system of non linear equations, in order to assess the impact location coordinates and the wave group speeds. The main advantages of the proposed algorithms are that they do not require an *a-priori* estimation of the group velocity and the mechanical properties of the isotropic and anisotropic structures. Moreover, these algorithms proved to be very robust since they were able to converge from almost any guess point and required little computational time. In addition, this research provided a comparison between the theoretical and experimental results, showing that the impact source location and the wave velocity were predicted with reasonable accuracy.

The *passive imaging-based* method was developed to detect in real-time the impact source in reverberant complex composite structures using only one passive sensor. This technique is based on the *reciprocal time reversal approach*, applied to a number of waveforms stored in a database containing the impulse responses of the structure. The proposed method allows achieving the optimal focalization of the acoustic emission source (impact event) as it overcomes the limitations of other ultrasonic impact localization techniques. Compared to a simple *time reversal process*, the robustness of this approach is experimentally demonstrated on a stiffened composite plate.

This thesis also extended *active* ultrasonic guided wave methods to the specific case of dissipative structures showing non-classical nonlinear behaviour. Indeed, an imaging method of the nonlinear signature due to impact damage in a reverberant complex anisotropic medium was developed. A novel technique called *phase symmetry analysis*, together with frequency modulated excitation signals, was used to characterize the third order nonlinearity of the structure by exploiting its invariant properties with the phase angle of the input waveforms. Then, a "virtual" reciprocal time reversal imaging process was employed to focus the elastic waves on the defect, by taking advantage of multiple linear scattering. Finally, the main characteristics of this technique were experimentally validated.

Contents

List of Figures

List of Tables

Chapter 1

Introduction

1.1 Structural Health Monitoring Systems

The integrity of structural components is conventionally performed through a wide variety of classical Non Destructive Evaluation (NDE) techniques. Some of these, including eddy currents, shearography, thermography, liquid penetrant, radiography and ultrasounds, require a detailed inspection of the system components, and most of the time the assessment of the defect is not so quick and easy to obtain. With the growing interest to use laminar composite materials in aerospace structures, much attention is devoted to the development of rapid, accurate and cost-effective *built-in* systems for the detection and evaluation of structural defects. Unlike metallic media, which are homogeneous and dissipate energy through yielding, carbon fibre reinforced plastic (CFRP) structures are relatively brittle and exhibit weak interfacial strength between laminas. Damages can be often imparted by a wide range of sources including unanticipated discrete events such as dropped tools, hail, runway debris during takeoff and landing etc... These events, resulting in a large range of possible impact velocity, mass and impactor geometry, not only weaken the structure undergone to a continuous service load, but also may generate different types of flaws before full perforation (i.e. sub-surface delamination, matrix cracking, fibre debonding or fracture, indentation and barely visible impact damage). Over time, these effects can induce variations in the mechanical properties of the laminate (the primary

Inspection time	**Current inspection time** (% of total)	**Estimated potential for smart systems**	**Time saved** (% of total)
Flight time	16	0.40	6.5
Scheduled	31	0.45	14
Unscheduled	16	0.10	1.5
Service instructions	37	0.6	22

Table 1.1: Estimated time saved on inspection operations by the use of SHM, from Balageas *et al.* [2006]

effect of a delamination is to change the local value of the bending stiffness and of the transverse-shear stiffness), leading to possible catastrophic failure conditions. In addition, NDE techniques require the structure to be disassembled during the inspections and this may cause disruptions and a considerable raise of the costs of maintenance. Hence, these methods are inadequate for real-time monitoring systems.

In the last decade, Structural Health Monitoring (SHM) systems based on guided waves were developed to provide an early warning of the damage occurrence, resulting into safer structures and operative costs saving (Chang [1999]). SHM has a common basis with NDE, in fact several NDE methods can be converted in SHM techniques by integrating sensors and actuators inside the monitored structure. For instance, traditional ultrasonic testing can be converted in acoustic/ultrasonic SHM systems, by simply using embedded or surface mounted piezoelectric patches. Essentially, a SHM sensing system is composed of a network of sensors or probes that guarantee a continuous remote monitoring aimed to:

- provide a fast, cost-effective and *in-situ* diagnosis of the safety condition of the structure through sensor and actuator data
- access the location and a quantification of the degree of damage
- investigate large areas, even in poorly accessible critical locations, without the need to remove the structure from service
- minimize the human involvement, thus reducing maintenance downtime and human errors.

Furthermore, a reliable, quick and fully integrated SHM technique mounted on in-service structures, ensure a considerable reduction either in the effective cost of maintenance or in the time for which the aircraft is out of service. In fact, as reported in Balageas *et al.* [2006], a recent study on inspection requirements for a modern aircraft revealed that an estimated 40% or more could be saved on inspection time through the introduction of SHM systems (Tab. 1.1).

1.2 Overview

This research was aimed at developing *in-situ* SHM systems for the localization of low-velocity impacts and the assessment of structural damages in isotropic and anisotropic materials. In particular, the methodologies presented in this thesis will be used to answer the following questions:

1. *Where is the impact location?*
2. *What are the effects of the impact on the structure?*

In order to answer the first question, two different techniques were carried out and validated to estimate the location of the impact source, i.e. an "*algorithm-based*" method used for plate-like structures and an "*imaging-based*" method employed for geometrically complex panels. The former approach consists in an inverse problem that relies on the *time of arrival* (TOA) estimation and the group velocity recognition of the ballistic waves (direct waves from the source to the receiver) recorded by a network of passive acoustic emission transducers. In such method, the waveforms are analysed with advanced signal processing techniques (*Continuous Wavelet Transform*) and then an optimization algorithm is employed to obtain the impact coordinates. The main outcome of the "*algorithm-based*" technique was to overcome the limitations of other impact localization methods, as it is able to satisfy the following requirements:

- it can be used for both isotropic and anisotropic structures as it does not require *a-priori* knowledge of the mechanical properties, thickness, as well as lay-up and anisotropic angular-group velocity pattern of the recorded waveforms

- it exhibits a suitable time-frequency analysis for the TOA identification
- it provides a flexible trade-off in terms of efficiency and accuracy as it is able to identify the impact source in real-time requiring little computational time

The "*imaging-based*" impact localization approach relies on the *time reversal* (TR) and *reciprocal time reversal* methods, wherein a propagating waveform can be focused back on the original source if the output received by a set of transducers is time-reversed and emitted back to the excitation point. Compared to conventional imaging SHM systems, the most significant improvements of the time reversal technique are:

- it does not require any iterative algorithms as well as a priori knowledge of the mechanical properties and the anisotropic group speed and it is suitable for locating the impact source in geometrically complex structures.
- it exploits the "benefits" of multimodal conversion and scattering effects to obtain the optimal refocusing at the impact location using only **one** receiver transducer
- it reduces signal processing requirements as it does not need to estimate the TOA of the ballistic waves

Furthermore, in order to answer the second question, an imaging method of the nonlinear signature in a complex anisotropic medium showing hysterical behaviour was developed. This technique is focused on the nonlinear effects of elastic wave propagation induced by impact damage (cracks and delamination), and is based on a combination of nonlinear reciprocal time reversal and a novel technique called *phase symmetry analysis*. Unlike other damage detection approaches, this nonlinear imaging method is used to characterize the third order nonlinearity of the damaged structures by exploiting its invariant properties with the phase angle of the frequency modulated (FM) excitation signals.
A summary of the original aspects of this thesis is shown in Fig. 1.1.

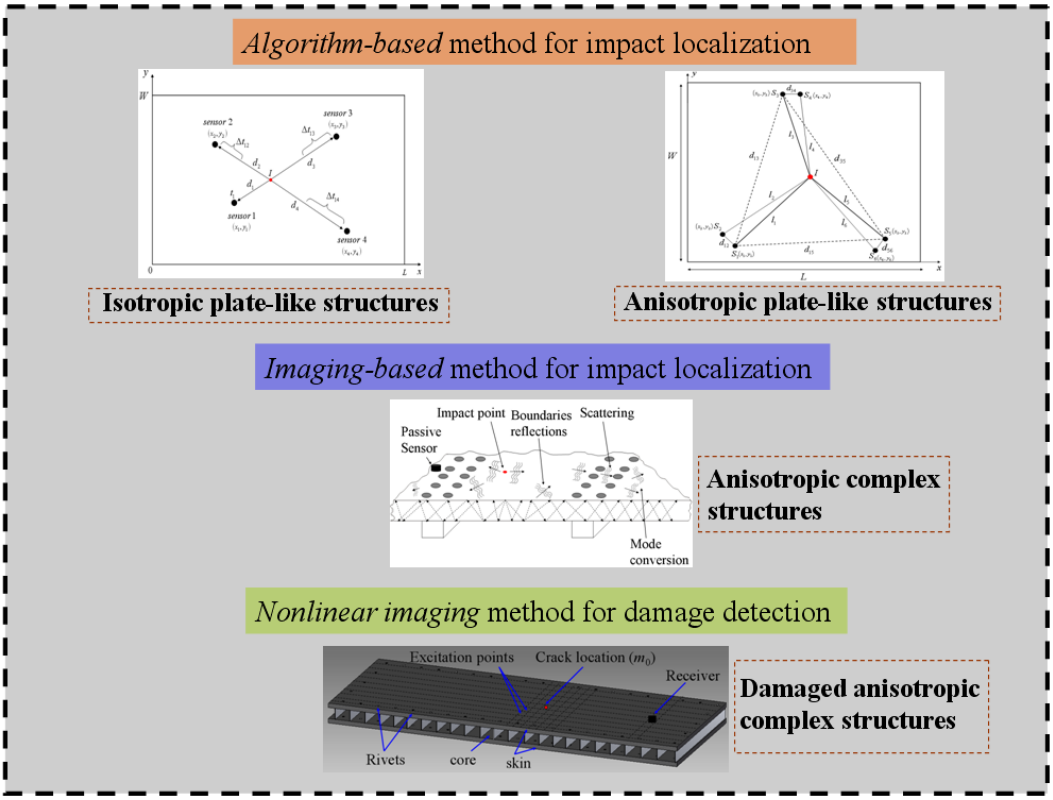

Figure 1.1: Original contributions of this research to impact localization and damage detection

1.3 Outline of the Thesis

The outline of the thesis is the following: the first three chapters (from chapter 2 to 4) will provide a summary of the background, tools and theoretical aspects adopted in this thesis. In chapter 2 a review of various SHM methodologies present in literature for the damage detection and impact localization is presented. In particular, the current developments in assessing the severity of damage mechanisms using linear and nonlinear ultrasonic techniques, as well as the acoustic emission and impact localization algorithms for isotropic and anisotropic structures, are addressed. Moreover, the main characteristics of imaging methods for damage and impact source identification are discussed. Chapter 3 gives an overview of guided wave solutions in isotropic and anisotropic multilayered structures. In particular, the Rayleigh-Lamb relations are mathematically formulated for isotropic media, and then, in order to generalize the analysis of dispersion to anisotropic materials, a semi-analytical spectral finite element model (SFEM) is reported. Chapter 4 is dedicated to an overview of the theoretical basis of time reversal (TR) imaging method by introducing the first experimental set-ups known as "Time Reversal Cavity" (TRC) and "Time Reversal Mirror" (TRM). Hence, in order to understand the principle of refocusing elastic energy in geometrically complex media, the main properties of TR wave physics along with the Green's function theories are presented.
Chapter 5, 6 and 7 will cover the main content of this study, by presenting the original contribution to the SHM systems for impact localization and damage detection. Chapter 5 investigates the development of two algorithms for the localization of impact source in anisotropic and isotropic media. The proposed methodologies, depending on the nature of the medium, are based on the differences of the stress waves measured either by four or six piezoelectric transducers. In both techniques, a joint time-frequency analysis based on the magnitude of the Continuous Wavelet Transform was used to determine the TOA of the stress waves. Then a combination of local Newton's method and unconstrained optimization was employed to determine the coordinates of the impact location and the values of the flexural group velocities reaching each sensor. Chapter 6 presents an imaging method able to detect the impact source in reverberant

complex composite structures using only one passive sensor. This technique is based on the reciprocal time reversal (inverse filtering) method applied to a number of waveforms stored in a database containing the impulse response of the structure. The optimal focalization in spatial and time domain of the acoustic emission source (impact point) was achieved through a “virtual” imaging procedure using the “benefits“ of a diffuse wave field. Chapter 7 reports an imaging method of the nonlinear signature due to cracks and delamination in a reverberant complex anisotropic medium showing hysteretic behaviour. Phase symmetry analysis, together with frequency modulated (FM) excitation signals, were used to characterize the third order nonlinearity of the structure. Then, a “virtual” reciprocal time reversal imaging process, using only one receiver sensor, was used to ”illuminate” the damaged area by taking advantage of multiple linear scattering.

Chapter 2

Structural Health Monitoring Techniques for Damage Detection and Impact Identification

Due to their versatility and sensibility, Structural Health Monitoring systems can be used for the real-time identification of the impact source and the assessment of the structural damages (evolution of defect, residual life, etc). Indeed, an external stimulus as an impact, a change in pressure or strain can induce acoustic emission (AE) that can be recorded by a network of piezoelectric transducers. In this manner, an early warning of the damage occurrence, resulting into safer structures and costs savings, can be provided. These systems are particularly suitable for probing components with different geometries, ensuring high reliability and a global inspection of large structures. In particular, as NDE techniques, SHM methods can be classified in:

- *active SHM* techniques
- *passive SHM* techniques

The first technique is used to detect and evaluate damages and can be distinguished in *linear* and *nonlinear* methods. Both approaches are based on generating perturbations in the structure by using actuators, and then, using sensors to monitor the wave response. Usually, a piezoelectric transducer (or an array of

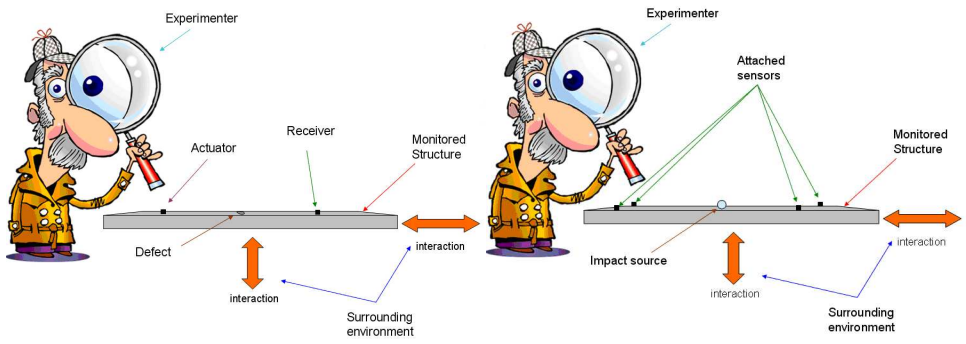

Figure 2.1: Active (a) and passive (b) SHM techniques

sensors) is employed as an emitter of elastic waves and a second sensor is used as a detector. From the collected sensor data, it is possible to deduce the presence of the defects within the material, by using a suitable time-frequency analysis method. Passive SHM techniques do not make use of integrated actuators and are mainly adopted to locate impacts or acoustic emission (AE) events. Indeed, the signals emitted by internal or external sources can be measured by ultrasonic transducers directly on the specimen surface or embedded into the structure (Balageas *et al.* [2006])(Fig. 2.1). Moreover, beside the above mentioned techniques, a novel class of *imaging methods* for SHM applications was developed to provide an image of the structural damages and the impact location in complex structures through sparse sensor arrays measurements.

2.1 Linear Damage Identification Methods

Traditional acoustic/ultrasonic SHM damage detection techniques in atomic elastic materials as viscoelastic media and monocrystalline solids (aluminium, steel, Plexiglas) are based on *Classical Linear Elasticity* (CLE) theory (Auld [1973]). Such methods are aimed either to study the acoustical vibrations of the structure and the changes of wave group speed and signal amplitude, or to measure impedance contrasts from open interfaces such as voids and free surfaces (Chang [1999]). Indeed, the presence of defects changes the acoustic parameters of phase and amplitude of the modes propagating within the medium. Linear damage

identification techniques can be distinguished in two different branches:

- *Acoustics vibration-based* methods
- *Ultrasonic guided wave* methods

Acoustic vibration-based techniques, also known as *global approaches*, are based on the concept that changes of physical properties of the entire structure, introduced by damages, alter its measured dynamic response such as resonant frequencies, mode shapes and modal damping (Doebling *et al.* [1996]). However, there are several disadvantages limiting the application of these methods. First, the sensitivity of most vibration-based methods to damage detection is very low (with frequency excitation generally less than 50 kHz). Then, external factors such as boundary and loading conditions may impair the reliability of damage detection.

Ultrasonic guided wave approaches can be regarded as *local damage detection* methods and make use of high frequency excitation, typically within the range of 50/100 kHz to 5 MHz. In this techniques the acoustic emissions, exited by actuators, propagate within the structure and are collected by a network of surface bonded or embedded sensors. Structural damages can be estimated through the analysis of local wave response such as reflection, refraction and scattering. A number of studies has investigated the use of guided waves (GW) to assess the severity of the defects either in isotropic (Giurgiutiu [2002], Hurlebaus *et al.* [2001], Quek *et al.* [2001]), and anisotropic materials (Cawley [1994], Diamanti *et al.* [2002], Paget *et al.* [2002a]).

2.1.1 Acoustics Vibration-based Methods

Acoustic vibration-based methods are among the earliest damage detection methods used, principally because they are simple to implement on structures with any size. These techniques identify damages by monitoring changes in the dynamic properties or the material response. Normally, they require an excitation source (at low frequencies) such as hammers, vibro-dynamic devices or piezoelectric transducers. The *global* methods can be classified on the types of measured

data used, or the technique employed to identify the damage from the measured data.

2.1.1.1 Frequency Changes Methods

These methods are based on the assumption that measured frequency shifts due to the presence of defects allow identifying their location and evaluating their severity (Lee & Shin [2001]). The frequency methods can be divided in two classes of problems, the *forward* and the *inverse problem*. The former consists of calculating the frequency shifts from a known type of damage. Typically, the damage is modelled mathematically, and then, the measured frequencies are compared to those predicted by the model to assess the damage. The latter technique consists of finding damage parameters such as crack length and delamination from the frequency shifts. Then, mathematical and numerical models are used for the assessment of the severity of the damage. The limitations of the frequency changes methods have been described by Doebling et al. (Doebling *et al.* [1998]) and are due to:

- low sensitivity of frequency shift to damage that requires either very precise measurements or large level of damage
- great effort required in the extraction of the modal parameters especially when the structure is complex or at high frequencies
- lack of spatial information on the damage provided by frequency shifts
- insufficient number of frequencies with significant changes to determine the location of the damage

2.1.1.2 Mode Shape Changes

In this method, the assessment of the defect is obtained comparing mode shape and slopes of the modes of the structure damaged and undamaged. As such, the information of the location of the flaw can be achieved without the use of a finite element (FE) model. Different mode shape criteria are presents in literature. Doebling et al. (Doebling *et al.* [1996]) used the *Modal Assurance Criteria* (MAC)

to select the most affected mode shapes by structural damages. However, as seen in Sec. 2.1.1.1, a critical issue of this methodology is the mode shape extraction that becomes very difficult with the increase of frequency and the complexity of the structure. Moreover, this technique can be used only when all types of damages that may occur into the structure are known. Otherwise, the defects not included might not be detected.

2.1.1.3 Compliance Matrix Methods

This class of damage identification methods uses the dynamically measured compliance matrix (the inverse of the stiffness matrix) to estimate changes in the static behaviour of the structure. Generally, these techniques compare the compliance matrices of the damaged structure with that of the undamaged structure, or the compliance matrix from a previously validated FE model (Gao & Spencer [2002]). However, the modal properties extracted (typically the lowest-frequency modes of the structure) influence the damage resolution of these methods, leading to the identification of only those damages that affect the resonance properties extracted.

2.1.1.4 Matrix Update Methods

These methods modify the structural model matrices such as mass, stiffness and damping of a FE model of the undamaged structure, in order to reproduce as closely as possible the measured static or dynamic response (Doebling *et al.* [1996]). The location and severity of damage can be obtained comparing the update structural matrices to the originals before permutation. These techniques use a common set of equations and can be classified upon the different algorithms of resolution:

- *Objective function to be minimized*: the objective function is a measure of the differences between FE model and experimental modal properties. Usually Newton's algorithm, applied to unconstrained optimization is required to minimize the objective function
- *Constraints placed on the problem*: the constraints depend on the type of

algorithm, but generally, they are used to preserve the characteristics of the updated matrices, such as symmetry, sparsity and positivity

- *Numerical schemes used to implement the minimisation process*: principal numerical schemes for constrained optimization are Lagrange multiplier and Penalty method approach. In the last case, a sequence of sub-functions represents the constraints that are added to the objective function to be minimized

2.1.2 Guided Ultrasonic Wave Methods

Stress waves originated by cracks, fibre/matrix interfacial failure, fibre pullout, matrix crazing, micro-cracking and disbonding, supply information on damage and its location and propagate through the structure at great speed to detectors located on the surface. However, more than one wave mode can propagate at the same time, even when generated from the same source. As the velocity of the modes is different, even transit time is different, and the total wave energy spreads over time with the increase of the distance. Wave packets that propagate as superposition of various modes are often called *Guided Waves* (GW). These modes are governed by the same wave equations as bulk waves, however, in contrast to the latter which are non-dispersive, GW have an infinite number of modes associated with propagation. There are various types of GW available in practise. When an elastic wave encounters a boundary between two media, its energy is divided between the reflected and the refracted wave. These phenomena change the amplitude and direction of a wave, introducing critical angles (David & Cheeke [2002]). Depending on the nature of the material, if the medium is a *semi-infinite medium*, the refracted waves are bound to the surface generating Rayleigh (Rayleigh [1887]), Stonely (Stoneley [1924]), Scholte (Sholte [1942]), and Love waves (Love [1926]) (Fig. 2.2).

Conversely, if the medium is a *finite medium*, the elastic waves are bound within the structure, inducing *Lamb waves*. According to Viktorov (Viktorov [1967]) theory, Lamb waves are guided stress waves that propagate within thin solid plates with free boundaries conditions. Unlike bulk waves, depending on the product of frequency times thickness, an infinite number of modes for both

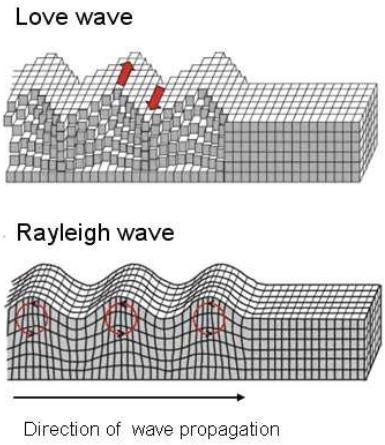

Figure 2.2: Surface waves, from David & Cheeke [2002]

symmetric and *antisymmetric* displacements are available. Symmetric modes (S_n) are related to the extensional modes as displacements occur in the direction of wave propagation, whilst antisymmetric modes (A_n) are known as flexural modes as the displacements pattern is transverse to the plane of the plate (see chapter 3). Fig. 2.3, shows the propagation of symmetrical and antisymmetrical Lamb waves, which are the most widely used GW for SHM applications.

2.1.2.1 Lamb Waves Generation and Reception

Within the SHM paradigm, various advanced transducer technologies are currently available which can be adapted or embedded into the structure to sense Lamb waves. Such sensors are often referred to as "*smart*", i.e. they accommodate integrated capabilities as signal acquisition, processing, analysis and transmission. *Smart* transducers include piezoelectric sensors (Crawley & Anderson [1990], Giurgiutiu & Zagrai [2000]), interdigital transducers (Wilcox *et al.* [1997]), sensitive nanocomposite sensors (Capezzuto *et al.* [2010]), fibre optic sensors (Udd [1994]), carbon nanotube sensors (Kang *et al.* [2006]), comparative vacuum sensors (Barton [2009]) and Micro-Electro-Mechanical Systems (MEMS) (Butrus *et al.* [2000]). In particular, this thesis is focused on the use of piezoelectric (PZT, lead zirconate titanate) crystals or ceramics, which are often chosen as actuators/receivers because of their high force output at relatively low voltages

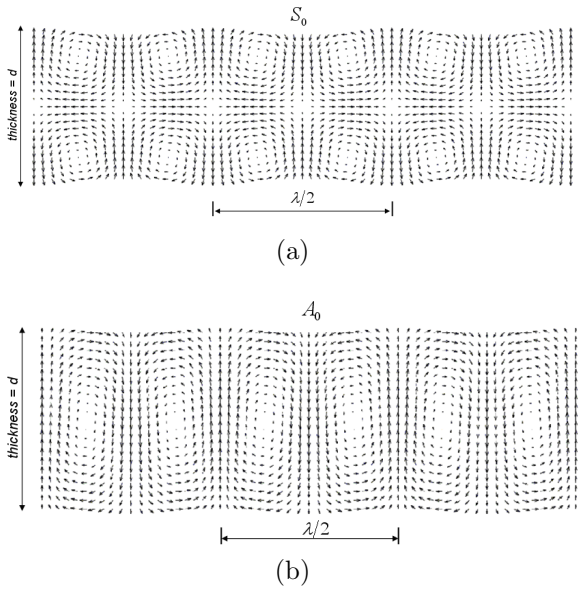

Figure 2.3: Lowest order symmetric (a) and antisymmetric (b) Lamb modes in a plate

and their good response at high/low frequencies. Each transducer is independent of others and is connected through conductive cabling to a centralized data processing and multiplexing unit. Indeed, PZT sensors or patches can be used in numerous applications involving vibration suppression and sensing, sonar, air ultrasonic transducers, etc... Depending on whether the testing scheme for damage detection is *pitch-catch* or *pulse-echo*, one transducer as actuator and the other as receiver, or just one sensor that acts as both transmitter and receiver are required, respectively.

Piezoelectric crystals and certain ceramics belong to a larger class of materials called *ferroelectrics*, wherein the molecular structure is oriented in way the medium exhibits a local charge of separation termed electric dipole (Culshaw [1996]). The electric dipoles are oriented randomly within the material, but when a very strong electric field is applied and the medium is cured above a certain temperature (Curie temperature), the electric dipoles reorient themselves in the direction relative to the electric field (*poling process*). When the structure is cooled, if the dipoles maintain their orientation, the material will exhibit a *piezoelectric effect*. This effect is responsible for the medium's ability to transform the

mechanical energy of the elastic wave into electrical energy, giving rise at two different phenomena, a *direct piezoelectric effect* and a *converse piezoelectric effect*. The former effect consists in the generation of an electrical charge in proportion of an external applied force, and allows PZT materials to function as receivers. The latter phenomenon consists in the medium's ability to convert an electrical potential into a mechanical strain and allows PZT materials to work as actuators. The mechanical/electrical behaviour of piezoelectric media can be described through the thermo-piezoelectric constitutive equations as follows (Ikeda [1996]):

$$\begin{aligned} e_{ij} &= s_{ijlm}^{E,T}\sigma_{lm} + d_{ijn}^{T}E_n + \alpha_{ij}^{E}\triangle T \\ D_k &= d_{klm}^{T}\sigma_{lm} + \epsilon_{kn}^{\sigma,T}E_n + p_k^{\sigma}\triangle T \end{aligned} \tag{2.1}$$

where $s_{ijlm}^{E,T}$ are the elastic compliance coefficients, d_{ijn}^{T} the piezoelectric strain constant, α_{ij}^{E} the coefficient of thermal expansion, $\epsilon_{kn}^{\sigma,T}$ the dielectric permittivity and p_k^{σ} the pyroelectric coefficient. In linear piezoelectricity, where temperature variation is negligible, the equations of linear elasticity are coupled to the charge equation of electrostatics by the means of the piezoelectric constants. In compact matrix notation, we have:

$$\begin{aligned} \mathbf{e} &= \mathbf{s}^{E}\boldsymbol{\sigma} + \mathbf{dE} \\ \mathbf{D} &= \mathbf{d}\boldsymbol{\sigma} + \boldsymbol{\epsilon}_d^{\sigma} \end{aligned} \tag{2.2}$$

with $\boldsymbol{\sigma}$ the stress vector, $\mathbf{e}$ the strain vector, $\mathbf{D}$ the electric displacement vector, $\mathbf{E}$ the electric field vector, $\mathbf{s}$, $\boldsymbol{\epsilon}_d$ and $\mathbf{d}$ the elastic, dielectric and piezoelectric constant matrix, respectively. Superscript E and σ indicate values at E and σ constant, respectively.

Piezoelectric materials can be classified in two coupling modes, the -33 and the -31 modes (Tzou [2003]). In the -31 mode the electric field is applied in the 3 direction and the material is strained in the direction perpendicular to the poling direction; in the -33 mode the electric field is applied in the 3 direction and the material is strained in the poling direction (Roundy *et al.* [2003]) (Fig. 2.4). These two modes of operation are particularly important when defining the electromechanical coupling coefficient d and g. The former is the transmission term,

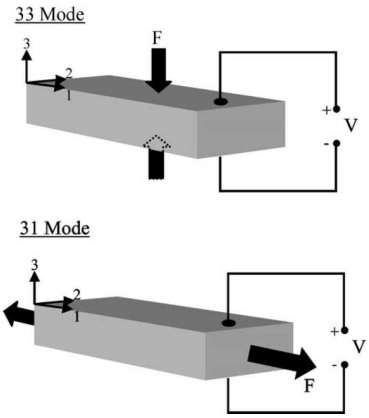

Figure 2.4: Illustration of -33 and -31 mode operation, from Roundy *et al.* [2003]

whilst the latter corresponds to the sensor term. Both coefficients are related each other by the following formula (Tzou [2003]):

$$g_{31} = \frac{d_{31}}{\varepsilon_0 K_3} \qquad g_{33} = \frac{d_{33}}{\varepsilon_0 K_3} \tag{2.3}$$

with ε_0 and K_3 the permittivity of free space and the dielectric constant, respectively. The shape of the piezoelectric sensors is generally chosen based upon the desired propagation or reception direction and the structural damages to investigate. PZT transducers are mainly disc-shaped, rectangular or square. Wilcox (Wilcox [2004]) studied the use of circular and linear arrays using piezoceramic disk for long-range guided waves applications in isotropic materials, providing an indication of the scanning capabilities achievable with actuators arrays. Interestingly, the ratio of the area of the plate inspected over the area of the circular transducer array was about 3000:1.

The vast majority of studies focused upon structural damages are based on active acoustic emission (AE) monitoring systems using PZT transducers sensors attached to plate-like structures (Brown [2000], Giurgiutiu [2002]). A formal definition of acoustic emission is often given as "*the release of energy in the form of transient elastic waves produced by a rapid redistribution of stress in a material*" (Achenbach [1984]). For ultrasonic Lamb modes generation (see chapter 3), the actuator length for optimal signal is obtained by a sinusoidal relationship between

the actuating wavelength λ and the actuator length L as follows (Viktorov [1967]):

$$L = \lambda\left(n + \frac{1}{2}\right) = \frac{c_{ph}}{f}\left(n + \frac{1}{2}\right) \qquad n = 0, 1, 2, \ldots \tag{2.4}$$

where f is the central frequency and c_{ph} is the phase velocity of the generated wave. Diamanti et al. (Diamanti *et al.* [2007]) developed an array system of piezoceramic sensors bonded on the surface of quasi-isotropic carbon fibre reinforced plastic (CFRP) laminates, for the detection of cracks and holes caused from low-velocity impacts. El youbi et al. (El youbi *et al.* [2004]) performed a pitch-catch ultrasonic system of multi-element piezoelectric transducers associated to a signal processing algorithm for analyzing three Lamb modes (A_0, S_0 and S_1). His work was aimed to study the interaction between the modes and the defects and to identify the most sensitive mode related to the damage. Giurgiutiu (Giurgiutiu [2002]) previously investigated this selectivity of piezoelectric transducers. He developed a theoretical model based on the 2-D Fourier Transform analysis of the Lamb displacement and strain wave solutions, harmonically exited by surface mounted piezoelectric active wafer sensors (PWAS). This tuning capability of piezoelectric transducers was exploited by several authors (Diamanti *et al.* [2002], Lin & Yuan [2001]) who employed the fundamental flexural Lamb mode A_0 for its low attenuation and high sensitivity to detect small damages in beams and plates. Moulin et al. (Moulin *et al.* [1997]) and Mall and Hsu (Mall & Hsu [2000]) studied the mechanical and electrical behaviour of smart embedded piezoceramic transducers (known as *adaptive structures*) undergone to cycling loading. Similarly to Mall's work, Paget et al. (Paget *et al.* [2002b]) evaluated the performance of such embedded sensors in carbon/epoxy composite materials. The experimental results revealed that the response of the these smart sensors in both static and fatigue loading conditions remained approximately unchanged.

An alternative to these conventional transducers was the use of polyvinyldilene fluoride (PVDF) film sensors (Gaul & Hurlebaus [1999], Monkhouse *et al.* [2000]). PVDF polymer is known to show a relatively strong piezoelectric effect despite it is not as sensitive as PZT sensors. These smart materials bonded on the surface of the structures own the characteristic of better interrogate large areas with a low cost availability, high flexibility, low weight, easily handle and broad-

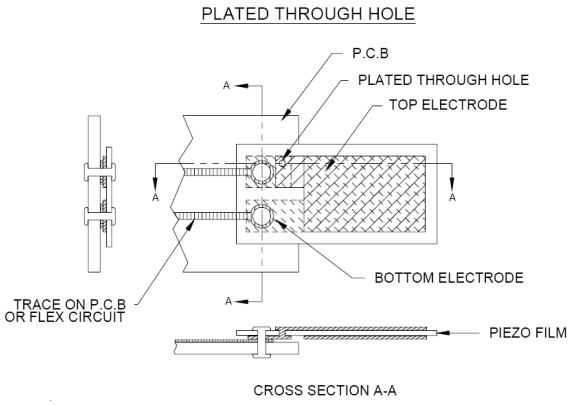

Figure 2.5: Piezoelectric-film for AE applications, from Measurement Specialities (http://www.meas-spec.com/)

band acoustic performance. However, this technology still suffers from having a signal-to-noise ratio that is not high as those measured by PZT, and a low Curie temperature that limit its integration as an embedded sensor (Fig. 2.5).

Recently, Active and Macro Fibre Composite (AFC and MFC, respectively) patches were developed as a promising alternative to traditional brittle monolithic piezoceramic transducers. Indeed, as ceramic materials are very dense and stiff, their use is limited in flexible or lightweight structures. Conversely, the flexible nature of polymer matrix allows fibre composite media to be more easily conformed to curved surfaces for aerospace and civil structural applications. Both AFC and MFC patches consist in an active piezoceramic fibrous phase embedded in a polymer. In particular, they are made from piezoceramic fibres or rods produced through a patented moulding process (Gentilman *et al.* [2003]), that are sandwiched between two sets of interdigitated electrodes (IDE). The IDE are manufactured on thin polymer films and are oriented perpendicular to the fibres or rods (Wilkie *et al.* [2000]). AFC actuator was developed at MIT's Active Materials and Structures Lab and is composed by unidirectional aligned piezoceramic fibres surrounded by a polymer matrix with an electrode layer placed on the top and bottom of the fibres (Bent *et al.* [1995]) (Fig. 2.6). MFC actuator was developed at the NASA Langley Research Centre and consists of active piezoceramic rods, IDE and an adhesive polymer matrix (Fig. 2.7). AFC patches are formed from an injection moulding process, whilst MFC rods are machined from

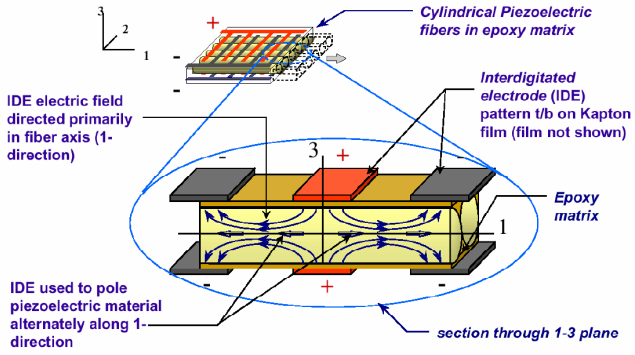

Figure 2.6: Cross section of AFC actuator, from Wilkie *et al.* [2000]

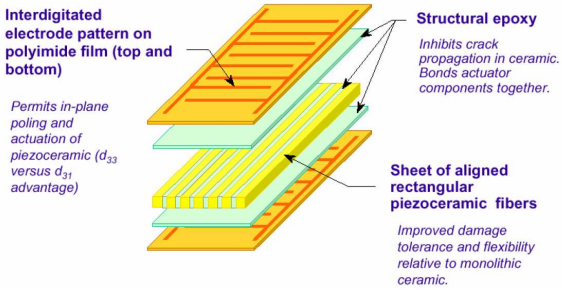

Figure 2.7: Schematic of MFC actuator, from Smart Materials Corp. (see http://www.smart-material.com/)

piezoceramic wafers and a computer dicing saw, in way to significantly lower the manufacturing costs (Lanza Di Scalea *et al.* [2007]) (Fig. 2.8).

Moreover, compared with piezoelectric bulk and wafer transducers, the resonance frequencies and transfer function of AFC and MFC transducers can be easily changed with high sensitivity, by simply cutting the patches. However, their behaviour under mechanical and thermo-mechanical loads is still largely unknown (Brunner *et al.* [2009]).

Professor Fu-Kuo Chang, at Stanford University, conceived the Stanford Multi-Actuator-Receiver Transduction (SMART) Layer. Such material is composed by a network of distributed thin piezoelectric patches embedded into a thin dielectric film, which can be surface mounted onto metallic structures or embedded in composite structures before curing. The film is available in various configurations, either as thin strips with the sensors in one row or as a flat 2-D layer of

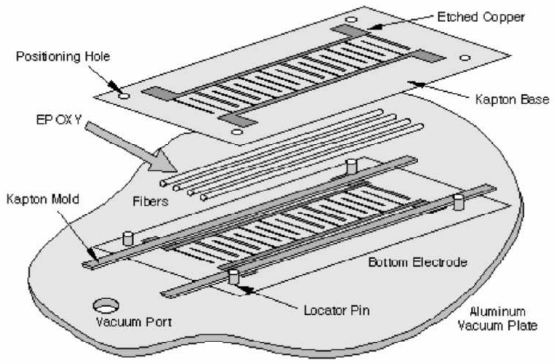

Figure 2.8: Schematic of the manufacturing process of AFC actuators, from Wilkie *et al.* [2000]

typical dimensions up to 0.6 × 9 mm. In addition, the film can be manufactured as a 3-D customized layer to fit specific structures (Lin & Chang [2002]). The standard thicknesses are 60 μm and 125 μm for the film and 250 mm and 750 mm for the piezoelectric patches. Even though SMART layer is mainly used for composite structures, it can be also used for crack monitoring in metallic structures (Lin *et al.* [2001], Ihn & Chang [2004]). A summary of the various piezoelectric materials discussed above can be found in Tab. 2.1.

2.1.2.2 Time-frequency Analysis Methods

One of the main objectives of SHM is to extract certain physical parameters from measured data in structures and then to use them to quantify the health status. Due to the dispersive nature of the flexural modes or to the uncertainty of the noise level of the signal measured, a suitable choice of the time-frequency analysis is necessary. In recent years, some advanced techniques based on the time-frequency analysis were applied to study waves in solids, such as *Short-Time Fourier Transform* (STFT) (Hodges *et al.* [1985]) and *Wigner-Ville Distribution* (WVD) (Latif *et al.* [1999]). However, because of the constant window structure employed in STFT, this technique is not capable of providing sufficient resolution over a wide spectral range. Furthermore, since WVD is defined as the Fourier transform of the central covariance function of a given signal and has quadratic structure, it inevitably generates interference terms that incur spurious informa-

Piezoelectric Smart Material	Advantages/Disadvantages
Monolithic PZT	Most common type of device Not flexible Susceptible to fatigue crack growth during cycle loading
PVDF	High Flexibility Resistance to fatigue crack Low Curie temperature
AFC and MFC	High Flexibility Low-capacitance devices Energy harvesting capability
SMART Layer	High Flexibility High electrical performances Resistance to fatigue crack

Table 2.1: Summary of several piezoelectric materials investigated

tion in the signal measured. White (White [1969]) was one of first to look into arrival time measurements in dispersive media. Ziola and Gorman (Ziola & Gorman [1991]) employed a cross-correlation technique for determining the time of propagation, whilst Kosel et al. (Kosel *et al.* [2003]) used a combination of cross-correlation function with an appropriate bandpass-filter. In both approaches, the maximum of the cross-correlation coefficient of two signals indicates the delay time between them:

$$R_{xy}(\tau) = \lim_{T\to\infty} \frac{1}{T} \int_{-T}^{+T} x(t)y(t+\tau)dt \tag{2.5}$$

where $y(t)$ is the output waveform from each transducer and $x(t)$ an input pulse consisting of a cosine wave modulated by a Gaussian pulse. However, these methods present some limitations especially when the sensors are placed close to the edges. In fact, multiple reflections from the boundaries generate ambiguous peaks in cross-correlation coefficients, which may cause a wrong interpretation of the signal content. Seydel and Chang (Seydel & Chang [2001]) proposed an approach based on a double peak method wherein the arrival time was chosen by selecting the minimum before the maximum for each signal (Fig. 2.9).

Nevertheless, the dependence of the wave velocity on frequency and the am-

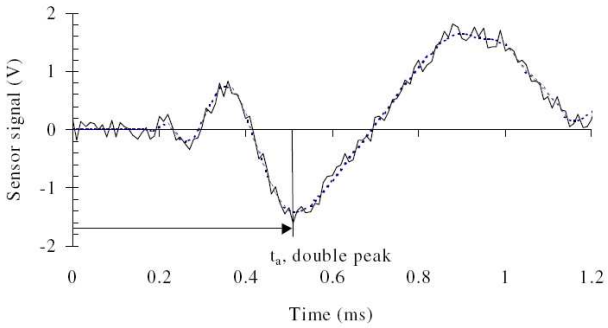

Figure 2.9: Illustration of the arrival time using double peak method, from (Seydel & Chang [2001])

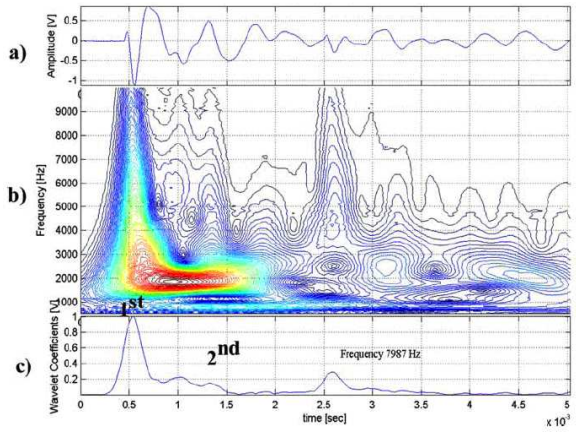

Figure 2.10: Time histories of the signal recorded (a), the contour-plot of the scalogram of the CWT (b) and line profile of the scalogram illustrating the procedure to extract the TOA at $f = 7000$ Hz (c), from (Meo *et al.* [2005])

biguity of the noise level made this method inappropriate for the purpose of a correct determination of the source. Therefore, the use of the *Continuous Wavelet Transform* (CWT), that provides high resolution for a wide range of frequencies, was found to guarantee more accuracy in the time-frequency analysis of acoustic waves (Jeong & Jang [2000], Meo *et al.* [2005]) (Fig. 2.10). Gaul and Hurlebaus (Gaul & Hurlebaus [1999]) applied the Gabor wavelet to an impact localization algorithm for aluminium plates and Meo (Meo *et al.* [2005]) used the Morlet wavelet to detect a source location of an acoustic emission on CFRP and sandwich composite panels.

2.1.2.3 Guided Wave-Based Damage Detection Techniques

Due to their capability of carrying energy over long distances, GW ultrasonic systems are widely used in many SHM applications. The excitation of the structure under interrogation occurs through actuators and then, receiver sensors are used to monitor the acoustic emission response. Indeed, a typical GW sensing system necessitates of a computing processor, signal conditioners, analog-to-digital (A/D) converters and a waveform generator. GW damage detection systems can be distinguished in the *direct path* and the *energy-based* approach. The former method consists in evaluating the extent of the defect from the amplitude of the scattered signals observed in the region covered by multiple actuator-receivers paths, obtained from a new and a reference set of data. Indeed, since AE signals generated from initiation of the defect carry the information of the damage, the location of the defect can be estimated by the differences between the undamaged (baseline) and the damaged structure or using statistically threshold methods (Sohn *et al.* [2004]). *Energy-based* method makes use of arrival time (TOA) measurements of reflected/refracted waves from the defect. TOA necessitate extensively signal-processing as wavelet transform decomposition, and the damage detection can be accomplished through an elliptical function (Ihn & Chang [2008b]), whose the actuator and the receiver are the foci (Fig. 2.11). Then, the damage position can be obtained using specific optimization algorithms.

Unlike acoustics vibration based methods, local techniques posses the capability to customize the excitation in order to achieve high sensitivity to specific defect types. Among the guided ultrasonic wave techniques, the *energy-based* method is usually preferred to the *direct path* approach. Indeed, variations of the environmental conditions and gradual ageing of the structural components may significantly alter the baseline features, thus causing poor damage localization (Kehlenback & Hanselka [2003]).

Moreover, another approach used for the assessment of structural damages is the *neural network* (NN) method. Such technique is an intelligent data fusion system that works on the idea of training intensively a computer network with known inputs and outputs until the network converges. The reasons lie in the strong interpolation capacity of NN, allowing the identification of damages in

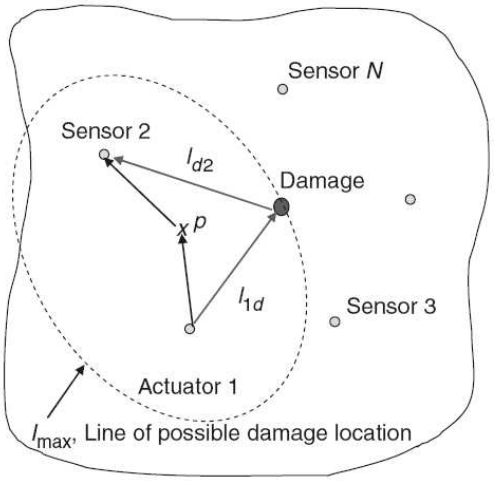

Figure 2.11: Elliptical locus of possible damage location, from (Ihn & Chang [2008b])

terms of location, extension and type. Studer and Peters (Studer & Peters [2003]) applied this technique to identify the size, the location and the angle of a crack in a plate using strain gradients values correlated to test crack parameters. The NN showed to significantly improve the detection of the crack properties when compared to the other approaches previously seen. However, neural network, as any interpolation algorithm, is able to identify the damage with remarkable accuracy only within a training range (Wang & Chen [2010]). Such training requires a large data sets from both the undamaged and damaged structures, which makes NN method rarely available for real aerospace or civil applications.

2.2 Nonlinear Damage Identification Methods

Nonlinear micro-damages may be missed by the linear methods if low frequencies are used, or may appear as voids when using high frequencies (Ulrich *et al.* [2008]). Consequently, nonlinear parameters can be much more sensitive to defects than linear ones and novel nonlinear damage detection methods can be developed as a potential tool for the analysis of the level of nonlinearity in damaged materials. Generally, the mechanism for the generation of the nonlinear response in elastic media is the "clapping" of two surfaces in intimate contact as micro-structural

defects (e.g. cracks and delamination) or weakened bonds. The existence and characteristics of nonlinear scattering can be evaluated through the observation of higher harmonics or sidebands effects of the fundamental frequencies using either a mono or bi harmonic wave excitation (Bas *et al.* [2006]).

2.2.1 Nonlinear Classical and Nonlinear Mesoscopic Elasticity

The theoretical model of nonlinear interaction of an acoustic/ultrasonic wave with the material defect relies on a first-order perturbation power series of the strain associated to the general partial differential equation (PDE) describing elastic wave motion [Eq. 3.8]. Microcraked or undamaged materials that have atomic elasticity (aluminium, steel, Plexiglas) arising from atomic-level forces between atoms and molecules show a *Classical Nonlinear Elasticity* (CNE) (Ostrovsky & Johnson [2001]). These equations are valid for moderate amplitude displacements, when the nonlinear terms are small compared with the linear ones. Assuming longitudinal wave propagation along the x-direction, the wave equation in linear elasticity can be expressed as a power series of the strain in $e_x = \partial u(x,t)/\partial x$ as follows (Guyer & Johnson [1999]):

$$\begin{gathered} \rho \frac{\partial^2 u(x,t)}{\partial t^2} = \frac{\partial \sigma}{\partial x} = M_0 \left\{ \frac{\partial}{\partial x} \left[1 + K(x,t) \right] e_x \right\} \\ K(x,t) = \beta e_x + \delta e_x^2 \end{gathered} \tag{2.6}$$

where $M_0 = (\lambda + 2\mu)$ is the longitudinal elastic modulus, β and δ are higher order nonlinear elastic coefficients, normally of the order of 1-10 in value. Eq. (2.6) implies characteristics scaling relations. In particular, the amplitude of the second harmonic scales as e_x^2 and the amplitude of the third harmonic scales as e_x^3. In case of dispersive guided Lamb modes, Deng (Deng [1999]) showed that second-harmonic generation grows linearly with the propagation distance and arises when the phase velocity of a primary Lamb mode equals that of the double frequency Lamb wave. In other words, the second harmonic field can be seen as a superposition of the fields of a series of double frequency Lamb modes (*cumulative effect*). Moreover, the author demonstrated analytically and experimentally that

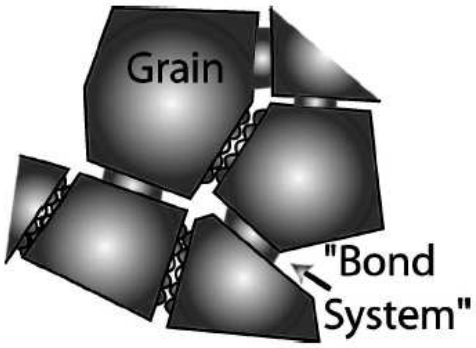

Figure 2.12: Mesoscopic model, from (Johnson [1999])

the generated second harmonic field of a Lamb mode is symmetrical, regardless of the Lamb waves are symmetrical or antisymmetrical (Deng [2003]). However, the material response in the presence of micro-structural features as cracks in the medium lattice or delamination may become highly nonlinear and exhibit quasi-static and dynamics nonlinear effects as hysteresis and relaxation (slow dynamics) in the stress-strain relationship. Hence, such non-classical behaviour of medium cannot be described by simply nonlinear classical theory.

In the last decades, similar nonlinear non-classical characteristics were discovered in granular Earth's materials and other types of solids. Indeed, starting from the 1950s, hysteresis and relaxation effects were also observed in volumetrically damaged materials as rocks, sandstones, ceramics, granular media, and concrete, even at low strain amplitudes (order 10^{-6} and lower) (Guyer & Johnson [1999]). These nonlinear phenomena are principally due to the *biphasic* structure of such media, known as *Nonlinear Mesoscopic Elastic* (NME), that exhibit a large nonlinear response generated by "*hard*" viscoelastic grains, embedded within a "*soft*" inclusions at mesoscopic level (of the order of one to hundreds μm) termed bond system (microcracks, grain contacts and dislocations) (Fig. 2.12).

Fig. 2.13 shows an example of quasi-static experiment carried out on a Berea sandstone specimen (tailored as a bar) measured with the stress input signal illustrated in the inset (Fig. 2.13b). From the above figure, it can be seen that the stress gradually increases up to a maximum value reached at point B, and then decreases towards zero generating a *hysteresis loop*. Indeed, the strain only partially

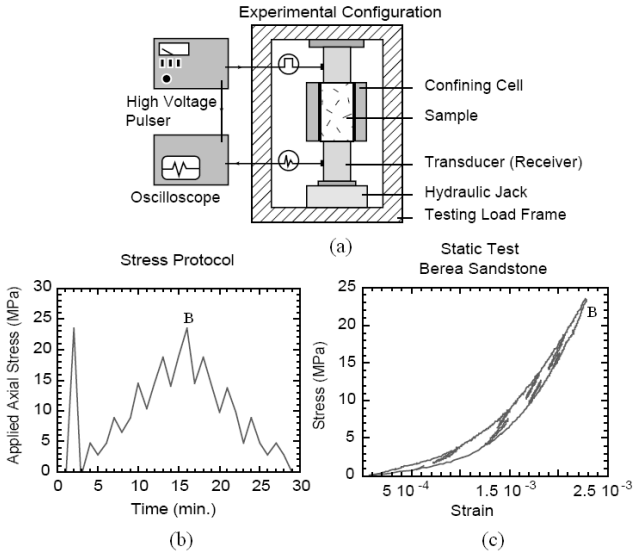

Figure 2.13: Quasi-static experiment for a Berea sandstone. Example of experimental apparatus (a), loading cycle protocol (b) and stress-strain plot (c), from (Ostrovsky & Johnson [2001])

reverses and holds memory of the maximum value of the loading stress, which is the basis of hysteresis. Moreover, the loading protocol includes intermediate sets wherein the stress locally decreases and then increases again up to the same point (Fig. 2.13b). Such sets create small sub-hysteresis loop branches out of the main big loop (Fig. 2.13c). However, the main hysteretic loop is maintained, as the strain keeps memory of the previous maximum value achieved. This phenomenon is a typical signature of material's nonlinear behaviour known as *discrete memory*. Therefore, based on these considerations, a new theory was developed by Guyer et al. (Guyer *et al.* [1994]) based on the *Preisach-Mayergoyz* (P-M) model, which describes classical nonlinearity, hysteresis and discrete memory effects:

$$\begin{aligned} \rho\frac{\partial^2 u(x,t)}{\partial t^2} = \frac{\partial \sigma}{\partial x} = M_0 \left\{ \frac{\partial}{\partial x}\left[1 + K(x,t)\right] e_x \right\} \\ K(x,t) = \left\{ \underbrace{\beta e_x + \delta e_x^2}_{CNE} + \underbrace{\alpha\left[\triangle e_x + e_x sign(\dot{e_x})\right]}_{NME} \right\} \end{aligned} \tag{2.7}$$

where $\triangle e_x$ is the local strain amplitude over a previous wave period, $\dot{e_x} =$

$\partial e_x/\partial x$ is the strain rate, $sign(\dot{e_x}) = 1$ if $\dot{e_x} > 0$, $sign(\dot{e_x}) = -1$ if $\dot{e_x} < 0$ and α is a measure of the material hysteresis. However, a specific form of α is still under investigation from the material physics. Eq. 2.7 can be used to identify the nonlinear response of either local macro-damages ($10^{-2} - 10^{-1}$ m) in aluminium, glass and composites or micro-defects ($10^{-7} - 10^{-6}$ m) in rocks and concrete. From a physical point of view, this means that the induction of distributions of microcracks creates interfaces between portions of the specimen that are filled up either by residual materials or impurities, acting as "binding" medium between "grains".

2.2.2 Nonlinear Elastic Wave Spectroscopy Techniques

Nonlinear elastic effects of damaged materials can be assessed with *nonlinear elastic wave spectroscopy* (NEWS) techniques, which explicitly interrogate the material nonlinear elastic behaviour and its effect on wave propagation caused by the presence of defects (Johnson [1999], Van Den Abeele *et al.* [2001]). A number of NEWS experiments were performed on a wide variety of materials subjected to micro-damages in different environmental conditions.

2.2.2.1 Nonlinear Resonant Ultrasound Spectroscopy

Nonlinear resonant ultrasound spectroscopy (NRUS) technique is aimed to monitoring the dependence of the resonance frequency on the strain amplitude for one or more vibration eigenmodes, while exciting the sample at relatively low amplitudes. Typically, the measurements are carried out through a sweep frequency response analysis over a frequency interval that contains the fundamental eigenmode. The frequency sweeps are repeated at successively increasing drive voltages: for undamaged atomic elastic material no frequency shift is present, whilst in NME media a frequency relative shift is clearly more visible. Fig. 2.14a shows NRUS results for a resonant bar from an atomic elastic material (polyvinylchloride, PVC) in undamaged conditions (Ostrovsky & Johnson [2001]). Fig. 2.14b illustrates an NRUS experiments for intact and damaged concrete samples. Although the undamaged sample exhibits a small amount of peak shift (which is in accordance with CNE theory), the damaged specimen reveals an evident

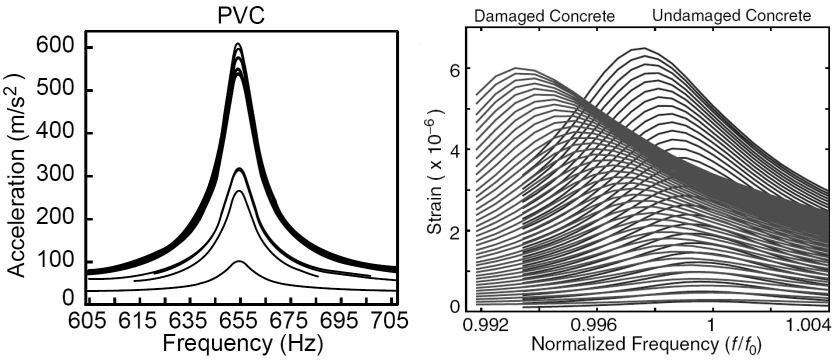

(a) (b)

Figure 2.14: Resonance acceleration response of PVC for several drive amplitudes (a), from (Ostrovsky & Johnson [2001]). Results from two concrete samples, one intact measured in the undamaged state and the other damaged (b), from (Johnson [2006])

downward shift of the resonance frequency with the increase of the excitation amplitude, which is a typical feature of the classical nonlinear elastic behaviour. From the test showed in Fig. 2.14b, the hysteretic nonlinear parameter α was extracted by measuring the changes of frequency with the strain amplitude:

$$\frac{f_0 - f_i}{f_0} = \alpha \triangle e_x \tag{2.8}$$

where f_0 is the natural frequency of intact material or the lowest resonance mode measured, f_i is the natural mode measured for each drive amplitude, $\triangle e_x$ is the average strain amplitude and α is the nonlinear parameter, which ranges nearly between 10 and 10^4.

2.2.2.2 Slow Dynamic Diagnostics

The phenomenon of *slow dynamic* (SDD) or *relaxation* is another characteristic of nonlinear elastic materials such as rock and concrete and solids with localized nonlinear sources (crack, delamination). A typical relaxation experiment is realized with the same apparatus of a NRUS one and consists of monitoring the resonance frequency before and after large excitation. In particular, the structure is first driven at large strain amplitude ($\approx 10^{-4} - 10^{-5}$) for several minutes to

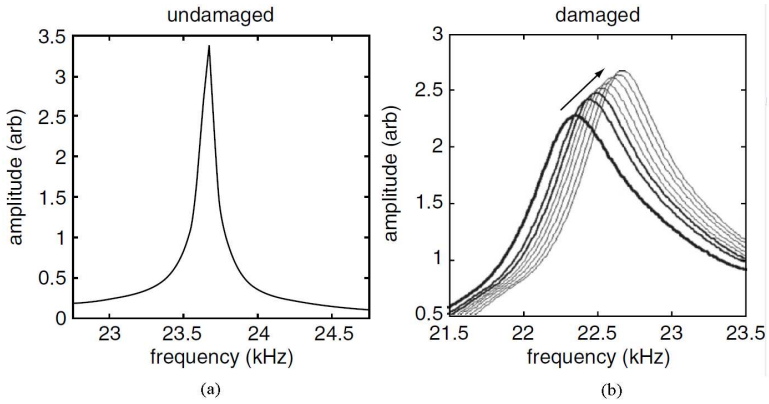

Figure 2.15: Modal resonance response in undamaged (a) and damaged sample. In the latter specimen, the SDD recovery process is clearly visible, from (Johnson [2006])

generate a softening of the medium (lowered average material modulus) (TenCate *et al.* [2000]). Then, a logarithmic-in-time recovery of the structural resonance peak is monitored at low strain amplitude ($\approx 10^{-7}$) until it returns to the original resonance frequency (Fig. 2.15).

The recovery time is a parameter typical of the material and a full recovery ranges between tens of minutes to hours.

2.2.2.3 Nonlinear Elastic Wave Modulation

One of the simplest ways to assess nonlinear elastic effects in damaged materials is called *nonlinear elastic wave modulation* (NEWM), which consists of a nonlinear interaction between two harmonic plane waves having two single frequencies, f_1 and f_2, with $f_1 \ll f_2$ and two different amplitudes A_1 and A_2, with $A_1 \gg A_2$. The material acts as a nonlinear mixer, so that when the harmonic waveforms interact together in the same localized region, not only their superposition, but also *sum and difference frequencies* (Van Den Abeele *et al.* [2000]) in addition to *higher harmonics* (TenCate *et al.* [2000]) and *subharmonics* (Moussatov & Gusev [2003]) of the fundamental frequency f_1 and f_2, can be generated. These new frequency components indicate that a crack or delamination is present within the material. Such phenomena can be predicted by approximated solutions of the Elastodynamics wave equation via perturbative methods, for either nonlinear classical

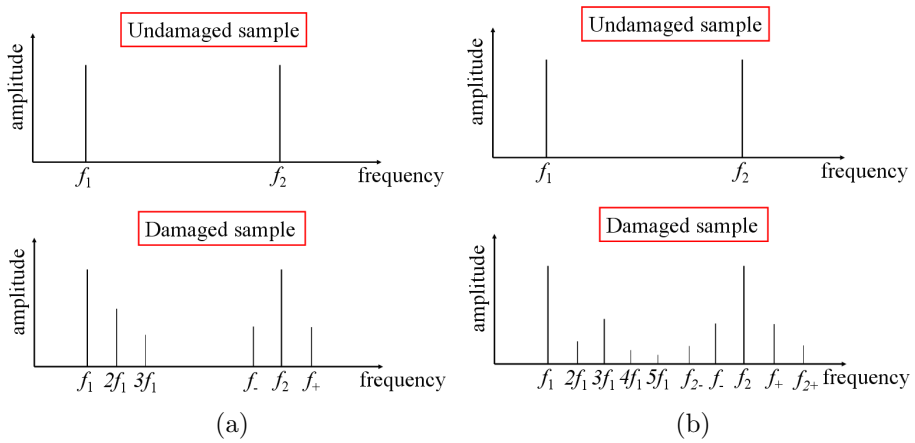

Figure 2.16: Spectra responses for CNE (a) and NME (b) materials. For both figures, data are shown for undamaged (top) and damaged (bottom) specimens

[Eq. (2.6)] or non-classical [Eq. (2.7)] media. However, although both atomic elastic and NME materials exhibit nonlinear wave mixing and higher harmonics generation, only the latter manifest a stronger intensity and phenomenology.

Indeed, as it can be seen from Fig. 2.16, experimental and numerical evidence showed that (Johnson [1999], Guyer & Johnson [1999], Van Den Abeele *et al.* [2000]):

- the 3^{rd} harmonic amplitude of a purely NME material is quadratic with the fundamental amplitude, while a cubic dependence is predicted by CNE theory
- in case of bi-tone (f_1 and f_2) nonlinear wave mixing experiments, NME materials have second order sidebands at frequencies $f_{2\pm} = f_2 \pm 2f_1$ with amplitude proportional to $\alpha A_1 A_2$
- for first order sidebands at frequencies $f_\pm = f_2 \pm f_1$ in CNE media, the amplitudes are proportional to $\beta A_1 A_2$

Meo and Zumpano (Meo & Zumpano [2005]), showed experimentally that a damage introduced on a complex composite structure as a sandwich plate caused a nonlinear non-classical behaviour (hysteresis and discrete memory). Thus, for such materials third harmonic signature can be chosen to identify the damage, as

it is the lowest harmonic with the larger energy content predicted by the nonlinear material hysteretic models.

Another important tool within NEWS methods is the *vibro-modulation* technique, which is based on the interaction of two excitation signals, an ultrasonic probing signal with fundamental frequency f_0 and an amplitude-modulated low frequency vibration (pumping signal) with central frequency f_1 and low-frequency modulation f_2 (Zaitsev *et al.* [2002], Aymerich & Staszewski [2010], Zumpano & Meo [2008]). When the material is undamaged, it behaves as a linear carrier for the frequency of the probe f_0 and for the three frequency components ($f_1 - f_2$, f_1 and $f_2 + f_1$). When the structure is damaged, the modulation is transferred from the pumping signal to the probe excitation and additional sidebands ($f_{0\pm} = f_0 \pm n f_2$, with $n = 1, 2, 3, \dots$) can be observed around the probing fundamental frequency f_0. Hence, the presence and the level of modulation can be used for the assessment of the defect.

2.3 Impact Localization Methods

The growing use of composite materials in aerospace structures has attracted much interest to the development of real-time, accurate, and cost effective ultrasonic SHM systems for the localization of impact points due to their poor impact resistance properties. Mathematically, the estimation of the impact or the acoustic emission source present on the structure is an inverse problem based on the *wave propagation approach*, i.e. the detection of the time at which the stressed waves reach a number of sensors. Such technique can be employed for both isotropic and anisotropic materials and is usually divided into two steps. First, the time of arrival (TOA) of the stress waves is measured by a network of transducers and the signals are evaluated using a suitable time-frequency analysis. Then, a resolution algorithm is used to convert this information into the impact location. Nevertheless, when the test specimen is a finite medium (plate-like), depending of the product frequency times thickness, extensional/symmetric (S_n) or flexural/antisymmetric (A_n) Lamb modes can be generated (see chapter 3). These Lamb waves differ in their phase and group velocities as well as in the strain and stress fields.

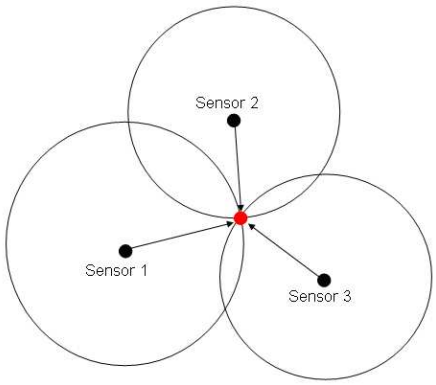

Figure 2.17: Illustration of Tobias algorithm

2.3.1 Impact Source Localization Methods in Isotropic Media

Usually, most of methods for impact location in isotropic and quasi-isotropic materials use the triangulation technique (also known as Tobias algorithm (Tobias [1976]), wherein the impact point is identified as the intersection of three circles, whose centres are the sensors location (Fig. 2.17).

Real-time impact localization algorithms must exhibit the best tradeoffs in terms of *efficiency* and *accuracy* and must require very little computational time (CPU cost) for different use in a SHM system. Kundu and Das (Kundu *et al.* [2009]) developed an optimization algorithm for the determination of impact point on aluminium and stiffened structures, based on minimizing an error function that used the difference of time of arrival of AE signals. The experiment were carried out by using dropping balls in three different locations of the plate and recording the acoustic emission signals to identify the coordinates of the source (Fig. 2.18).

DeMarchi et al. (Marchi *et al.* [2011]) proposed an analytical solution for the impact source location using a hyperbolic positioning method based on the cross-correlation of the signals acquired by different sensors. Gaul et al. (Gaul *et al.* [2001]) applied a Gauss-Newton method to non-linear least square optimization to analyse "synthetic" AE signals. Conversely, an alternative approach to model-based methods for the identification of the impact location was the artificial neural network (NN) approach (see Sec. 2.1.2.3). Despite this method is suitable

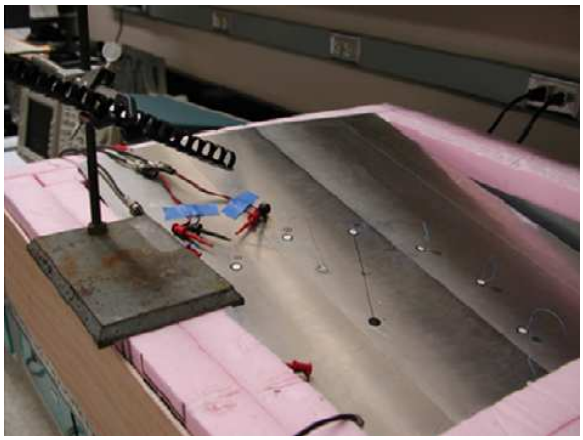

Figure 2.18: Experimental set-up, from Kundu's work (Kundu *et al.* [2009])

for complex structure, it cannot provide an optimum solution (Sung *et al.* [2000]).

2.3.2 Impact Source Localization Methods in Anisotropic Media

Triangulation techniques are not suitable for anisotropic materials, as they are strongly limited by the assumption that wave velocity is constant in all directions, but this is not true in anisotropic and inhomogeneous materials. Indeed, the group velocity (c_g) is function of the signal frequency (f) that depends on the impact speed of the object hitting the structure and the heading angle (θ). Paget et al. (Paget *et al.* [2003]) and Kurokawa et al. (Kurokawa *et al.* [2005]) developed an algorithm for impact location based on elliptical group velocity pattern defined by the following equation (Fig. 2.19):

$$c_g(f,\theta) = \frac{c_{g0} \cdot c_{g90}}{\sqrt{c_{g0}^2 sin^2(\theta) + c_{g90}^2 cos^2(\theta)}} \tag{2.9}$$

This method requires the knowledge of the group velocities at 0 (c_g0) and 90 degrees (c_{g90}) with respect to the planar reference frame, and it can be used for quasi-isotropic and unidirectional composite plates. Meo et al. (Meo *et al.* [2005]) employed such technique to find the impact source in sandwich panels. Seydel and Chang (Seydel & Chang [2001]) proposed a *model-based method* for the recon-

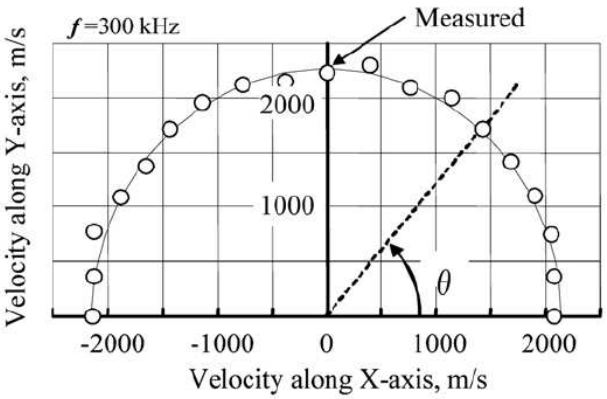

Figure 2.19: Elliptical angular-group velocity pattern, from (Kurokawa *et al.* [2005])

struction of the force history and the identification of the impact location, based on the minimization of the difference between the actual and predicted response from PZT. Although this method was applied to any kind of anisotropic material, even with complex geometries, it required the knowledge of the mechanical properties of the medium and a theoretical model for the simulation of dynamic-acoustic behaviour of the structure. For geometrically complex anisotropic structures, Matt and Lanza di Scalea (Matt & di Scalea F. [2007]) developed a method to locate low-velocity impact sources through the intersection of the wave paths detected by two rosettes of rectangular MFC transducers. Then, Salamone et al (Salamone *et al.* [2010]) extended such methodology to high-velocity impacts.

2.4 Imaging Methods

Literature provides a quantitative number of diagnostic *imaging methods* that can continuously provide a detailed image of the status of the damage and the location of the impact point. One type of algorithm is based upon a *damage index* (Ihn & Chang [2008a]) (Fig. 2.20), which is a measure of how different the current signal is from a baseline. This approach use the *artificial intelligence* (AI) method to generate an image for visualizing scattering locations and estimating the size of various type of damage. A second algorithm is the *ellipse method* (Michaels & Michaels [2007]) wherein differenced signals from all transducer pairs are delayed

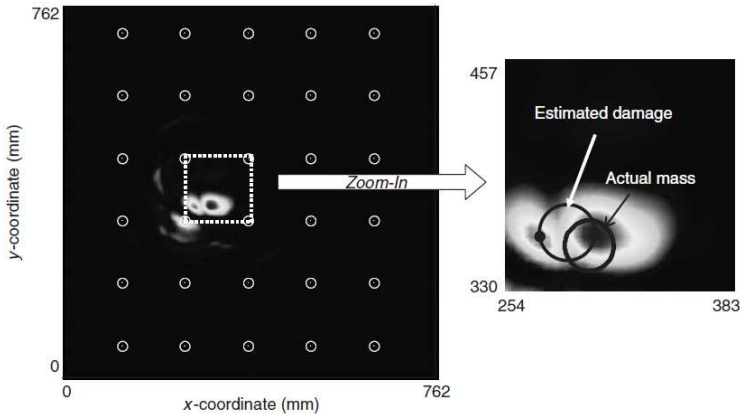

Figure 2.20: Damage estimation by diagnostic imaging with damage index, from (Ihn & Chang [2008a])

and summed for each spatial point in the image. For a single transducer pair, this imaging algorithm maps a single echo to an ellipse with the foci of the ellipse being the transmitter-receiver location. As additional pairs are added, the ellipses intersect at defect location and thus reinforce. A third algorithm (Croxford *et al.* [2007]), known as *hyperbola method*, is based on the proposition that the received waveform at two sensing transducer, as actuated by the same transmitting transducer, can be correlated according to the time difference in the time of flight from a given region to each of the receiver sensor. The maximum correlation corresponds to a serious of hyperbole that crosses the location of the defect with the foci on the two receiver transducers. All these algorithms rely on the fact that active ultrasonic signals are repeatable and the time origin of the excitation, as well as the group speeds, are known.

Another imaging technique is the *tomography* (Leonard *et al.* [2002]), wherein an image representing changes of physical quantities of the object under investigation, can be obtained through data collected from acoustic waves (e.g. attenuation or wave speed in *transmission tomography* or acoustic impedance mismatch in *reflection tomography*). Usually each transducer is used as a both, actuator and receiver, resulting N^2 *ray paths* if the number of transducer is N. Generally, there are two major classes of tomography imaging techniques:

- *Transform Based Methods* (TBM) that use the Fourier-slice theorem and

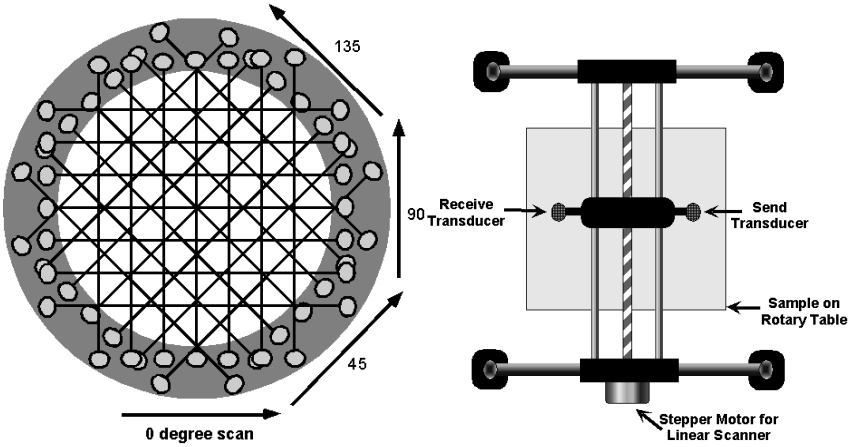

(a) (b)

Figure 2.21: Geometry (a) and scanning system (b) for parallel-projection tomography for the case of seven parallel projections at four orientations, from (Leonard *et al.* [2002]).

the Fourier diffraction theorem for non diffracting and diffracting sources, respectively (Hutchins *et al.* [1993]). These methods are fast but have the restriction that the data must be acquired on evenly spaced sets of straight rays known as *projections* (Fig. 2.21).

- *Algebraic Reconstruction Technique* (ART) that employs iterative procedures to reconstruct an image (Malyarenko & Hinders [2000]).

Other related iterative techniques are SIRT (*Simultaneous Iterative Reconstruction Technique*) and SART (*Simultaneous Algebraic Reconstruction Technique*) (Leonard *et al.* [2002]). These techniques are less efficient than TBM but they have several advantages. They can be used with irregular sampling geometries, incomplete data sets, and may incorporate curved ray paths. It is noteworthy that all these techniques require a large number of sensors to scan the entire area for image construction, which may limit their applications for *in-situ* damage identification.

Over the past 30 years, "*migration*" technique was applied to SHM systems in order to recover the location and shape of reflecting, refracting and diffracting defects (Lin & Yuan [1999]). This method, deriving from geophysics, is based on the idea that reconstruction of the image is made via numerical finite dif-

ference calculations. The signals recovered by the receivers (positioned along a line including the emitter) are time-reversed, back-propagated and "stacked" to create image snapshots of the displacement field, in particular at the moment at which all back-propagated waves precisely converge on the defect. An image of the defect is thus obtained. Initially this technique was limited to only isotropic materials. Then, the method was applied to anisotropic composite materials (Wang & Yuan [2005]), wherein the group velocities were taken as a function of the propagation direction. This method was capable of imaging several defects present in a composite plate, and the quality of the defect image was improved by the use of several excitations from distinct transducers.

2.4.1 Time Reversal Method

Time Reversal (TR) theoretical description for elastic wave propagation was first introduced by the group of M. Fink at the *Laboratoire Ondes and Acosutique of the Universite de Paris VII Denis Diderot* during 1990s. Due to the time invariance and spatial reciprocity of linear wave equation in a lossless medium, in a TR experiment, an input signal can be focused back on the original source if the output received by a set of transducers is time reversed and re-emitted back onto the excitation point (Fink [1992]). TR has been widely used for the imaging of the impact source and linear and nonlinear scatterers in biomedical ultrasound applications, seismology, underwater acoustics and SHM systems (Zumpano & Meo [2007]).

2.4.1.1 Imaging Linear and Nonlinear Scatterers with Time Reversal

The earliest work on TR dedicated to localize and characterize scatterers in a multiple scattering medium was carried out by the group at the University of Paris VII, who developed three different techniques, ITRM (Iterative TR Method) (Prada *et al.* [1991]), DORT (Decomposition of the TR Operator) (Prada *et al.* [1996]) and MUSIC (MUltiple SIgnal Classification scheme) methods (Gruber *et al.* [2004]). Although ITRM can only illuminate only the strongest scatterer presents on the medium, both DORT and MUSIC are based on the *Singular Value Decomposition* (SVD) of the transfer matrix of the structure, which allows

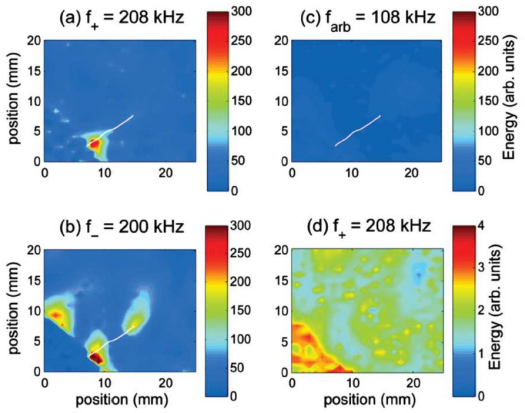

Figure 2.22: Imaging of the crack on an elastic medium using a combination of TR and NEWS technique, from Ulrich *et al.* [2007]

extracting for each frequency a set of N number (singular values) related to the reflectivity of a specific scatterer present in the medium. Then, each singular value is associated to a set of N signals, which are the Fourier transforms of the waveforms used to focus on the singular scatterer (Barbieri & Meo [2010]). However, such methods were used to localize only linear scatterers as boundary reflections and mode conversion in complex structures. In addition, with these methodologies, the number of transducers must be the equal or grater than the number of targets to be illuminated, which limits their use in SHM applications. Over the last ten years, much work on SHM techniques with NEWS and TR has been conducted by Los Alamos National Laboratories, in collaboration with a number of other institutions. A first method, called TREND (Time Reversal Elastic Nonlinear Diagnostic), was applied to the analysis of complex superficial cracks in a bounded medium, by measuring with a scanner laser vibrometer the harmonic/sidebands content of the retro-focusing waveforms after a TR operation (Ulrich *et al.* [2006]). A second technique employs only the harmonic filtered nonlinear components of narrow frequency band sources, in order to illuminate only nonlinear scatterers, such as micro-cracks (Goursolle *et al.* [2007], Ulrich *et al.* [2007]) (Fig. 2.22). Beside these mentioned methods, novel signal processing techniques were associated to TR in order to enhance the focusing of nonlinearities. Scalerandi et al. (Scalerandi *et al.* [2008]) developed a nonlinear imaging method based on a combination of TR and *Scaling Subtraction Method*

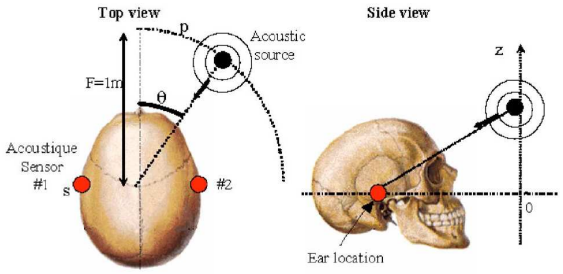

Figure 2.23: Sound localization within a skull, from Catheline *et al.* [2007]

(SSM). This last technique relies on the analysis of the differences of two received waveforms, one with very low excitation amplitude (approximated to a linear signal) and the other with larger excitation amplitude linearly scaled. The difference between two waveforms acquired is a signal sum of three contributions that takes into account not only the higher harmonic effects, but also nonlinear attenuation mechanisms and amplitude dependence on the wave speed. These last two phenomena mostly affect the fundamental frequency. Furthermore, TR was combined to *Phase Inversion* (PI) method to improve the extraction of nonlinear response in the recorded waveforms compared to a simple Butterworth filter, and the re-focusing at the nonlinear scatterer location (Ulrich *et al.* [2008]). PI, already used in landmines detection (Sutin *et al.* [2009]), eliminates the linear part and odd nonlinear harmonics contribution, taking into account only the even nonlinear harmonic part (second order nonlinearity). Indeed, the only operation performed in PI is the sum of two excitation signals with same amplitude, but phase-inverted (0 and 180 degrees).

2.4.1.2 Imaging of the Impact Source with Time Reversal

Some experimental works have employed TR to compensate the dispersive behaviour of guided Lamb waves (Park *et al.* [2009]). Indeed, depending on the propagation frequency, dispersive guided Lamb modes have a number of wave packets that travel at higher and lower speed towards the receivers. After a TR process, the slower modes are re-emitted first, so that all the wave packets can converge at the original source point at the same time, thus compensating the dispersion. The idea of using the time reversal concept for impact detection was

originally developed by Ing et al. (Ing *et al.* [2005]) for the detection of a finger knock on a glass plate. Then, this method was extended to the localization of the reverberated sounds in a human skull in order to understand the spatial positioning of pulses emitted by a loudspeaker (Catheline *et al.* [2007]) (Fig. 2.23). An imaging technique of the impact point with TR was also exploited for open spaces (Parot [2008]) and wireless communication systems (Jin *et al.* [2008]).

Chapter 3

Fundamentals of Guided Elastic Waves in Solids

Due to their capability of carrying energy over long distances, ultrasonic GW have found a considerable interest for the characterization of material properties in both isotropic and anisotropic plates. Indeed, SHM systems based on guided Lamb waves with integrated components (sensors and probes) are addressed to provide a real-time warning of the structural health status, thus ensuring high reliability and a global inspection of large structures. Guided Lamb waves are specific types of elastic waves confined by the boundaries of plate or pipe structures and are analytically described through exact solutions known as Rayleigh-Lamb relations. Such transcendental equations are based upon the superposition of bulk waves and show how the wave numbers or the velocities of the waves vary with the frequency. In this chapter the Rayleigh-Lamb relations for isotropic media are mathematically formulated (Sec. 3.2). Then, in order to generalize the analysis of dispersion of guided Lamb waves to multilayered anisotropic plates, a semi-analytical spectral finite element model (SFEM) is presented (Sec. 3.3).

3.1 The Wave Equation in Elastodynamics

In order to understand the guided Lamb wave solutions in a bounded isotropic material, the wave propagation in an unbounded medium is first introduced.

Referring to Lagrangian coordinates x_j, the equation of motion in *Classical Linear Elasticity* (CLE) can be obtained by combining the force equilibrium [Eq. (3.1a)] and the linear Hooks law [Eq. (3.1b)] in absence of body force f_i (Achenbach [1984]):

$$\frac{\partial \sigma_{ij}}{\partial x_j} = \rho \frac{\partial^2 u_i}{\partial t^2} \tag{3.1a}$$

$$\sigma_{ij} = C_{ijkl} \epsilon_{kl} \tag{3.1b}$$

where σ_{ij} is the Cauchy stress tensor, u_i the displacement, ϵ_{kl} the strain, ρ the material density and C_{ijkl} the fourth-order elasticity tensor. The strain-displacement relation using the compact notation is:

$$\epsilon_{kl} = \frac{1}{2} \left(\frac{\partial u_l}{\partial x_k} + \frac{\partial u_k}{\partial x_l} \right) \tag{3.2}$$

A combination of Eqs. (3.1a), (3.1b) and (3.2) leads to the following linear system:

$$\rho \frac{\partial^2 u_i}{\partial t^2} = \frac{1}{2} C_{ijkl} \frac{\partial}{\partial x_j} \left(\frac{\partial u_l}{\partial x_k} + \frac{\partial u_k}{\partial x_l} \right) \tag{3.3}$$

Decoupling between longitudinal and transverse components Eq. (3.1b) for linearly elastic, homogeneous and isotropic materials, we have:

$$\sigma_{ij} = \lambda \epsilon_{kk} \delta_{ij} + 2\mu \epsilon_{ij} = \lambda \frac{\partial u_k}{\partial x_k} \delta ij + \mu \left(\frac{\partial u_i}{\partial x_j} + \frac{\partial u_j}{\partial x_i} \right) \tag{3.4}$$

where $\lambda = \frac{\nu E}{(1+\nu)(1-2\nu)}$ is the bulk modulus, $\mu = \frac{E}{2(1+\nu)}$ is the shear modulus, E is the Young's modulus, ν is the Poisson's coefficient and $\delta = 1$ if $i = j$, $\delta = 0$ if $i \neq j$ is the Kronecker delta. Eq. (3.4) can be expressed as six scalar equations

in terms of the displacement field $u_i = \{u_x, u_y, u_z\}^T$:

$$\begin{aligned}
\sigma_{xx} &= \lambda\left(\epsilon_x + \epsilon_y + \epsilon_z\right) + 2\mu\epsilon_x = \lambda\left(\frac{\partial u_x}{\partial x} + \frac{\partial u_y}{\partial y} + \frac{\partial u_z}{\partial z}\right) + 2\mu\frac{\partial u_x}{\partial x} \\
\sigma_{yy} &= \lambda\left(\epsilon_x + \epsilon_y + \epsilon_z\right) + 2\mu\epsilon_y = \lambda\left(\frac{\partial u_x}{\partial x} + \frac{\partial u_y}{\partial y} + \frac{\partial u_z}{\partial z}\right) + 2\mu\frac{\partial u_y}{\partial y} \\
\sigma_{zz} &= \lambda\left(\epsilon_x + \epsilon_y + \epsilon_z\right) + 2\mu\epsilon_z = \lambda\left(\frac{\partial u_x}{\partial x} + \frac{\partial u_y}{\partial y} + \frac{\partial u_z}{\partial z}\right) + 2\mu\frac{\partial u_z}{\partial z} \\
\tau_{xy} &= 2\mu\epsilon_{xy} = \mu\left(\frac{\partial u_x}{\partial y} + \frac{\partial u_y}{\partial x}\right) \\
\tau_{yz} &= 2\mu\epsilon_{yz} = \mu\left(\frac{\partial u_y}{\partial z} + \frac{\partial u_z}{\partial y}\right) \\
\tau_{zx} &= 2\mu\epsilon_{zx} = \mu\left(\frac{\partial u_z}{\partial x} + \frac{\partial u_x}{\partial z}\right)
\end{aligned} \tag{3.5}$$

The linear elastodynamics wave equation is obtained differentiating Eq. (3.4) and substituting into Eq. (3.1a):

$$\rho\frac{\partial^2 u_i}{\partial t^2} = \frac{\partial}{\partial x_i}\left(\lambda\frac{\partial u_k}{\partial x_k}\right) + \mu\frac{\partial^2 u_i}{\partial x_k^2} + \frac{\partial}{\partial x_i}\left(\mu\frac{\partial u_k}{\partial x_k}\right) = (\lambda+\mu)\frac{\partial^2 u_k}{\partial x_i \partial x_k} + \mu\frac{\partial^2 u_i}{\partial x_k^2} \tag{3.6}$$

and in terms of the three scalar equations:

$$\begin{aligned}
\rho\frac{\partial^2 u_x}{\partial t^2} &= (\lambda+\mu)\frac{\partial}{\partial x}\left(\frac{\partial u_x}{\partial x} + \frac{\partial u_y}{\partial y} + \frac{\partial u_z}{\partial z}\right) + \mu\left(\frac{\partial^2 u_x}{\partial x^2} + \frac{\partial^2 u_x}{\partial y^2} + \frac{\partial^2 u_x}{\partial z^2}\right) \\
\rho\frac{\partial^2 u_y}{\partial t^2} &= (\lambda+\mu)\frac{\partial}{\partial y}\left(\frac{\partial u_x}{\partial x} + \frac{\partial u_y}{\partial y} + \frac{\partial u_z}{\partial z}\right) + \mu\left(\frac{\partial^2 u_y}{\partial x^2} + \frac{\partial^2 u_y}{\partial y^2} + \frac{\partial^2 u_y}{\partial z^2}\right) \\
\rho\frac{\partial^2 u_z}{\partial t^2} &= (\lambda+\mu)\frac{\partial}{\partial z}\left(\frac{\partial u_x}{\partial x} + \frac{\partial u_y}{\partial y} + \frac{\partial u_z}{\partial z}\right) + \mu\left(\frac{\partial^2 u_z}{\partial x^2} + \frac{\partial^2 u_z}{\partial y^2} + \frac{\partial^2 u_z}{\partial z^2}\right)
\end{aligned} \tag{3.7}$$

The invariant form of Eq. (3.6), known as *Navier's equation*, becomes (Auld [1973]):

$$\rho\frac{\partial^2 \mathbf{u}(\mathbf{r},t)}{\partial t^2} = (\lambda+\mu)\nabla\left[\nabla\cdot\mathbf{u}(\mathbf{r},t)\right] + \mu\nabla^2\mathbf{u}(\mathbf{r},t) \tag{3.8}$$

where $\mathbf{r} = x\hat{i} + y\hat{j} + z\hat{n}$ and $\nabla^2 = \left(\frac{\partial^2}{\partial x^2}\hat{i} + \frac{\partial^2}{\partial y^2}\hat{j} + \frac{\partial^2}{\partial z^2}\hat{n}\right)$ is the Laplacian operator. Eq. (3.8) can be rewritten as:

$$\rho\frac{\partial^2\mathbf{u}(\mathbf{r},t)}{\partial t^2} = \rho c_l^2\nabla\left[\nabla\cdot\mathbf{u}(\mathbf{r},t)\right] + \rho c_t^2\left[\nabla^2\mathbf{u}(\mathbf{r},t) - \nabla\cdot\mathbf{u}(\mathbf{r},t)\right] \tag{3.9}$$

or

$$\rho\frac{\partial^2\mathbf{u}(\mathbf{r},t)}{\partial t^2} = \rho c_l^2 M^l\mathbf{u}(\mathbf{r},t) + \rho c_t^2 M^t\mathbf{u}(\mathbf{r},t) \tag{3.10}$$

where $M^l\mathbf{u} = \nabla(\nabla\cdot\mathbf{u})$, $M^t\mathbf{u} = \nabla^2\mathbf{u} - \nabla\cdot\mathbf{u} = -\nabla\times\nabla\times\mathbf{u}$, $c_l^2 = (\lambda+2\mu)/\rho$ is the longitudinal wave velocity and $c_t^2 = \mu/\rho$ is the transverse wave speed. A solution of Eq. (3.10) is[1]:

$$\mathbf{u}(\mathbf{r},t) = M^l\mathbf{u}^l(\mathbf{r},t) + M^t\mathbf{u}^t(\mathbf{r},t) \tag{3.11}$$

and substituting Eq. (3.11) into (3.10) we have:

$$\rho M^l\left[c_l^2\nabla^2\mathbf{u}^l(\mathbf{r},t) - \frac{\partial^2\mathbf{u}^l(\mathbf{r},t)}{\partial t^2}\right] + \rho M^t\left[c_t^2\nabla^2\mathbf{u}^t(\mathbf{r},t) - \frac{\partial^2\mathbf{u}^t(\mathbf{r},t)}{\partial t^2}\right] = 0 \tag{3.12}$$

Therefore, the Navier's equation will be satisfied if:

$$\begin{aligned} c_l^2\nabla^2\mathbf{u}^l(\mathbf{r},t) - \frac{\partial^2\mathbf{u}^l(\mathbf{r},t)}{\partial t^2} &= 0 \\ c_t^2\nabla^2\mathbf{u}^t(\mathbf{r},t) - \frac{\partial^2\mathbf{u}^t(\mathbf{r},t)}{\partial t^2} &= 0 \end{aligned} \tag{3.13}$$

which represent the longitudinal and transverse (shear) differential linear wave equations, respectively.

[1] $M^l\left(M^t\mathbf{u}\right) = M^t\left(M^l\mathbf{u}\right) = 0$
$M^l\left(M^l\mathbf{u}\right) = M^l\left(\nabla^2\mathbf{u}\right)$
$M^t\left(M^t\mathbf{u}\right) = M^t\left(\nabla^2\mathbf{u}\right)$

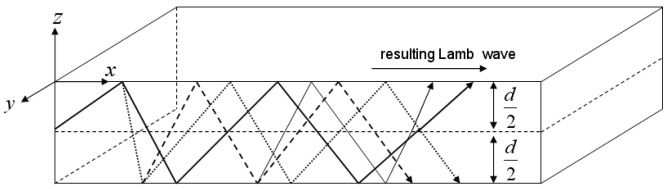

Figure 3.1: Lamb wave propagation within a thin isotropic plate plate. Propagating wave packets are superpositions of extensional and flexural modes

3.2 Ultrasonic Guided Lamb Waves in Isotropic Elastic Media

The guided Lamb wave problem can be solved by using the potential method (*Helmholtz decomposition*) of an elastic body in absence of body forces applied to Eq. (3.8). Indeed, the time harmonic displacement can be written as the sum of the gradient of a scalar potential Φ and the curl of a vector potential $\mathbf{\Psi}$ (Viktorov [1967]):

$$\mathbf{u} = \nabla\Phi + \nabla \times \mathbf{\Psi} \tag{3.14}$$

where $\nabla\Phi = \frac{\partial\Phi}{\partial x}\hat{i} + \frac{\partial\Phi}{\partial y}\hat{j} + \frac{\partial\Phi}{\partial z}\hat{n}$ and $\nabla \times \mathbf{\Psi} = \left(\frac{\partial\Psi_z}{\partial y} - \frac{\partial\Psi_y}{\partial z}\right)\hat{i} + \left(\frac{\partial\Psi_x}{\partial z} - \frac{\partial\Psi_z}{\partial x}\right)\hat{j} + \left(\frac{\partial\Psi_y}{\partial x} - \frac{\partial\Psi_x}{\partial y}\right)\hat{n}$. Assuming a time harmonic wave motion propagating in the positive x-direction of a bounded isotropic medium with thickness d (Fig. 3.1), we have:

$$\Phi = \phi e^{i(kx-\omega t)} \tag{3.15a}$$

$$\mathbf{\Psi} = \psi e^{i(kx-\omega t)} \tag{3.15b}$$

where $i = \sqrt{-1}$, $k = \omega/c_{ph}$ is the wave number, ω the angular frequency and c_{ph} the phase velocity, either longitudinal or transverse. It must be observed that displacement and velocity components are in the x and z-directions (*sagittal plane*). According to Eq. (3.5) and (3.14) the components u_x and u_z of the displacements along the x and z-direction, as well as the stress components σ_{xx},

σ_{xz} and σ_{zz} can be described in terms of Φ and $\mathbf{\Psi}$:

$$u_x = \frac{\partial \Phi}{\partial x} - \frac{\partial \Psi_y}{\partial z} \tag{3.16a}$$

$$u_z = \frac{\partial \Phi}{\partial z} + \frac{\partial \Psi_y}{\partial x} \tag{3.16b}$$

$$\sigma_{xx} = \lambda \left(\frac{\partial^2 \Phi}{\partial x^2} + \frac{\partial^2 \Phi}{\partial z^2} \right) + 2\mu \left(\frac{\partial^2 \Phi}{\partial x^2} - \frac{\partial^2 \Psi_y}{\partial x \partial z} \right) \tag{3.16c}$$

$$\sigma_{zz} = \lambda \left(\frac{\partial^2 \Phi}{\partial x^2} + \frac{\partial^2 \Phi}{\partial z^2} \right) + 2\mu \left(\frac{\partial^2 \Phi}{\partial z^2} + \frac{\partial^2 \Psi_y}{\partial x \partial z} \right) \tag{3.16d}$$

$$\sigma_{xz} = \mu \left(2\frac{\partial^2 \Phi}{\partial x \partial z} + \frac{\partial^2 \Psi_y}{\partial x^2} - \frac{\partial^2 \Psi_y}{\partial z^2} \right) \tag{3.16e}$$

Substituting Eq. (3.14) in (3.8), we obtain:

$$\rho \left[\frac{\partial^2 \Phi}{\partial t^2} + \frac{\partial^2 \left(\nabla \times \mathbf{\Psi} \right)}{\partial t^2} \right] = (\lambda + \mu) \nabla \left(\nabla^2 \Phi \right) + \mu \nabla^2 \left(\nabla \Phi \right) + \mu \nabla^2 \left(\nabla \times \mathbf{\Psi} \right) \tag{3.17}$$

and according to the Schwarz theorem, i.e. $\nabla \times (\nabla \Phi) = 0$ and $\nabla \cdot (\nabla \times \mathbf{\Psi}) = 0$, Eq. (3.17) can be rewritten as:

$$\nabla \left[\rho \frac{\partial^2 \Phi}{\partial t^2} - (\lambda + 2\mu) \nabla^2 \Phi \right] + \nabla \times \left[\rho \frac{\partial^2 \mathbf{\Psi}}{\partial t^2} - \mu \nabla^2 \mathbf{\Psi} \right] = 0 \tag{3.18}$$

Since the first term of Eq. (3.18) is purely a scalar and the latter purely a vector, the two terms can be separately equal to zero:

$$\left(\nabla^2 - \frac{1}{c_l^2} \frac{\partial^2}{\partial t^2} \right) \Phi = 0 \tag{3.19a}$$

$$\left(\nabla^2 - \frac{1}{c_t^2} \frac{\partial^2}{\partial t^2} \right) \mathbf{\Psi} = 0 \tag{3.19b}$$

The motion does not depend on the y-coordinate and the potential vector can expressed by simply its component along the y-axis (Ψ_y or simply Ψ). In addition, using the *Helmholtz identity* (Barton [1989]) to reduce the complexity of the

analysis and assuming:

$$\phi = \phi(z) \tag{3.20a}$$

$$\psi = \psi(z) \tag{3.20b}$$

we obtain a time-independent form of the original Eqs. (3.19a-3.19b):

$$\begin{cases} \frac{\partial^2 \Phi}{\partial x^2} + \frac{\partial^2 \Phi}{\partial z^2} + k_l^2 \Phi = 0 \\ \frac{\partial^2 \Psi}{\partial x^2} + \frac{\partial^2 \Psi}{\partial z^2} + k_t^2 \Psi = 0 \end{cases} \tag{3.21}$$

where $k_l^2 = (\omega/c_l)^2 = [\omega^2 \rho/(\lambda + 2\mu)]$ and $k_t^2 = (\omega/c_t)^2 = (\omega^2 \rho/\mu)$. Substituting Eqs. (3.15a-3.15b) in (3.21) according with Eqs. (3.20a-3.20b), we have:

$$\begin{cases} \frac{\partial^2 \phi(z)}{\partial z^2} - (k^2 - k_l^2)\,\phi(z) = 0 \\ \frac{\partial^2 \psi(z)}{\partial z^2} - (k^2 - k_t^2)\,\psi(z) = 0 \end{cases} \tag{3.22}$$

Solving the above system of differential equations for the unknown amplitude functions $\phi(z)$ and $\psi(z)$, the following solutions are obtained:

$$\phi(z) = Ae^{\sqrt{(k^2 - k_l^2)}z} + Be^{-\sqrt{(k^2 - k_l^2)}z} \tag{3.23a}$$

$$\psi(z) = Ce^{\sqrt{(k^2 - k_t^2)}z} + De^{-\sqrt{(k^2 - k_t^2)}z} \tag{3.23b}$$

Assuming $k^2 > k_t^2 > k_l^2$, only the solution with positive exponent correspond to motion increasing with the depth (*Lamb waves*). Hence, the expressions of Φ and Ψ become[2]:

$$\Phi = [A_1 \cosh(rz) + A_2 \sinh(rz)]\, e^{i(kx - \omega t)} \tag{3.24a}$$

$$\Psi = [A_3 \cosh(sz) + A_4 \sinh(sz)]\, e^{i(kx - \omega t)} \tag{3.24b}$$

where A_1, A_2, A_3 and A_4 are constant amplitudes unknown, $r = \sqrt{(k^2 - k_l^2)}$

[2] $cos(iy) = \frac{e^{-y} + e^{y}}{2} = cosh(y)$
$sin(iy) = \frac{e^{-y} - e^{y}}{2i} = isinh(y)$
$cos(iy) - isin(iy) = cosh(y) + sinh(y) = e^{y}$

and $s = \sqrt{(k^2 - k_t^2)}$. Substituting Eqs. (3.24a-3.24b) into (3.16a-3.16e) we get:

$$u_x = [ikA_1 \cosh(rz) + ikA_2 \sinh(rz) - sA_3 \sinh(sz) - sA_4 \cosh(sz)]\, e^{i(kx-\omega t)} \tag{3.25a}$$

$$u_z = [rA_1 \sinh(rz) + rA_2 \cosh(rz) + ikA_3 \cosh(sz) + ikA_4 \sinh(sz)]\, e^{i(kx-\omega t)} \tag{3.25b}$$

$$\begin{aligned}\sigma_{xx} = \{ &\left[(\lambda + 2\mu)r^2 - \lambda k^2\right] A_1 \cosh(rz) + \left[(\lambda + 2\mu)r^2 - \lambda k^2\right] A_2 \sinh(rz) \\ &-2\mu iksA_3 \sinh(sz) - 2\mu iksA_4 \cosh(sz)\}\, e^{i(kx-\omega t)}\end{aligned} \tag{3.25c}$$

$$\begin{aligned}\sigma_{zz} = \{ &\left[(\lambda + 2\mu)r^2 - \lambda k^2\right] A_1 cosh(rz) + \left[(\lambda + 2\mu)r^2 - \lambda k^2\right] A_2 \sinh(rz) \\ &+2\mu iksA_3 \sinh(sz) + 2\mu iksA_4 \cosh(sz)\}\, e^{i(kx-\omega t)}\end{aligned} \tag{3.25d}$$

$$\begin{aligned}\sigma_{xz} = \{ &2\mu ikrA_1 \sinh(rz) + 2\mu ikrA_2 \cosh(rz) - \mu\left(k^2 + s^2\right) A_3 \cosh(sz) \\ &-\mu\left(k^2 + s^2\right) A_4 \sinh(sz)\}\, e^{i(kx-\omega t)}\end{aligned} \tag{3.25e}$$

Hence, in order to obtain the four unknown amplitudes, the traction-free boundary conditions are applied on the front/back surface of the plate:

$$\sigma_{xz} = 0 \quad \rightarrow \quad z{=}d/2 \qquad\qquad \sigma_{xz} = 0 \quad \rightarrow \quad z{=}{-}d/2 \tag{3.26a}$$

$$\sigma_{zz} = 0 \quad \rightarrow \quad z{=}d/2 \qquad\qquad \sigma_{zz} = 0 \quad \rightarrow \quad z{=}{-}d/2 \tag{3.26b}$$

The following system of linear and homogeneous equations is thus obtained:

$$\begin{aligned}
&\left(k^2+s^2\right)\cosh\left(\frac{rd}{2}\right)A_1+\left(k^2+s^2\right)\sinh\left(\frac{rd}{2}\right)A_2+2iks\sinh\left(\frac{sd}{2}\right)A_3\\
&\qquad+2iks\cosh\left(\frac{sd}{2}\right)A_4=0\\
&\left(k^2+s^2\right)\cosh\left(\frac{rd}{2}\right)A_1-\left(k^2+s^2\right)\sinh\left(\frac{rd}{2}\right)A_2-2iks\sinh\left(\frac{sd}{2}\right)A_3\\
&\qquad-2iks\cosh\left(\frac{sd}{2}\right)A_4=0\\
&2ikr\sinh\left(\frac{rd}{2}\right)A_1+2ikr\cosh\left(\frac{rd}{2}\right)A_2-\left(k^2+s^2\right)\cosh\left(\frac{sd}{2}\right)A_3\\
&\qquad-\left(k^2+s^2\right)\sinh\left(\frac{sd}{2}\right)A_4=0\\
&-2ikr\sinh\left(\frac{rd}{2}\right)A_1+2ikr\cosh\left(\frac{rd}{2}\right)A_2-\left(k^2+s^2\right)\cosh\left(\frac{sd}{2}\right)A_3\\
&\qquad+\left(k^2+s^2\right)\sinh\left(\frac{sd}{2}\right)A_4=0
\end{aligned}\tag{3.27}$$

that can be rewritten as:

$$\begin{pmatrix}C_{11}&C_{12}&C_{13}&C_{14}\\C_{21}&C_{22}&C_{23}&C_{24}\\C_{31}&C_{32}&C_{33}&C_{34}\\C_{41}&C_{42}&C_{43}&C_{44}\end{pmatrix}\begin{pmatrix}A_1\\A_2\\A_3\\A_4\end{pmatrix}=\begin{pmatrix}0\\0\\0\\0\end{pmatrix}\tag{3.28}$$

where $C_{11}-C_{44}$ are the elementary functions of stress fields within the system (3.27). Hence, the characteristic equation can be obtained by solving:

$$\det\begin{pmatrix}C_{11}&C_{12}&C_{13}&C_{14}\\C_{21}&C_{22}&C_{23}&C_{24}\\C_{31}&C_{32}&C_{33}&C_{34}\\C_{41}&C_{42}&C_{43}&C_{44}\end{pmatrix}=0\tag{3.29}$$

From the characteristic equation (3.29), the eigenvalues in the wave number k can be evaluated and two new expressions of Φ and Ψ as function of the coefficients

A_1 and A_2 can be obtained:

$$\Phi = \left[A_1 \cosh(rz) + A_2 \sinh(rz)\right] e^{i(kx-\omega t)} \tag{3.30a}$$

$$\Psi = \left[\frac{2ikr \cosh\left(\frac{rd}{2}\right)}{(k^2+s^2)\cosh\left(\frac{sd}{2}\right)} A_2 \cosh(sz) + \frac{2ikr \cosh\left(\frac{rd}{2}\right)}{(k^2+s^2)\cosh\left(\frac{sd}{2}\right)} A_1 \sinh(sz) \right] e^{i(kx-\omega t)} \tag{3.30b}$$

Since the potentials in Eqs. (3.30a-3.30b) involve sines and cosines of the argument z that are odd and even functions, the solutions for the displacements can be divided in two set of modes, known as symmetric (S_n) and antisymmetric (A_n). This means that the wave motion in the x-direction will be symmetric with respect to the mid-plane ($z = 0$) if u_x contains cosines, and it will be antisymmetric if u_x contains sines. The reverse is true for the motion in the z-direction.

Hence, the displacements calculated substituting Eqs. (3.30a-3.30b) into (3.25a-3.25b) are:

$$u_x = u_x^s + u_x^a \tag{3.31a}$$

$$u_z = u_z^s + u_z^a \tag{3.31b}$$

where:

$$u_x^s = A^s k \left[\frac{\cosh(rz)}{\sinh\left(\frac{rd}{2}\right)} - \frac{2rs}{(k^2+s^2)} \frac{\cosh(sz)}{\sinh\left(\frac{sd}{2}\right)} \right] e^{i\left(kx-\omega t-\frac{\pi}{2}\right)} \tag{3.32a}$$

$$u_x^a = A^a k \left[\frac{\sinh(rz)}{\cosh\left(\frac{rd}{2}\right)} - \frac{2rs}{(k^2+s^2)} \frac{\sinh(sz)}{\cosh\left(\frac{sd}{2}\right)} \right] e^{i\left(kx-\omega t-\frac{\pi}{2}\right)} \tag{3.32b}$$

$$u_z^s = -A^s r \left[\frac{\sinh(rz)}{\sinh\left(\frac{rd}{2}\right)} - \frac{2k^2}{(k^2+s^2)} \frac{\sinh(sz)}{\sinh\left(\frac{sd}{2}\right)} \right] e^{i(kx-\omega t)} \tag{3.32c}$$

$$u_z^a = -A^a r \left[\frac{\cosh(rz)}{\cosh\left(\frac{rd}{2}\right)} - \frac{2k^2}{(k^2+s^2)} \frac{\cosh(sz)}{\cosh\left(\frac{sd}{2}\right)} \right] e^{i(kx-\omega t)} \tag{3.32d}$$

with A^s and A^a new arbitrary amplitudes. The phase velocities or wave numbers of Lamb waves can be expressed as function of the frequency-thickness product

through the Rayleigh-Lamb frequency relations, known as the dispersion equations:

for *symmetrical modes*

$$\frac{tan\left(\frac{qd}{2}\right)}{tan\left(\frac{pd}{2}\right)} + \frac{4k^2qp}{\left(q^2-k^2\right)^2} = 0 \tag{3.33}$$

for *antisymmetrical modes*

$$\frac{tan\left(\frac{qd}{2}\right)}{tan\left(\frac{pd}{2}\right)} + \frac{\left(q^2-k^2\right)^2}{4k^2qp} = 0 \tag{3.34}$$

where $q = \sqrt{k_t^2 - k^2}$ and $p = \sqrt{k_l^2 - k^2}$. Relations analogous to Eqs. (3.33) and (3.34) can be found for the group velocity by assuming:

$$c_g = c_{ph} + k\frac{\partial c_{ph}}{\partial k} \tag{3.35}$$

where c_{ph} is the phase speed. Figures 3.2a and b illustrate the phase and group velocity dispersion curves, respectively, for an aluminium plates with thickness of 3 mm. Among the infinite Lamb modes, the fundamental flexural mode A_0 and the fundamental symmetric mode S_0, even if they can be generated for only low values of the product frequency-thickness, they do not present cut-off frequencies.

3.3 Guided Waves in Flat Multilayer Anisotropic Media

Theoretical studies on dispersion curves for guided waves have been carried out on isotropic ad anisotropic plates for over one hundred years (Mindlin [1959], Achenbach [1984]). More recently, the *transfer matrix* (Nayfeh [1991]) technique was used for modelling multilayered anisotropic media. Then, this method was extended to viscoelastic anisotropic laminates (*global matrix* method (Lowe [1995])). Such methods are based on the superposition of bulk waves, and the displacement field can be expressed as function of several parameters as the cross-section position in the layers, density, wave velocities and wavenumber. By applying

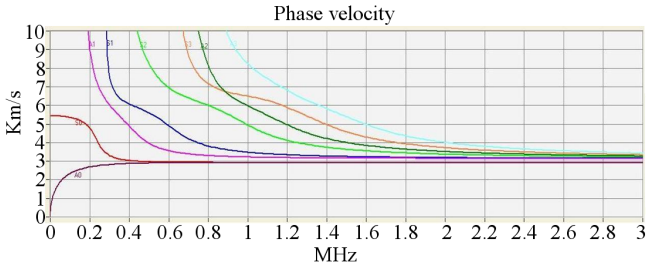

(a)

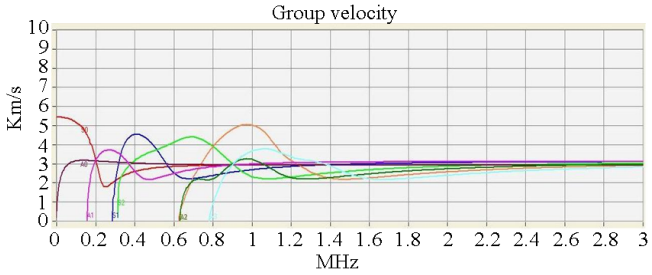

(b)

Figure 3.2: Phase velocity (a) and group velocity (b) dispersion curves for an aluminium plate with thickness of 3 mm.

the appropriate boundary conditions and imposing the continuity of stress and strain at each layer interface, the free-wave propagation in the laminate takes the form of a nonlinear transcendental eigenvalue problem. Nevertheless, in these techniques, the exact solution requires iterative root-searching algorithms that might miss some wave types. Hence, in order to avoid solving transcendental equations, 3-D approximated plate theories were employed for computing the dispersion relations of GW in simple anisotropic plate-like structures (Whitney & Pagano [1970], Reddy [1984], Wang & Yuan [2007]). However, the use of these plate theories is not valid for describing the GW modes at frequencies at which the wavelengths are comparable to the plate thickness (Jeong & Jang [2000]).

At low frequencies, the elastic wave propagation can be also revealed through numerical simulations. Indeed, finite element (FE) method was used to describe the displacements field across each element by using low-order polynomials (Cook *et al.* [1989]). However, as the element size is of the order of the wavelength, at higher frequencies and large meshes, conventional FE analysis becomes compu-

tationally too expensive. *Semi-analytical finite element*, also known as *spectral finite element* (SFEM) method, is a valid alternative to obtain dispersive curves for propagating waves of arbitrary thickness, with an acceptable computational cost (Hayashi *et al.* [2003], Shorter [2004]). In particular, this technique provides a description of the cross-sectional deformation of a laminate using a one-dimensional FE discretization of the cross-sectional displacement field. The displacements are approximated as harmonic exponential functions with the shape independent of frequency. The characteristic equation (SFEM solution) for free wave propagation is obtained in stable manner from a linear eigenvalue problem in wavenumber k, and the propagating wave field can be predicted for any kind of composite laminate or complex structures (Barbieri *et al.* [2009]).

3.3.1 Variational Fomulation of the Equations of Motions

The weak form of the differential equation of the elastodynamics is obtained from the variation of the Hamilton's principle as follows:

$$\delta \int_{t_1}^{t_2} (E_K + E_P)\, dt = 0 \tag{3.36}$$

where E_K is the time-average kinetic energy and E_P is the potential energy. If Ω is the volume of the laminate (waveguide's cross-sectional domain), then:

$$E_K = \frac{1}{2} \int_{\Omega} \dot{\mathbf{u}}^T \rho \dot{\mathbf{u}} d\Omega \tag{3.37}$$

where $\dot{\mathbf{u}} = \partial \mathbf{u}/\partial t$, $\mathbf{u}$ is the displacements field, ρ is the mass density and the superscript T denotes the transpose operation. The potential energy or strain energy is given by:

$$E_P = \frac{1}{2} \int_{\Omega} \boldsymbol{\epsilon}^T \mathbf{C}_{\mathbf{x-y}} \boldsymbol{\epsilon} d\Omega \tag{3.38}$$

where $\boldsymbol{\epsilon}$ is the strain tensor and $\mathbf{C}_{\mathbf{x-y}}$ is the stiffness matrix in the laminate reference plane $x - y$. By integrating by parts the kinetic term, the variational

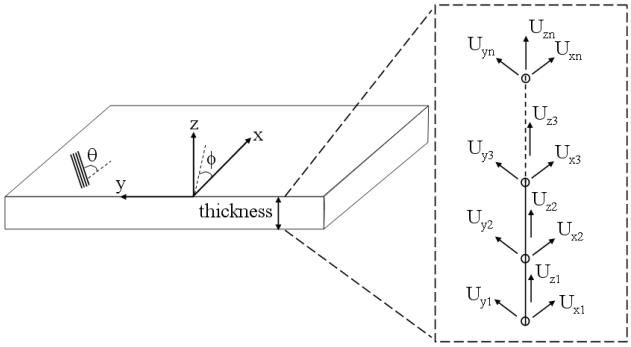

Figure 3.3: SFEM model of wave propagation. The inset represents the degrees of freedom of a 1-D two-node element

form of the elastodynamics equation is:

$$\int_{t_1}^{t_2} \left[\int_{\Omega} \delta\left(\boldsymbol{\epsilon}^T\right) \mathbf{C}_{\mathbf{x}-\mathbf{y}} \boldsymbol{\epsilon} d\Omega + \delta\left(\mathbf{u}^T\right) \rho \ddot{\mathbf{u}} d\Omega \right] = 0 \tag{3.39}$$

with $\ddot{\mathbf{u}} = \partial^2 \mathbf{u}/\partial t^2$. Assuming an harmonic motion of plane waves that propagates in the positive x-direction with angular frequency ω, wavenumber k and heading angle ϕ, the cross-sectional displacement field $\mathbf{u}(\zeta, t)$, with $\zeta = x, y, z$, in a full 3-D problem is (Fig. 3.3):

$$\mathbf{u}(\zeta, t) = \begin{pmatrix} u_x(\zeta, t) \\ u_y(\zeta, t) \\ u_z(\zeta, t) \end{pmatrix} = \begin{pmatrix} U_x(z) \\ U_y(z) \\ U_z(z) \end{pmatrix} e^{i(k_x - \omega t)} \tag{3.40}$$

where $k_x = [\cos(\phi)x + \sin(\phi)y]$ and the cross-section lies in the plane $y - z$.

3.3.2 Spectral Finite Element Formulation

The volume Ω of the laminate is discretized in a system of finite elements with domain $\Omega^{(e)}$. Hence, Eq. (3.40) can be written in terms of the polynomial shape functions $\mathbf{N}(z)$ and the complex amplitude of nodal displacement $\mathbf{q}^{(e)}$ (Barbieri

et al. [2009]):

$$\mathbf{u}^{(e)}(\zeta,t) = \begin{pmatrix} \sum_{j=1}^{n} N_j(z)U_{xn} \\ \sum_{j=1}^{n} N_j(z)U_{yn} \\ \sum_{j=1}^{n} N_j(z)U_{zn} \end{pmatrix}^{(e)} e^{i(k_x-\omega t)} = \mathbf{N}(z)\mathbf{q}^{(e)}e^{i(k_x-\omega t)} \tag{3.41}$$

where n is the number of nodes in the FE mesh. Since the one-dimensional mesh contains two nodes per element, a single element has six degrees of freedom. The shape function matrix (size 3×6) is:

$$\mathbf{N}(z) = \begin{pmatrix} \mathbf{N}_i(z) & 0 & 0 \\ 0 & \mathbf{N}_i(z) & 0 \\ 0 & 0 & \mathbf{N}_i(z) \end{pmatrix} \tag{3.42}$$

where

$$\mathbf{N}_i(z) = \begin{pmatrix} 1 - \frac{z}{L} & \frac{z}{L} \end{pmatrix}$$

It can be seen that the shape functions are linear in the element and fulfil the property to be interpolant of the nodal data, i.e. $\mathbf{N}_i(z) = \delta_{ij}$ where δ_{ij} is the Kronecker delta. The nodal unknown displacements are:

$$\mathbf{q}^{(e)} = \begin{pmatrix} U_{x1} & U_{y1} & U_{z1} & U_{x2} & U_{y2} & U_{z2} \end{pmatrix} \tag{3.43}$$

The strain vector for the element (e) is:

$$\boldsymbol{\epsilon}^{(e)}(\zeta,t) = \begin{pmatrix} \epsilon_{xx} \\ \epsilon_{yy} \\ \epsilon_{zz} \\ \epsilon_{xy} \\ \epsilon_{xz} \\ \epsilon_{yz} \end{pmatrix} = \nabla\mathbf{u}^{(e)}(\zeta,t) = \begin{pmatrix} \frac{\partial}{\partial x} & 0 & 0 \\ 0 & \frac{\partial}{\partial y} & 0 \\ 0 & 0 & \frac{\partial}{\partial z} \\ \frac{\partial}{\partial y} & \frac{\partial}{\partial x} & 0 \\ \frac{\partial}{\partial z} & 0 & \frac{\partial}{\partial x} \\ 0 & \frac{\partial}{\partial z} & \frac{\partial}{\partial y} \end{pmatrix} \mathbf{u}^{(e)}(\zeta,t) \tag{3.44}$$

and it can be represented as a function of the nodal displacements by substituting Eq. (3.41) in (3.44):

$$\boldsymbol{\epsilon}^{(e)}(\zeta,t) = \mathbf{F}(k,\phi,z)\mathbf{q}^{(e)}e^{i(k_x-\omega t)} \tag{3.45}$$

where the strain-displacement matrix (size 6×6) is given by:

$$\mathbf{F}(k,\phi,z) = \begin{pmatrix} -jk\cos(\phi)\mathbf{N}_i(z) & 0 & 0 \\ 0 & -jk\sin(\phi)\mathbf{N}_i(z) & 0 \\ 0 & 0 & \frac{\partial \mathbf{N}_i(z)}{\partial z} \\ 0 & \frac{\partial \mathbf{N}_i(z)}{\partial z} & -jk\sin(\phi)\mathbf{N}_i(z) \\ \frac{\partial \mathbf{N}_i(z)}{\partial z} & 0 & -jk\cos(\phi)\mathbf{N}_i(z) \\ -jk\sin(\phi)\mathbf{N}_i(z) & -jk\cos(\phi)\mathbf{N}_i(z) & 0 \end{pmatrix} \tag{3.46}$$

In order to extend this method to materials with arbitrary lay-up, a transformation between the laminate (O, x, y) reference frame and the lamina one (O, x_L, y_L) is required. Hence, the stiffness matrix in the laminate reference $\mathbf{C_{x-y}}$ is:

$$\mathbf{C_{x-y}} = \mathbf{R}_1\mathbf{C}_L\mathbf{R}_2 \tag{3.47}$$

with

$$\mathbf{R}_1 = \begin{pmatrix} m^2 & n^2 & 0 & 0 & 0 & 2mn \\ n^2 & m^2 & 0 & 0 & 0 & -2mn \\ 0 & 0 & 1 & 0 & 0 & 0 \\ 0 & 0 & 0 & m & -n & 0 \\ 0 & 0 & 0 & n & m & 0 \\ -mn & mn & 0 & 0 & 0 & m^2-n^2 \end{pmatrix} \tag{3.48a}$$

$$\mathbf{R}_2 = \begin{pmatrix} m^2 & n^2 & 0 & 0 & 0 & mn \\ n^2 & m^2 & 0 & 0 & 0 & -mn \\ 0 & 0 & 1 & 0 & 0 & 0 \\ 0 & 0 & 0 & m & -n & 0 \\ 0 & 0 & 0 & n & m & 0 \\ -2mn & 2mn & 0 & 0 & 0 & m^2-n^2 \end{pmatrix} \tag{3.48b}$$

with $m = \cos(\theta)$, $n = \sin(\theta)$ and $\mathbf{C_L}$ the stiffness matrix in the lamina reference frame. Recalling Hookes law [Eq. (3.1b)], the most general relation between the stress-strain matrices for linearly elastic problem can be written as:

$$\boldsymbol{\sigma}^{(e)}(\zeta, t) = \mathbf{C}_{\mathbf{x-y}}\boldsymbol{\epsilon}^{(e)}(\zeta, t) \tag{3.49}$$

and substituting Eqs. (3.45) and (3.47) in (3.49), we obtain:

$$\boldsymbol{\sigma}^{(e)}(\zeta, t) = \mathbf{F}(k, \phi, z)\mathbf{C}_{\mathbf{x-y}}\mathbf{q}^{(e)}e^{i(k_x - \omega t)} \tag{3.50}$$

The discrete form of the weak form of the Hamiltonian function is obtained computing a sum of integrals over element domains $\Omega^{(e)}$:

$$\int_{t_1}^{t_2} \left\{ \sum_{e=1}^{n_{el}} \left[\int_{\Omega^{(e)}} \delta\left(\boldsymbol{\epsilon}^{(e)T}\right) \boldsymbol{\sigma}^{(e)} d\Omega^{(e)} + \int_{\Omega^{(e)}} \delta\left(\mathbf{u}^{(e)T}\right) \rho^{(e)} \ddot{\mathbf{u}}^{(e)} d\Omega^{(e)} \right] \right\} dt = 0 \tag{3.51}$$

where n_{el} represents the number of elements present in the 1-D FE mesh. Substituting Eqs. (3.41), (3.45) and (3.50) in (3.51), the first terms of the above equations becomes (Chakraborty & Gopalakrishnan [2006]):

$$\begin{aligned} &\int_{\Omega^{(e)}} \delta\left(\boldsymbol{\epsilon}^{(e)T}\right) \boldsymbol{\sigma}^{(e)} d\Omega^{(e)} \\ &\quad = \int_{\Omega^{(e)}} \left\{ \delta\left[\mathbf{F}^T(k, \phi, z)\mathbf{q}^{(e)T} e^{-i(k_x - \omega t)}\right] \mathbf{F}(k, \phi, z)\mathbf{C}_{\mathbf{x-y}}\mathbf{q}^{(e)} e^{i(k_x - \omega t)} \right\} d\Omega^{(e)} \\ &\quad = \delta\mathbf{q}^{(e)T} \int_{\Omega^{(e)}} \left[\mathbf{F}^T(k, \phi, z)\mathbf{C}_{\mathbf{x-y}}\mathbf{F}(k, \phi, z)\right] \mathbf{q}^{(e)} d\Omega^{(e)} \end{aligned} \tag{3.52}$$

with $i^T = -i$. The second term of Eq. (3.51) is:

$$\begin{aligned}
&\int_{\Omega^{(e)}} \delta\left(\mathbf{u}^{(e)T}\right) \rho^{(e)} \ddot{\mathbf{u}}^{(e)} d\Omega^{(e)} \\
&\quad = -\int_{\Omega^{(e)}} \delta\left(\mathbf{N}^T(z)\mathbf{q}^{(e)T} e^{-i(k_x-\omega t)}\right) \rho^{(e)} \mathbf{N}(z) \omega^2 \mathbf{q}^{(e)} e^{i(k_x-\omega t)} d\Omega^{(e)} \\
&\quad = -\delta\mathbf{q}^{(e)T} \omega^2 \int_{\Omega^{(e)}} \left[\mathbf{N}^T(z) \rho^{(e)} \mathbf{N}(z)\right] \mathbf{q}^{(e)} d\Omega^{(e)}
\end{aligned} \tag{3.53}$$

A combination of Eqs. (3.52) and (3.53) yields:

$$\int_{t_1}^{t_2} \left\{ \sum_{e=1}^{n_{el}} \delta\mathbf{q}^{(e)T} \left[\mathbf{k}^{(e)}(k,\phi) - \omega^2 \mathbf{m}^{(e)}\right] \mathbf{q}^{(e)} \right\} dt = 0 \tag{3.54}$$

where:

$$\mathbf{k}^{(e)}(k,\phi) = \int_{\Omega^{(e)}} \left[\mathbf{F}^T(k,\phi,z) \mathbf{C}_{\mathbf{x-y}} \mathbf{F}(k,\phi,z)\right] d\Omega^{(e)} \tag{3.55}$$

is the *element stiffness matrix*,

$$\mathbf{m}^{(e)} = \int_{\Omega^{(e)}} \left[\mathbf{N}^T(z) \rho^{(e)} \mathbf{N}(z)\right] d\Omega^{(e)} \tag{3.56}$$

is the *element mass matrix*.

3.3.3 Wavenumber Evaluation

Applying the standard FE assembling procedure, the governing Eq. (3.54) becomes:

$$\int_{t_1}^{t_2} \left\{ \delta\mathbf{U}^T \left[\mathbf{K}(k,\phi) - \omega^2 \mathbf{M}\right] \mathbf{U} \right\} dt = 0 \tag{3.57}$$

where $\mathbf{U}$ is the global unknown nodal displacement vector and

$$\begin{aligned} \mathbf{K}(k,\phi) &= \sum_{e=1}^{n_{el}} \mathbf{k}^{(e)}(k,\phi) \\ \mathbf{M} &= \sum_{e=1}^{n_{el}} \mathbf{m}^{(e)} \end{aligned} \tag{3.58}$$

Since the strain stress matrix contains only linear terms in k, the stiffness matrix can be rewritten as:

$$\mathbf{K}(k,\phi) = \mathbf{K}_0(\phi) + \mathbf{K}_1(\phi) + \mathbf{K}_2(\phi)k^2 \tag{3.59}$$

Therefore, for every $\delta\mathbf{U}^T$, the elastodynamics-discretized equation of motion takes the form:

$$\left[\mathbf{K}_0(\phi) + \mathbf{K}_1(\phi) + \mathbf{K}_2(\phi)k^2 - \omega^2\mathbf{M}\right]_N \mathbf{U} = 0 \tag{3.60}$$

where the subscript N represents the number of total degrees of freedom of the system. If ω and ϕ are fixed, the quadratic eigenvalue problem for k [Eq. (3.60)] can be transformed into a linear eigenvalue problem by employing the transformation:

$$\mathbf{U}_2 = k\mathbf{U}_1 \tag{3.61a}$$

$$\mathbf{U}_1 = k\mathbf{U}_0 \tag{3.61b}$$

Inserting Eqs. (3.61a-3.61b) into (3.60), the following system of equations is obtained:

$$\begin{pmatrix} 0 & \mathbf{I} & 0 \\ 0 & 0 & \mathbf{I} \\ 0 & \mathbf{C}_1 & \mathbf{C}_2 \end{pmatrix} \begin{pmatrix} \mathbf{U}_0 \\ \mathbf{U}_1 \\ \mathbf{U}_2 \end{pmatrix} - k \begin{pmatrix} \mathbf{I} & 0 & 0 \\ 0 & \mathbf{I} & 0 \\ 0 & 0 & \mathbf{I} \end{pmatrix} \begin{pmatrix} \mathbf{U}_0 \\ \mathbf{U}_1 \\ \mathbf{U}_2 \end{pmatrix} = 0 \tag{3.62}$$

where

$$\mathbf{C}_2 = \mathbf{K}_2 \tag{3.63a}$$

$$\mathbf{C}_1 = \mathbf{K}_1 \tag{3.63b}$$

$$\mathbf{C}_0 = \mathbf{K}_0 - \omega^2\mathbf{M} \tag{3.63c}$$

System (3.62) can be converted to a standard form by eliminating $\mathbf{U}_2$, in order to get:

$$\begin{pmatrix} 0 & \mathbf{I} \\ -\mathbf{C}_2^{-1}\mathbf{C}_0 & -\mathbf{C}_2^{-1}\mathbf{C}_1 \end{pmatrix} \begin{pmatrix} \mathbf{U}_0 \\ \mathbf{U}_1 \end{pmatrix} - k \begin{pmatrix} \mathbf{I} & 0 \\ 0 & \mathbf{I} \end{pmatrix} \begin{pmatrix} \mathbf{U}_0 \\ \mathbf{U}_1 \end{pmatrix} = 0 \tag{3.64}$$

If N is the dimension of the system (3.64), for each frequency ω, $2N$ eigenvalues k along the cross-sectional wave shape of the laminate can be found, with associated $2N$ propagating eigenvectors (N forward and N backward modes). The pure real eigenvalues (Rek) represent *propagating oscillating waves* in the longitudinal x-direction, whereas complex conjugate eigenvalues (Re$k \pm$ Imk) and purely imaginary numbers ($\pm$Imk) represent *oscillating evanescent waves* and *non-oscillating evanescent waves*, respectively. Evanescent waves are waves that exhibit an exponential decay, so they do not propagate to the far field, but simply attenuates with the distance.

3.3.4 Group Velocity Determination

In undamped media, the stiffness matrix $\mathbf{C}_{\mathbf{x-y}}$ is real. The group velocity c_g in conventional manner can be calculated through the differentiations of two close frequencies and two adjacent wave numbers:

$$c_g = \frac{\partial \omega}{\partial k} \cong \frac{(\omega_{i+1} - \omega_i)}{(k_{i+1} - k_i)} \tag{3.65}$$

Due to the complexity of dispersion curves, especially when one mode overlaps another, Eq. (3.65) is not straightforward. Indeed, a small error in the wavenumber causes large errors in the assessment of the group velocity. A new approach proposed by Finnveden (Finnveden [2004]) allowed calculating the group velocity at each frequency and wavenumber solution, without any contribution from closest points. The procedure consisted of evaluating at first the derivative of Eq.

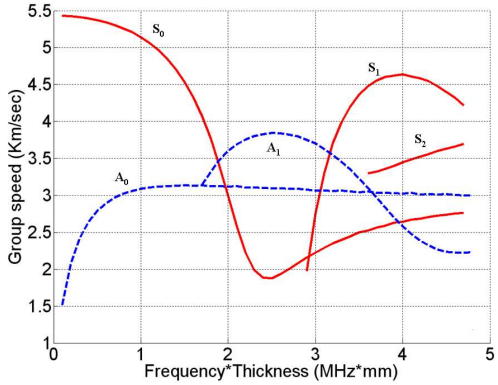

Figure 3.4: Dispersion curves for a quasi-isotropic composite plate with 3mm of thickness

(3.60) with respect to the wavenumber:

$$\begin{aligned}
&\frac{\partial}{\partial k}\left[\mathbf{K}_0(\phi)+\mathbf{K}_1(\phi)+\mathbf{K}_2(\phi)k^2-\omega^2\mathbf{M}\right]\mathbf{U}_R \\
&\quad=\left\{\frac{\partial\left[\mathbf{K}_0(\phi)+\mathbf{K}_1(\phi)+\mathbf{K}_2(\phi)k^2\right]}{\partial k}-2\omega\frac{\partial\omega}{\partial k}\right\}\mathbf{U}_R \\
&\quad+\left[\mathbf{K}_0(\phi)+\mathbf{K}_1(\phi)+\mathbf{K}_2(\phi)k^2-\omega^2\mathbf{M}\right]\frac{\partial\mathbf{U}_R}{\partial k}
\end{aligned} \tag{3.66}$$

where $\mathbf{U}_R$ is the right-eigenvector. Multiplying Eq. (3.66) by the transpose of the left-eigenvector, $\mathbf{U}_L^T=\mathbf{U}^\dagger$, where the superscript † corresponds to the Hermitian conjugation operation, by virtue of following equation:

$$\mathbf{U}^\dagger\left[\mathbf{K}_0(\phi)+\mathbf{K}_1(\phi)+\mathbf{K}_2(\phi)k^2-\omega^2\mathbf{M}\right]=0 \tag{3.67}$$

we get:

$$\mathbf{U}^\dagger\left\{\frac{\partial\left[\mathbf{K}_0(\phi)+\mathbf{K}_1(\phi)+\mathbf{K}_2(\phi)k^2\right]}{\partial k}-2\omega\frac{\partial\omega}{\partial k}\right\}\mathbf{U}_R=0 \tag{3.68}$$

Rearranging Eq. (3.68), since $\partial\omega/\partial k$ is a scalar, the group velocity c_g becomes:

$$c_g=\frac{\partial\omega}{\partial k}=\frac{\mathbf{U}^\dagger\left[\mathbf{K}_1(\phi)+2k\mathbf{K}_2(\phi)\right]\mathbf{U}_R}{2\omega\mathbf{U}^\dagger\mathbf{M}\mathbf{U}_R} \tag{3.69}$$

This equation indicates that the group velocity can be estimated for each wavenumber and frequency at a time, without regard to any adjacent solutions (Fig. 3.4).

Chapter 4

Theory of Time Reversal Imaging Method

If the time invariance and spatial reciprocity of the wave equation are satisfied, a *time reversal* (TR) imaging process can be used to focus ultrasonic waves through homogeneous and inhomogeneous media. Indeed, a wave diverging from a punctual source and received by a set of transducers enclosing the medium, can be time reversed and re-emitted by the sensors elements. The generated wave will converge back to its original source location as if time was running backwards.
This chapter is aimed to report the theoretical description of time reversal imaging method, by first introducing the theoretical treatment of a pulsed elastic wave generated by a point source propagating within an isotropic medium (Sec. 4.1). Then, in order to obtain the optimal re-focusing at the source location, an ideal experimental set-up known as "Time Reversal Cavity" (TRC) is presented (Sec. 4.2). A TRC is composed by a closed surface covered with a 2D array of reversible transducers surrounding the source and is presented through an extensive use of the Green's function theory for homogeneous and inhomogeneous media. The basic and most relevant results of such treatment enables an understanding of the physics of time reversal. However, a TRC is difficult to realize in practise and the time reversal imaging is only achieved with a limited number of transducers of finite amplitude that limits the focus quality, known as time-reversal mirror (TRM) (Sec.4.3). Nevertheless, Sec. 4.4 illustrates that the reverberation of a

diffuse wave field in a complex medium improves the spatial resolution of the focusing.

4.1 The Wave Equation with Dirac Point-Like Source

The *Navier's* equation of motion (3.8) for an isotropic elastic medium with a source distribution $\mathbf{f}(\mathbf{r},t)$ is (Achenbach [1984]):

$$\rho\frac{\partial^2\mathbf{u}(\mathbf{r},t)}{\partial t^2} = (\lambda+\mu)\nabla\left[\nabla\cdot\mathbf{u}(\mathbf{r},t)\right] + \mu\nabla^2\mathbf{u}(\mathbf{r},t) + \mathbf{f}(\mathbf{r},t) \tag{4.1}$$

which can be decoupled in the following system of equations:

$$\begin{aligned} c_l^2\nabla^2\mathbf{u}^l(\mathbf{r},t) - \frac{\partial^2\mathbf{u}^l(\mathbf{r},t)}{\partial t^2} &= -\mathbf{f}(\mathbf{r},t) \\ c_t^2\nabla^2\mathbf{u}^t(\mathbf{r},t) - \frac{\partial^2\mathbf{u}^t(\mathbf{r},t)}{\partial t^2} &= -\mathbf{f}(\mathbf{r},t) \end{aligned} \tag{4.2}$$

Assuming the wave field $\psi(\mathbf{r},t)$ as a generic component of the longitudinal or shear displacement vector field (3.11), we can write:

$$c^2\nabla^2\psi(\mathbf{r},t) - \frac{\partial^2\psi(\mathbf{r},t)}{\partial t^2} = -f(\mathbf{r},t) \tag{4.3}$$

Eq. (4.3) is an inhomogeneous, linear, partial differential equation (PDE) where c is the velocity of propagation in the medium and $f(\mathbf{r},t)$ is a known point-like source in a *homogeneous* medium given by:

$$f(\mathbf{r},t) = e(t)\delta(\mathbf{r}) \tag{4.4}$$

where $\delta(\mathbf{r})$ represents the Dirac delta function in the three-dimensional space and $e(t)$ is the signal emitted by the point-like source, which describes the temporal

variations of the source excitation:

$$e(t) = \begin{cases} 0 & \forall t < 0 \\ e(t) & \forall t \in [0, T_e] \\ 0 & \forall t > T_e \end{cases} \tag{4.5}$$

where T_e is the temporal duration of the excitation function $e(t)$. Eq. (4.5) implies that $e(t)$ is a causal function and the temporal excitation only exists on a finite time-interval. The time-derivative operator of Eq. (4.3) appears only at the second order, hence if $\psi(\mathbf{r}, t)$ is a solution, then $\psi(\mathbf{r}, -t)$ is also a solution. It should also be noticed that the presence of the Laplacian differential operator, guarantees the invariance of Eq. (4.3) under the transformation $\mathbf{r} \rightarrow -\mathbf{r}$, i.e it guarantees a *spatial reciprocity* condition.
According to the Green's theorem (Duffy [2001]), to solve Eq. (4.3) it is useful to define a Green space-time function G that depends on the variables $(\mathbf{r}, t; \mathbf{r}_0, t_0)$. The Green's function allows the calculation of the wave field ψ at a given position and time $(\mathbf{r}, t)$ without explicitly solving the differential Eq. (4.3). From a physical point of view, it corresponds to an impulsive diverging spherical wave satisfying the following conditions (Barton [1989]):

- $G(\mathbf{r}, t; \mathbf{r}_0, t_0)$ must be a solution to the following linear, inhomogeneous wave equation:

$$c^2 \nabla^2 G(\mathbf{r}, t; \mathbf{r}_0, t_0) - \frac{\partial^2 G(\mathbf{r}, t; \mathbf{r}_0, t_0)}{\partial t^2} = -\delta(\mathbf{r} - \mathbf{r}_0)\delta(t - t_0) \tag{4.6}$$

  where $\delta(\mathbf{r} - \mathbf{r}_0)$ and $\delta(t - t_0)$ are Dirac delta functions in space and time, respectively. $G(\mathbf{r}, t; \mathbf{r}_0, t_0)$ is the field produced in $\mathbf{r}$ at time t by an impulsive force located in $\mathbf{r}_0$ and excited at time t_0. For $t < t_0$ causality requires that $G(\mathbf{r}, t; \mathbf{r}_0, t_0) \equiv 0$.

- $G(\mathbf{r}, t; \mathbf{r}_0, t_0)$ is a reciprocal function in the sense of the *reciprocity theorem*:

$$G(\mathbf{r}, t; \mathbf{r}_0, t_0) \equiv G(\mathbf{r}_0, t_0; \mathbf{r}, -t) \equiv G(\mathbf{r}_0, t; \mathbf{r}, t_0) \tag{4.7}$$

- $G(\mathbf{r}, t; \mathbf{r}_0, t_0)$ must satisfy the homogeneous boundary conditions on S (Dirichelet,

Neumann or mixed):

$$G(\mathbf{r}, t; \mathbf{r}_0, t_0) = 0 \quad \mathbf{r} \in S \tag{4.8a}$$

$$\frac{\partial G(\mathbf{r}, t; \mathbf{r}_0, t_0)}{\partial \mathbf{n}} = 0 \quad \mathbf{r} \in S \tag{4.8b}$$

where S is a closed surface of a solid Ω and $\partial G(\mathbf{r}, t; \mathbf{r}_0, t_0)/\partial \mathbf{n}$ is the Green's function normal derivative.

- $G(\mathbf{r}, t; \mathbf{r}_0, t_0)$ must satisfy the Cauchy initial conditions:

$$G(\mathbf{r}, t; \mathbf{r}_0, t_0) = 0 \quad t = t_0 \tag{4.9a}$$

$$\frac{\partial G(\mathbf{r}, t; \mathbf{r}_0, t_0)}{\partial t} = 0 \quad t = t_0 \tag{4.9b}$$

Hence, considering Eq. (4.6) and conditions (4.8a-4.9b), the solution of the wave equation (4.3) can be expressed in terms of the Green's function, boundary conditions and initial condition as follows:

$$c^2 \nabla_0^2 \psi(\mathbf{r}_0, t_0) - \frac{\partial^2 \psi(\mathbf{r}_0, t_0)}{\partial t_0^2} = -f(\mathbf{r}_0, t_0) \tag{4.10a}$$

$$c^2 \nabla_0^2 G(\mathbf{r}, t; \mathbf{r}_0, t_0) - \frac{\partial^2 G(\mathbf{r}, t; \mathbf{r}_0, t_0)}{\partial t_0^2} = -\delta(\mathbf{r} - \mathbf{r}_0)\delta(t - t_0) \tag{4.10b}$$

Multiplying Eq. (4.10a) by $G(\mathbf{r}, t; \mathbf{r}_0, t_0)$ and Eq. (4.10b) by $\psi(\mathbf{r}_0, t_0)$, performing the difference and then integrating over the volume Ω_0 and over the time t_0 from 0 to t', with $t' \gg t$ in order to avoid the integration exactly at the peak of the

delta function, we obtain:

$$\begin{aligned}
&\int_{t_0}^{t'} dt_0 \iiint_{\Omega} \Big\{ c^2 \left[\nabla_0^2 \psi(\mathbf{r}_0, t_0) G(\mathbf{r}, t; \mathbf{r}_0, t_0) - \nabla_0^2 G(\mathbf{r}, t; \mathbf{r}_0, t_0) \psi(\mathbf{r}_0, t_0) \right. \\
&\quad \left. + \frac{\partial^2 G(\mathbf{r}, t; \mathbf{r}_0, t_0)}{\partial t_0^2} \psi(\mathbf{r}_0, t_0) - \frac{\partial^2 \psi(\mathbf{r}_0, t_0)}{\partial t_0^2} G(\mathbf{r}, t; \mathbf{r}_0, t_0) \right] \Big\} d\Omega_0 \\
&\quad = \int_{t_0}^{t'} dt_0 \iiint_{\Omega} \left[\delta(\mathbf{r} - \mathbf{r}_0) \delta(t - t_0) \psi(\mathbf{r}_0, t_0) - f(\mathbf{r}_0, t_0) G(\mathbf{r}, t; \mathbf{r}_0, t_0) \right] d\Omega_0 \\
&\quad = \psi(\mathbf{r}, t) - \int_{t_0}^{t'} dt_0 \iiint_{\Omega} f(\mathbf{r}_0, t_0) G(\mathbf{r}, t; \mathbf{r}_0, t_0) d\Omega_0
\end{aligned} \tag{4.11}$$

The volume integral over the two terms in left side of Eq. (4.11) turns into a surface integral employing Green's second identity as follows:

$$\begin{aligned}
&\iiint_{\Omega} \left[\frac{\partial G(\mathbf{r}, t; \mathbf{r}_0, t_0)}{\partial t_0} \psi(\mathbf{r}_0, t_0) - \frac{\partial \psi(\mathbf{r}_0, t_0)}{\partial t_0} G(\mathbf{r}, t; \mathbf{r}_0, t_0) \right] d\Omega_0 \\
&\quad + \int_{t_0}^{t'} dt_0 \iint_{S} c^2 \left[\nabla_0^2 \psi(\mathbf{r}_0, t_0) G(\mathbf{r}, t; \mathbf{r}_0, t_0) - \nabla_0^2 G(\mathbf{r}, t; \mathbf{r}_0, t_0) \psi(\mathbf{r}_0, t_0) \right] \cdot \mathbf{n} dS_0
\end{aligned} \tag{4.12}$$

where $\mathbf{n}$ is the vector field normal to the closed surface S in each of its points, directed outwards. Hence, Eq. (4.11) can be rewritten as:

$$\psi(\mathbf{r}, t) = g(\mathbf{r}, t) + h(\mathbf{r}, t) + s(\mathbf{r}, t) \tag{4.13}$$

with:

$$g(\mathbf{r},t) = \int_{t_0}^{t'} dt_0 \iiint_{\Omega} f(\mathbf{r}_0,t_0)G(\mathbf{r},t;\mathbf{r}_0,t_0)d\Omega_0 \tag{4.14a}$$

$$h(\mathbf{r},t) = c^2 \int_{t_0}^{t'} dt_0 \iint_{S} \left[\nabla_0^2\psi(\mathbf{r}_0,t_0)G(\mathbf{r},t;\mathbf{r}_0,t_0) - \nabla_0^2 G(\mathbf{r},t;\mathbf{r}_0,t_0)\psi(\mathbf{r}_0,t_0)\right]\cdot\mathbf{n}dS_0 \tag{4.14b}$$

$$s(\mathbf{r},t) = \iiint_{\Omega}\left[\frac{\partial G(\mathbf{r},t;\mathbf{r}_0,t_0)}{\partial t_0}\psi(\mathbf{r}_0,t_0) - \frac{\partial\psi(\mathbf{r}_0,t_0)}{\partial t_0}G(\mathbf{r},t;\mathbf{r}_0,t_0)\right]d\Omega_0 \tag{4.14c}$$

Eq. (4.13) gives the complete solution of the inhomogeneous problem (4.3) including the initial conditions. The above terms $g(\mathbf{r},t)$ and $h(\mathbf{r},t)$ represent the effects of the source and the boundary conditions, respectively. The last term $s(\mathbf{r},t)$ is only related to the initial conditions (Barton [1989]).
Assuming a free unbounded space and supposing that we are able to measure at any point of a closed surface S the wave field $\psi(\mathbf{r},t)$ and its normal derivatives (set to zero at infinity), the general solution of the wave equation (4.3) takes the form:

$$\begin{aligned}\psi(\mathbf{r},t) &= \int_{t_0}^{t'} dt_0 \iiint_{\Omega} f(\mathbf{r}_0,t_0)G(\mathbf{r},t;\mathbf{r}_0,t_0)d\Omega_0 \\ &= \iiint_{\Omega} G(\mathbf{r},\mathbf{r}_0;t)\otimes f(\mathbf{r}_0,t)d\Omega_0\end{aligned} \tag{4.15}$$

where the symbol $\otimes$ represents a convolution over time and the Green's function for an unbounded isotropic medium is given by Eq. (A.9). In the case of anisotropic medium, $G(\mathbf{r},\mathbf{r}_0;t)$ assumes forms more complicated than Eq. (A.9) (Tverdokhlebov & Rose [1988]).
Substituting Eqs. (A.9) and (4.4) in Eq. (4.15), the solution of the wave equation

with a Dirac distribution for an elastic, isotropic, homogeneous solid is:

$$\psi(\mathbf{r},t) = \iiint_{\Omega} \left[\frac{1}{4\pi\|\mathbf{r}-\mathbf{r}_0\|} \delta\left(t - \frac{\|\mathbf{r}-\mathbf{r}_0\|}{c}\right) \otimes e(t)\delta(\mathbf{r}_0) \right] d\Omega_0$$
$$= G_d(\mathbf{r},\mathbf{r}_0;t) \otimes e(t) = \frac{1}{4\pi\|\mathbf{r}-\mathbf{r}_0\|} e\left(t - \frac{\|\mathbf{r}-\mathbf{r}_0\|}{c}\right) \tag{4.16}$$

where $G_d(\mathbf{r},\mathbf{r}_0;t)$ is the forward propagating field from the source located at $\mathbf{r} = \mathbf{r}_0$. However, the same theory here developed can be generalised to the case of elastic, isotropic medium with inhomogeneities. In this case, the point-like source $f(\mathbf{r},t)$ is given by the following expression (Cassereau & Fink [1992]):

$$f(\mathbf{r},t) = e(t)\delta(\mathbf{r}) + L(\mathbf{r})[\psi(\mathbf{r},t)] \tag{4.17}$$

where the term $L(\mathbf{r})$ is the functional linear operator applied on the wave field $\psi(\mathbf{r},t)$. It describes the interactions between the inhomogeneities and the wave field acting as secondary sources, i.e. the "*scatterers*". Substituting the free-space retarded Green's function [Eq. (A.9), see appendix A] and Eq. (4.17) in Eq. (4.15), the solution of the wave equation with a Delta function for an inhomogeneous medium is:

$$\psi(\mathbf{r},t) = \underbrace{\frac{1}{4\pi\|\mathbf{r}-\mathbf{r}_0\|} e\left(t - \frac{\|\mathbf{r}-\mathbf{r}_0\|}{c}\right)}_{\text{primary source}} + \underbrace{\iiint_{\Omega} \left\{ L(\mathbf{r_0})[\psi(\mathbf{r_0},t)] \otimes G_d(\mathbf{r},\mathbf{r}_0;t) \right\} d\Omega_0}_{\text{secondary source}} \tag{4.18}$$

The above equation shows that the wave function is the sum of two components, a *primary source*, i.e. the impulse waveform emitted from the impact point, and a *secondary source* generated by scattering.

4.2 Theory of Time Reversal Cavity

Time Reversal (TR) theoretical description for elastic wave propagation was first introduced by the group of M. Fink at the *Laboratoire Ondes and Acosutique of the Universite de Paris VII Denis Diderot* during 1990s. Based on the principle

of time reversal invariance and spatial reciprocity of wave equation in a lossless medium, in a time reversal experiment, the elastic waves diverging from a point-like target can be focused back to the original source if the output measured by a set of transducers is time reversed and re-emitted back onto the excitation point (Fink [1992]). Although this is not possible in each point of a 3D volume surrounding the source of an elastic impulse, *Huygens's principle* suggests that the reconstruction of the wave function in a generic volume at any time can be obtained by the knowledge of its sources on a 2D surface. From this basic principle of diffraction theory, it derives the *Time Reversal Cavity* (TRC) process (Cassereau *et al.* [1990]). A TR acoustic experiment is usually split into *forward propagation* step and *backward propagation* step. In the *forward propagation* step, the wave field $\psi(\mathbf{r}, t)$ and its normal derivatives are measured at each point $\mathbf{r}$ of the surface S of the cavity within a finite time interval $[0, T]$. The output signal of the ultrasonic receivers (ideally an infinite set) can be written as $\psi(\mathbf{r}, t)W(t)$, where $W(t)$ is a windowing function defined by:

$$W(t) = \begin{cases} 1 & 0 \leq 1 \leq T \\ 0 & \text{otherwise} \end{cases} \tag{4.19}$$

and $\psi(\mathbf{r}, t)$ is the wave field defined either by Eq. (4.16) or (4.18) for a homogeneous or an inhomogeneous medium, respectively (Fig. 4.1).

In the *backward propagation* step, the TR experiment can be obtained by time reversing the received signals during the first step, i.e. throughout the transformation $t \Rightarrow T - t$. From a mathematical point of view, this means that we are able to create secondary sources on the surface of the cavity, such that the boundary conditions on S are the time-reversed components of the wave field $\psi(\mathbf{r}, t)$ received during the forward propagation step (Fig. 4.1). These secondary sources are:

$$\begin{aligned} s_1(\mathbf{r}_0, t) &= \psi(\mathbf{r}_0, T - t)W(T - t) \\ s_2(\mathbf{r}_0, t) &= \frac{\partial \psi(\mathbf{r}_0, T - t)}{\partial \mathbf{n}} W(T - t) \end{aligned} \tag{4.20}$$

According to Eq. (4.20), the initial source at $\mathbf{r}_0$ is now removed or remains passive,

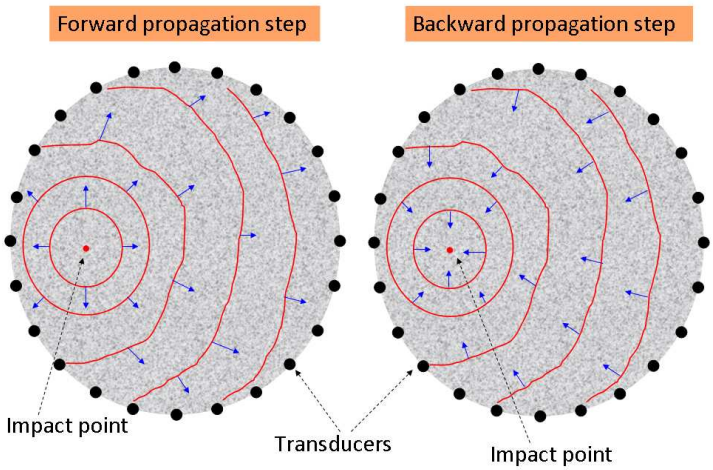

Figure 4.1: Illustration of forward and backward propagation steps in a TRC

whilst the inhomogeneities are unchanged. Hence, the time-reversed wave field $\psi_{TR}(\mathbf{r}, t)$ will satisfy the following equation:

$$c^2\nabla^2\psi_{TR}(\mathbf{r}, t) - \frac{\partial^2\psi_{TR}(\mathbf{r}, t)}{\partial t^2} = -L(\mathbf{r})[\psi_{TR}(\mathbf{r}, t)] \tag{4.21}$$

Similarly to Eq. (4.13), the solution of the above equation can be written as:

$$a(\mathbf{r}, t) = \iiint_{\Omega} \{G_d(\mathbf{r}, \mathbf{r}_0; t) \otimes L(\mathbf{r}_0)[\psi_{TR}(\mathbf{r}_0, t)]\}\, d\Omega_0 \tag{4.22a}$$

$$b(\mathbf{r}, t) = c^2 \iint_{S} [G_d(\mathbf{r}, \mathbf{r}_0; t) \otimes s_2(\mathbf{r}_0, t) - s_1(\mathbf{r}_0, t) \otimes \mathbf{n} \cdot \nabla_0 G_d(\mathbf{r}, \mathbf{r}_0; t)]\, dS_0 \tag{4.22b}$$

wherein the surface integral $b(\mathbf{r}, t)$ can be transformed into a volume integral using the second Green's identity (Duffy [2001]):

$$b(\mathbf{r}, t) = c^2 \iiint_{\Omega} \left[G_d(\mathbf{r}, \mathbf{r}_0; t) \otimes \nabla_0^2 s_2(\mathbf{r}_0, t) - s_1(\mathbf{r}_0, t) \otimes \nabla_0^2 G_d(\mathbf{r}, \mathbf{r}_0; t)\right] d\Omega_0 \tag{4.23}$$

The above equation cannot be used directly for finding a solution of Eq. (4.21), as $s_1(\mathbf{r}_0, t)$, due to time windowing function $W(t)$ defined in Eq. (4.19), has a

singularity in $t = T$. Hence, from the distribution theory reported by (Cassereau *et al.* [1990]) the time-reversed wave field $\psi_{TR}(\mathbf{r}, t)$ can be written as (Cassereau & Fink [1992]):

$$\begin{aligned}\psi_{TR}(\mathbf{r},t) = &\frac{1}{4\pi\|\mathbf{r}-\mathbf{r}_0\|} e\left(T-t-\frac{\|\mathbf{r}-\mathbf{r}_0\|}{c}\right) W(T-t) \\ &- \frac{1}{4\pi\|\mathbf{r}-\mathbf{r}_0\|} e\left(T-t+\frac{\|\mathbf{r}-\mathbf{r}_0\|}{c}\right) W\left(T-t+\frac{\|\mathbf{r}-\mathbf{r}_0\|}{c}\right) \\ &+ W(T-t) \iiint_{\Omega} \{G_c(\mathbf{r},\mathbf{r}_0;t) \otimes L(\mathbf{r}_0)[\psi_{TR}(\mathbf{r}_0,T-t)]\}\, d\Omega_0 \\ &- \iiint_{\Omega} \{G_d(\mathbf{r},\mathbf{r}_0;t) \otimes W(T-t)L(\mathbf{r}_0)[\psi_{TR}(\mathbf{r}_0,T-t)]\}\, d\Omega_0 \\ &+ \iiint_{\Omega} \{G_d(\mathbf{r},\mathbf{r}_0;t) \otimes L(\mathbf{r}_0)[\psi_{TR}(\mathbf{r}_0,t)]\}\, d\Omega_0 \\ &+ \frac{1}{c^2} \iiint_{\Omega} \frac{1}{4\pi\|\mathbf{r}-\mathbf{r}_0\|} \left\{\eta(\mathbf{r}_0)\delta\left(t-\frac{\|\mathbf{r}-\mathbf{r}_0\|}{c}\right) - \zeta(\mathbf{r}_0)\frac{\partial\delta}{\partial t}\left(t-\frac{\|\mathbf{r}-\mathbf{r}_0\|}{c}\right)\right\} d\Omega_0\end{aligned} \tag{4.24}$$

where

$$\begin{aligned}\eta(\mathbf{r}_0) &= \psi(\mathbf{r}_0,t)|_{t=T} \\ \zeta(\mathbf{r}_0) &= \frac{\partial\psi(\mathbf{r}_0,t)}{\partial t}|_{t=T}\end{aligned} \tag{4.25}$$

4.2.1 Focusing in a Homogeneous Medium

If the linear operator $L(\mathbf{r}_0)$ is zero (the medium is without inhomogeneities), the time-reversed wave field $\psi_{TR}(\mathbf{r}_0, t)$ given by Eq. (4.24) is reduced to:

$$\psi_{TR}(\mathbf{r},t) = \frac{1}{4\pi\|\mathbf{r}-\mathbf{r}_0\|}\left[e\left(T-t-\frac{\|\mathbf{r}-\mathbf{r}_0\|}{c}\right) - e\left(T-t+\frac{\|\mathbf{r}-\mathbf{r}_0\|}{c}\right)\right] \tag{4.26}$$

Eq. (4.26) represents the back-propagation wave field which can be described as a superposition of two waveforms: an impulse spherical wave converging to the source position, placed at $\mathbf{r} = \mathbf{r}_0$ (origin of the reference frame), and a spherical

isotropic wave diverging from the impact point. Eq. (4.26) can be re-written in a compact form as:

$$\begin{aligned}\psi_{TR}(\mathbf{r},t) &= G_d(\mathbf{r},\mathbf{r}_0;T-t)\otimes e(t) - G_d(\mathbf{r},\mathbf{r}_0;t)\otimes e(T-t)\\ &= K(\mathbf{r},t)\otimes e(T-t)\end{aligned} \tag{4.27}$$

where the kernel $K(\mathbf{r},t)$ is:

$$K(\mathbf{r},t) = \frac{1}{4\pi\|\mathbf{r}-\mathbf{r}_0\|}\delta\left(t+\frac{\|\mathbf{r}-\mathbf{r}_0\|}{c}\right) - \frac{1}{4\pi\|\mathbf{r}-\mathbf{r}_0\|}\delta\left(t-\frac{\|\mathbf{r}-\mathbf{r}_0\|}{c}\right) \tag{4.28}$$

Hence, comparing Eq. (4.27) and (4.16), two components can be clearly distinguished, an exact time-reversed version of the forward propagating wave field and a diverging component from the position of the source. Eq. (4.27) in the Fourier domain is:

$$\hat{\psi}_{TR}(\mathbf{r},\omega) = \hat{K}(\mathbf{r},\omega)\hat{e}(\omega)e^{i\omega T} \tag{4.29}$$

with:

$$\hat{K}(\mathbf{r},\omega) = \frac{1}{\lambda i}\frac{\sin(k\|\mathbf{r}-\mathbf{r}_0\|)}{k\|\mathbf{r}-\mathbf{r}_0\|} = \frac{1}{\lambda i}\frac{\sin(2\pi\|\mathbf{r}-\mathbf{r}_0\|/\lambda)}{2\pi\|\mathbf{r}-\mathbf{r}_0\|/\lambda} \tag{4.30}$$

where k is the wavenumber defined by and $k = \omega/c = 2\pi/\lambda$ and λ is the wavelength. Hence, according to classical diffraction theory (Auld [1973]), Eq. (4.30) shows that the maximum resolution available through a time reversal focusing process of the wave field in a closed cavity is $\|\mathbf{r}-\mathbf{r}_0\| = \lambda/2$.

4.2.2 Focusing in a Inhomogeneous Medium

If the operator $L(\mathbf{r})$ is not zero, inhomogeneities of the medium must be taken into account. This term includes (Cassereau & Fink [1992]) spatial variations of the compressibility $[\chi = \chi(\mathbf{r})]$ and density $[\rho = \rho(\mathbf{r})]$, located inside a region R contained into the volume Ω. Hence, the operator $L(\mathbf{r})$ can be defined as:

$$L(\mathbf{r}) = \frac{1}{c^2}\gamma_\chi(\mathbf{r})\frac{\partial^2}{\partial t^2} + \nabla\cdot[\gamma_\rho(\mathbf{r})\nabla] \tag{4.31}$$

where $\gamma_\chi(\mathbf{r})$ and $\gamma_\rho(\mathbf{r})$ are the relative variations of compressibility and density with respect to the values corresponding to the homogeneous medium. Substituting Eq. (4.31) in Eq. (4.24), the time-reversed wave field $\psi_{TR}(\mathbf{r}, t)$ is:

$$\psi_{TR}(\mathbf{r}, t) = [g(\mathbf{r}, -t) - g(\mathbf{r}, t)] \otimes e(T - t) \tag{4.32}$$

where where $g(\mathbf{r}, t)$ corresponds to the new Green's impulse solution that allows the calculation of the wave field $\psi_{TR}(\mathbf{r}, t)$ in case of the general source distribution $f(\mathbf{r}, t)$ given by (4.17). Similarly to Eq. (4.27), Eq. (4.32) represents the wave function propagating during the second step, expressed as a superposition of a converging spherical wave towards the impact source and a diverging isotropic wave from the source itself. In particular, in the *forward propagation* step, due to causality reasons, the waveforms from the impact point arrive at the TR cavity only after scattering from the inhomogeneities of the medium. Hence, as $g(\mathbf{r}, -t)$ is the the time reversed version of the Green's function $g(\mathbf{r}, t)$, according to Eq. (4.32), in the *backward propagation* step the effects of local heterogeneities (spatial variations of the compressibility modulus and density) are observed first. Moreover, the impulsive responses $[g(\mathbf{r}, -t) - g(\mathbf{r}, t)]$ are completely separated in time (except in the neighbourhood of the source $\mathbf{r}_0$) and the second term takes place only after the first term vanish.

4.3 Theory of Time Reversal Mirror

As remarked in the previous Section, the basic principles of Time Reversal Cavity are interesting since they allow an understanding of the time-reversed focusing process. However, according to (Fink [1992]), TRC is a pure theoretical model and the following considerations must be addressed:

- the results in TRC theory do not depend on the shape of the surface S to obtain the imaging of an impact point source
- compensation of the focusing beam for inhomogeneous materials is self-adaptive (there is a no *a priori* knowledge of scattering location)

- the time-reversed field of the cavity has a *spherical symmetry* with a maximum resolution of $\lambda/2$
- TRC cannot be obtained in practise, since the ultrasonic receivers do not measure simultaneously the wave field $\psi(\mathbf{r}, t)$ in each point and its normal derivatives. In general, the electrical output contains a linear combination of both quantities
- it is not experimentally possible to surround the 2D surface with ultrasonic transducers. Indeed, only a limited solid angle can be covered in respect to the whole cavity
- any transducer device shows a finite aperture, so that information loss about the wave field is inevitable (spatial filtering)

Therefore, a TRC is replaced by a *Time Reversal Mirror* (TRM) of finite bandwidth and aperture that limits the focusing quality (Wu *et al.* [1992]). From a theoretical point of view, the TRM basic principle is very similar to TRC and can be divided in the *forward propagation* step and *backward propagation* step. In terms of signal processing, the acoustic emission (AE) propagation [Eq. (4.15)] can be described as a linear system with different impulse responses (Papoulis [1984]). Indeed, if $e(t) = \delta(t)$ represents an input source sending an ideal pulse, the electrical output $f(t)$ at the transducer location is:

$$f(t) = h(t) \otimes e(t) \approx h(t) \tag{4.33}$$

where $h(t) = G_d(\mathbf{r}, \mathbf{r}_0; t)$ is the impulsive response (Green's function) describing the propagation from the source to the receiver (included the transducer electromechanical efficiency). Subsequently, the output signal [Eq. 4.33] is time reversed and the new electrical input is:

$$f_{TR}(t) = h(-t) \tag{4.34}$$

In the *backward propagation* step, the time-reversed signal [Eq. 4.34] is re-transmitted through the medium and the time-reversed field at the source location becomes:

$$e_{TR}(t) = h(-t) \otimes h(t) \tag{4.35}$$

It must be noted that, due to spatial reciprocity condition, $h(t)$ propagates also from the receiver to the source. In the frequency domain, TRM can be seen as an extension of optical *Phase Conjugated Mirror* (PCM), as the Fourier transform of the time-reversed signal $h(-t)$ is $\hat{h}^*(\omega)$. Hence, the TR version of an impulsive waveform is mathematically equivalent to the phase conjugation of monochromatic waves (Jackson & Dowling [1991]).

From an experimental point of view, TRM consists of one or two-dimensional array of piezoelectric transducers that can work as either pulse-echo or receiving-transmitting modes and fulfils the following conditions:

- the spatial sampling of the TRM can introduce grating lobes, which can be avoided by using an array pitch smaller than $\lambda_{min}/2$, where λ_{min} is the smallest wavelength of the waveforms
- the temporal sampling of the signal acquired in the forward propagating step must be of the order of $T_{min}/8$, where T_{min} is the minimum period of the waveforms

The receiver sensors are connected to a receiving amplifier, A/D converter and a personal computer for recording and time reversing the waveforms. The back-scattered signals sent out by the actuators can be the wave fields emitted either by the impact point or simply a scatterer (or more scatterers) illuminated in the forward propagation step. The transmitter transducer can be driven by waveform generator and instrumented with a D/A converter and amplifiers.

4.4 Time Reversal Elastic Wave Propagation in Diffusive Wave Fields

A number of experiments were conducted since the 1990s to investigate the properties of TRM in homogenous and inhomogeneous media (Fink [1997]). In par-

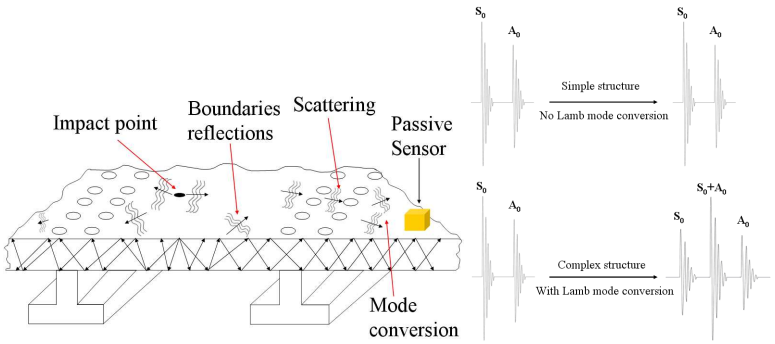

(a) (b)

Figure 4.2: Complex structure with diffused wave field conditions (a) and the effects of mode conversion for the fundamental Lamb waves in complex structures (b)

ticular, experiments in lossless acoustic waveguides (Roux *et al.* [1997]) showed that TR approach behaves as a *matched-filter*, which maximises the ratio between the amplitude of the output and the energy of the input (Dorme & Fink [1995]). Indeed, it is straightforward from Eq. (4.35) that:

$$e_{TR}(t) = h(-t) \otimes h(t) = \int_{-\infty}^{+\infty} h(\tau)h(t+\tau)d\tau \tag{4.36}$$

where the left term of Eq. (4.36) represents a TR operation and the right term is the auto-correlation function of the Green's function. The above equation is maximum at the TR focusing time $t = 0$ and equal to $\int_{-\infty}^{+\infty} h^2(t)dt$, i.e. the energy of the inpulsive function $h(t)$.

The theory of elastic propagation in ultrasonic waveguides can be extended to real aerospace structures, wherein the dispersive nature of guided Lamb waves and the presence in geometrically complex media of multiple scattering, reflections from the boundaries and mode conversion (known from seismology as *coda*) can lead to waveforms recorded by the sensors dissimilar from the original elastic source. That is, the wave field of complex structures (with stiffeners, rivets, holes and voids), excited over a finite frequency band, becomes diffuse incoherent (Fig. 4.2).

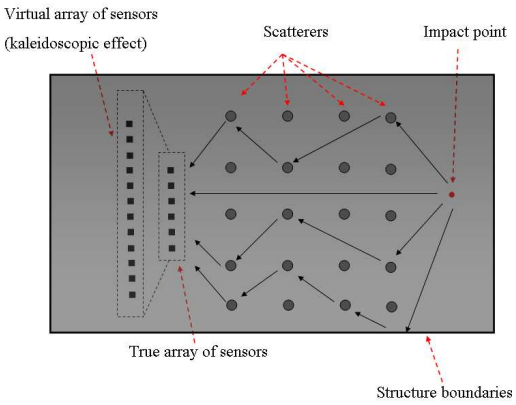

Figure 4.3: Illustration of Kaleidoscopic effect

From a statistical point of view, fully *diffuse wave fields* are globally equipartitioned and are characterized by a superposition of modes having uncorrelated amplitude, phase and direction of propagation (Weaver [1982], Evans & Cawley [1999]). However, Lobkins and Weaver (Lobkis & Weaver [2001]) showed the importance of the elastic diffuse wave field to retrieve the structural impulse response (Green's function) at two sensors locations. This concept was then widely used in seismology (Campillo & Paul [2003]), ocean acoustics (Roux & Fink [2003]), open media (Derode *et al.* [2003b]) and ultrasonic applications (Derode *et al.* [2003a]), and only recently it was examined through a time reversal (TR) process (Wapenaar *et al.* [2005]). Since TRM behaves as a matched-filter in lossless structures, Derode et al. (Derode *et al.* [1995]) illustrated that the reverberations of a diffuse wave field in a complex medium enhance the focusing resolution of the re-emitted signal, and, in particular cases, allow overcoming the diffraction limit (De Rosny & Fink [2002]). Such a combination of TR and diffusive wave fields is known as *Correlation of a Diffuse Field* (CDF). From a physical point of view, this phenomenon is due to the presence of scatterers within the medium that allows the *evanescent modes* (waves that decay exponentially with the distance to the source) to be converted in propagating modes (Carminati *et al.* [2000], Blomgren *et al.* [2002]). These waves, carrying the information of the impact source to the far field, where the TRM is located, can participate to the focusing process. The result of such operation creates a "virtual" enlargement of the transducers an-

gular aperture (*kaleidoscopic effect*) of the TRM and thus the number of sensors can be drastically reduced (Fig. 4.3). The limit case was reported by Draeger and Fink (Draeger & Fink [1997]) wherein the benefits of a reverberant closed cavity, showing ergodic properties and negligible absorptions, were used to perform TRM experiments with only one sensor surface bonded.

Chapter 5

Impact Localization Algorithms in Plate-Like Structures

This chapter investigates the development of two *algorithm-based* SHM systems able to identify in real-time the acoustic emission source (impact point) in isotropic and composite plate-like structures. The proposed techniques rely on the differences of stress waves measured by a number of surface bonded piezoelectric transducers. In both methodologies a joint time frequency analysis based on the magnitude of the *Continuous Wavelet Transform* (CWT) was used to determine the time of arrivals (TOA) of the wave packets. Then, a combination of a globally convergent strategy based on an *unconstrained optimization* (*line search* and *polynomial backtracking*) associated to a local *Newton's* iterative method was employed to solve a set of nonlinear equations in order to assess the impact location coordinates and the flexural group speed. Therefore, these two algorithms overcome the limitations of most impact detection systems, as they do not require *a-priori* knowledge of the group velocity as well as the mechanical properties, thickness and orientation of each ply in the composite laminate (see Sec. 2.3). In addition, the CWT was chosen to guarantee high accuracy in the time-frequency analysis of the acoustic waveforms as it is able to characterize near Lamb modes. To validate the first algorithm for isotropic materials, two different experiments with PVDF and acoustic emission sensors were carried out. The experimental results revealed that the impact source coordinates and the wave velocity values,

compared with those from the dispersion relation [Eq. (3.34)], were predicted with reasonable accuracy.
For the validation of the second algorithm for the composite laminate, experimental tests were conducted on two different structures, a quasi-isotropic carbon fibre reinforced plastic (CFRP) and a sandwich panel. The results showed that the impact source location and the group speed was achieved with satisfactory accuracy, requiring little computational time (less than 1 s). In addition good agreement between the group velocity calculated from the algorithm and the values obtained from the dispersion curves through a numerical SFEM analysis [Eq. (3.69)] was found.
This chapter is organized as follow: in Sec. 5.1 and 5.2 the algorithms for the impact source localization and the fundamental flexural Lamb wave speed determination in aluminium and composite structures are presented. Sec. 5.3 describes the procedure for identifying the time of arrival using the Continuous Wavelet Transform. In Sec. 5.4, the optimization algorithm for obtaining the coordinates of the impact point is discussed. Sec. 5.5 reports the experimental set-up for the specimens tested, whilst in Sec. 5.6 the impact source location results for two aluminium plates, a CFRP and a sandwich panel are shown. Sec. 5.7 reports the values of the flexural group speeds obtained through the comparison with the optimization algorithms and the analytical approach using the Rayleigh-Lamb frequency relations for isotropic media, and the SFEM method for anisotropic materials. Then, a summary with the advantages and disadvantages of the algorithms presented in this chapter is discussed.

5.1 Impact Localization Algorithm for Isotropic Materials

The algorithm for the impact source location and wave velocity determination is based on the differences of acoustic emission (AE) signals measured by **four** piezoelectric transducers attached on the surface of an aluminium structure (Fig. 5.1). As the medium of interest is isotropic and homogeneous, the group velocity can be considered independent of propagation direction. Assuming the origin of

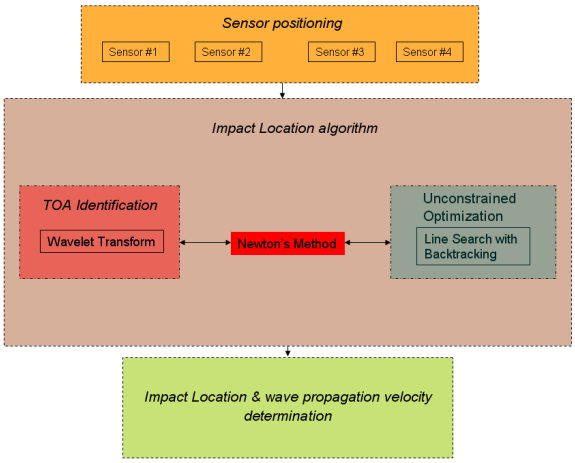

Figure 5.1: Architecture of impacts source location and wave velocity identification system for isotropic structures

the Cartesian planar reference frame $x-y$ was arranged at the left bottom corner of the plate, the impact point I is at unknown coordinates (x_I, y_I) and the sensors are located at distance l_i $(i = 1, \ldots, 4)$ from the source (Fig. 5.2). Furthermore, the dimensions of the plate are L, length and W, width.

The resulting system of equation for the source location problem and wave speed identification is given as follow:

$$\|\mathbf{l}_i\|^2 = (x_i - x_I)^2 + (y_i - y_I)^2 \tag{5.1a}$$

$$t_i = \frac{\|\mathbf{l}_i\|}{c_g} \tag{5.1b}$$

where c_g is the velocity of propagation of the stressed wave, t_i is the time of detection of the AE signals and (x_i, y_i) are the coordinates of the ith sensor. Combining Eqs. (5.1a) and (5.1b) we obtain:

$$(x_i - x_I)^2 + (y_i - y_I)^2 - (t_i c_g)^2 = 0 \tag{5.2}$$

which is the equation of a circumference with radius $r^2 = (t_i c_g)^2$. Eq. (5.2) can

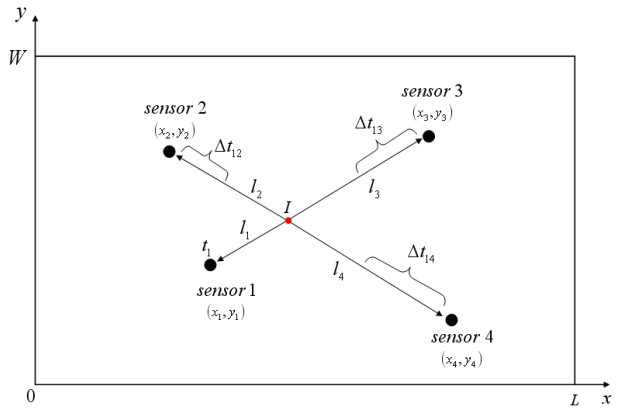

Figure 5.2: Sensors arrangement for the source location in the isotropic plate

be expanded into the following set of equations, with unknowns t_i, x_I, y_I and c_g:

$$\begin{aligned}
(x_1 - x_I)^2 + (y_1 - y_I)^2 - (t_1 c_g)^2 &= 0 \\
(x_2 - x_I)^2 + (y_2 - y_I)^2 - (t_2 c_g)^2 &= 0 \\
(x_3 - x_I)^2 + (y_3 - y_I)^2 - (t_3 c_g)^2 &= 0 \\
(x_4 - x_I)^2 + (y_4 - y_I)^2 - (t_4 c_g)^2 &= 0
\end{aligned} \tag{5.3}$$

This is a system of four equations with seven unknowns. However, if t_1 is the travel time required to reach the sensor 1 (*master sensor*) and Δt_{1j} $(j = 2, 3, 4)$ are the time difference between the sensor 1 and the other sensors, we can write:

$$t_j = t_1 \pm \Delta t_{1j} \tag{5.4}$$

and system (5.2) becomes:

$$(x_i - x_I)^2 + (y_i - y_I)^2 - [(t_1 \pm \Delta t_{1j}) \cdot c_g]^2 = 0 \tag{5.5}$$

Location and wave velocity must be calculated by solving this set of non linear equations with the unknown $\mathbf{x} = x_I, y_I, t_i, c_g$. However, an appropriate time-frequency analysis for the determination of the time differences Δt_{1j} as well as a well-adapted resolution algorithm need to be chosen.

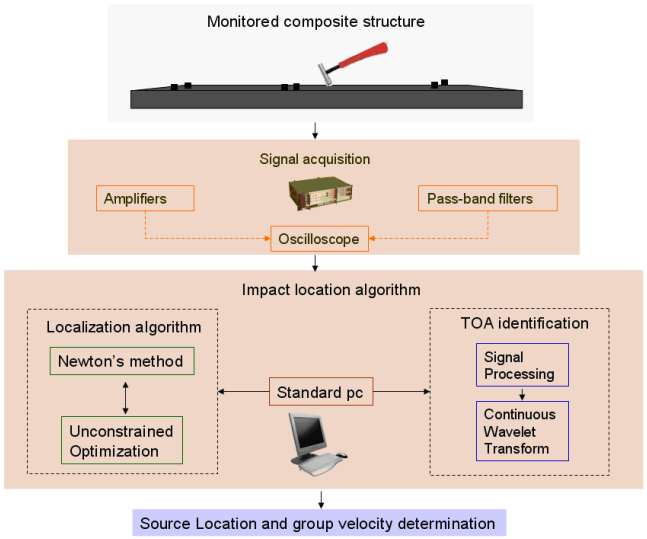

Figure 5.3: Architecture of source location system in anisotropic materials

5.2 Impact Localization Algorithm for Anisotropic Materials

In order to overcome the limitations of triangulation techniques as the group speed is not constant but dependent of the excitation frequency (f) and the heading angle (θ) in the $x-y$ plane, the algorithm for isotropic materials reported in Sec. 5.1 is extended to anisotropic structures. Such method is based on the differences of the wave packets measured by **six** surface bonded AE piezoelectric sensors and, unlike other SHM systems (see Sec. 2.3.2), it can be applied to composite laminates with any lay-up, thickness and anisotropic angular-group velocity pattern (Fig. 5.3).

In accordance with the previous algorithm, let us consider as origin of the planar Cartesian reference frame the left bottom corner of the structure with dimensions $L \times W$. The impact source point I is at unknown coordinates (x_I, y_I) in the plane of the plate, the transducers are located at distance l_i $(i = 1, \ldots, 6)$ from the source, and d_{km} $(k = 1, 3, 5)$ $(m = 2, 4, 6)$ is the distance between each pair of transducers k and m (Fig. 5.4).

Applying the same procedure employed in Sec. 5.1, the coordinates of the acoustic emission source and the group speed can be evaluated by solving the

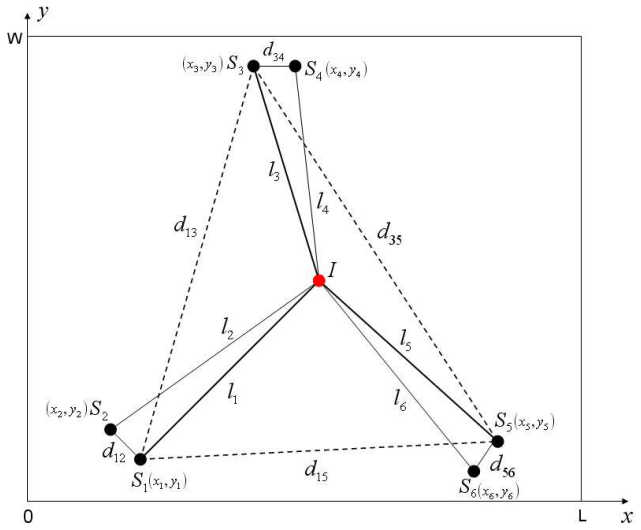

Figure 5.4: Sensors arrangement for the source location in the composite plate

following system of equations:

$$(x_i - x_I)^2 + (y_i - y_I)^2 - [(t_1 \pm \Delta t_{1j}) \cdot c_{g,i}]^2 = 0 \tag{5.6}$$

where $c_{g,i}$ is the velocity of propagation of the stress wave reaching the ith transducer and the index $j = 2, \ldots, 6$. The above set of nonlinear equations is a system of six equations for fourteen unknowns (t_i, x_I, y_I and $c_{g,i}$) and cannot be solved. Thereby, in order to find a solution of system (5.6), additional information is needed, i.e. an optimal sensors configuration. In the current approach, the sensors were disposed in way that each pair of transducers was relatively close together (see Fig. 5.4). In this manner, any pair will experience approximately the same group speed. Therefore, based on the sensors configuration as depicted in Fig. 5.5, if $l_1, l_2 \gg d_{12}$, we have:

$$\frac{d_{12}}{l_1} \ll \sin\left(\underbrace{\theta_1 - \theta_2}_{\Delta\theta}\right) \ll 1 \tag{5.7}$$

where d_{12} is the distance between sensors 1-2, l_1 and l_2 are the distances from the impact source and θ_1 and θ_2 are the heading angles (propagation angles) of the AE in the reference frame. Hence, if $\Delta\theta = \theta_1 - \theta_2$ is sufficiently small (close

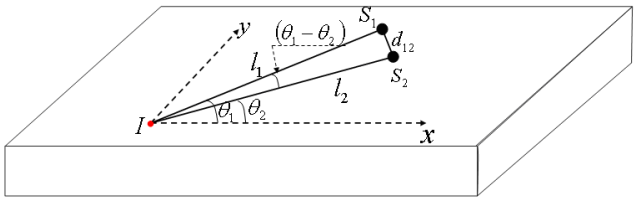

Figure 5.5: Optimal disposition with short distance of each pair of transducers

transducers) such that $\theta_1 \approx \theta_2$, the following assumption becomes straightforward:

$$\begin{aligned} c_{g,1}(\theta) &\approx c_{g,2}(\theta) \\ c_{g,3}(\theta) &\approx c_{g,4}(\theta) \\ c_{g,5}(\theta) &\approx c_{g,6}(\theta) \end{aligned} \tag{5.8}$$

Hence, according to condition (5.8), system (5.6) can now be rewritten as:

$$(x_i - x_I)^2 + (y_i - y_I)^2 - [(t_1 \pm \Delta t_{1j}) \cdot c_{g,k}]^2 = 0 \quad k = 1, 3, 5 \tag{5.9}$$

Source location and group velocity of the flexural Lamb mode can now be calculated by solving the above set of six nonlinear equations with the six unknowns $\mathbf{x} = x_I, y_I, t_i, c_{g,1}, c_{g,3}, c_{g,5}$. Therefore, since no mechanical properties and simple angular-group speed pattern are required, the proposed technique is able to obtain the source location in anisotropic structures for arbitrary lay-up or thickness of the plate.

5.3 The Continuous Wavelet Transform

The dispersive nature of the flexural Lamb mode and the uncertainty of the noise level can drastically decrease the performance of a source localization system. Hence, a good impact detection method necessitates of a suitable choice of the time-frequency analysis for the time arrival identification (TOA). A wavelet transformation method was chosen as it overcomes the drawback of harmonic analysis of the STFT (see App. B). Indeed, it provides a good compromise between time

and frequency resolution, and it is able to analyse low and high frequencies at the same time, even respecting the uncertainty principle (Le & Argoul [2004] and Newland [1997]).

A wavelet transform is an inner product of the signal $u(t)$ and a family of wavelet. Let $\psi \in L^1(\mathbb{R}) \cap L^2(\mathbb{R})$ be the analysing wavelet called also the *mother wavelet*, where $\mathbb{R}$ is the domain of real numbers and the space $L^2(\mathbb{R})$ is the set of all square-integrable functions defined on $\mathbb{R}$. The condition $\psi \in L^1(\mathbb{R})$ means that the function ψ has a zero integral, i.e.:

$$\int_{-\infty}^{+\infty} \psi(t)dt = 0 \tag{5.10}$$

The condition $\psi \in L^2(\mathbb{R})$ implies that most of the energy in the basis function is confined to a finite duration. There are an infinite number of possible choices for the mother wavelet. Some of them are especially suitable for detecting and characterizing irregularities within the signal. For this purpose, we require $\psi(t)$ to be orthogonal to polynomials up to order N such that the wavelet admits $n+1$ zero moments:

$$\int_{-\infty}^{+\infty} t^p \psi(t)dt = 0 \qquad 0 \leq p \leq N \tag{5.11}$$

The number p controls the oscillations of ψ, in the sense that the larger p is, the more ψ oscillates. Furthermore, the mother wavelet must satisfy the *admissibility condition* defined as:

$$\int_{-\infty}^{+\infty} \frac{|\hat{\psi}(\omega)|^2}{|\omega|} d\omega < \infty \tag{5.12}$$

where $\hat{\psi}$ is the Fourier transform of ψ. Eq. (5.12) is the necessary condition for ensuring the existence of the inverse wavelet transform.

The Continuous Wavelet Transform (CWT) is a linear transformation that decomposes an arbitrary signal $u(t)$ through basis functions that are simply dilatations and translations of a parent wavelet $\psi(t)$, by the continuous convolution of

the signal and the scaled or shifted wavelet (Mallat [1998]):

$$CWT(a,b) = \langle u(t)|\psi_{a,b}\rangle = \frac{1}{\sqrt{a}} \int_{-\infty}^{+\infty} u(t)\psi^* \left(\frac{t-b}{a}\right) dt \tag{5.13}$$

where $\psi^*(t)$ denotes the complex conjugate of the mother wavelet $\psi(t)$, a is the dilatation or scale parameter defining the support width of the wavelet and b the translation parameter localising the wavelet in the time domain. The factor $1/\sqrt{a}$ is used to ensure that all wavelets at all scales have the same area and contain the same energy. The notation $\langle u(t)|\psi_{a,b}\rangle$ is used for inner product or the projection of function $u(t)$ onto the wavelet function $\psi(t)$. Analogously to the Fourier transform, the CWT is a linear integral transformation and according with the Parseval's theorem it conserves the energy (Yang *et al.* [2004]). If $\hat{u}(\omega)$ is the Fourier transform of the signal $u(t)$ and $a\hat{\psi}^*(a\omega)e^{i\omega b}$ the Fourier transform of the wavelet $\psi^*(t-b/a)$, we obtain in the angular frequency domain:

$$CWT(a,b) = \frac{\sqrt{a}}{2\pi} \int_{-\infty}^{+\infty} \hat{u}(\omega)\hat{\psi}^*(a\omega)e^{i\omega b} d\omega \tag{5.14}$$

According to appendix B, assuming the duration Δt_ψ and the bandwidth $\Delta\omega_\psi$ as a function of the scale parameter a, we obtain:

$$\Delta t = a^m \Delta t_\psi \tag{5.15a}$$

$$\Delta\omega = \frac{\Delta\omega_\psi}{a^m} \tag{5.15b}$$

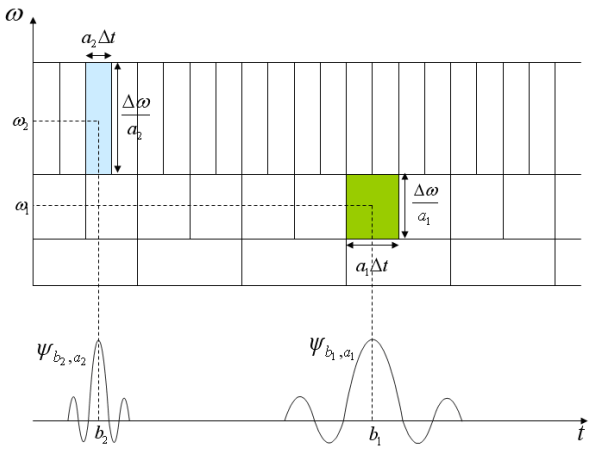

Figure 5.6: Tiling of Heisenberg box for CWT

where $m \in \mathbb{Z}$ and $\mathbb{Z}$ is the set of positive integers. Δt_ψ and $\Delta\omega_\psi$ can also be expressed in terms of standard deviation of root mean square (RMS) as follows:

$$\Delta t_\psi = \frac{1}{|\psi(t)|^2}\sqrt{\int_{-\infty}^{+\infty}(t-t_\psi)^2|\psi(t)|^2dt} \tag{5.16a}$$

$$\Delta\omega_\psi = \frac{1}{|\hat{\psi}(\omega)|^2}\sqrt{\int_{-\infty}^{+\infty}(\omega-\omega_\psi)^2|\hat{\psi}(\omega)|^2d\omega} \tag{5.16b}$$

where $t_\psi = \int_{-\infty}^{+\infty} t|\psi(t)|^2dt / \int_{-\infty}^{+\infty}|\psi(t)|^2dt$ and $\omega_\psi = \int_{-\infty}^{+\infty}\omega|\hat{\psi}(\omega)|^2d\omega / \int_{-\infty}^{+\infty}|\hat{\psi}(\omega)|^2d\omega$ are the temporal centre and the central frequency of $\psi(t)$ and $\hat{\psi}(\omega)$, respectively. Consequently, time resolution of the CWT increases as frequency decreases and frequency resolution increases as time decreases. For these reasons, unlike the Short Time Fourier Transform wherein resolution is constant, the CWT is called *multi-resolution analysis* (Fig. 5.6).

The kernel function of the Continuous Wavelet Transform is:

$$\psi_{a,b}(t) = \frac{1}{\sqrt{a}}\psi\left(\frac{t-b}{a}\right) \tag{5.17}$$

which is generated by shifting and scaling a mother wavelet $\psi(t)$. Its Fourier

transform is:

$$\hat{\psi}_{a,b}(\omega) = \int_{-\infty}^{+\infty} \psi_{a,b}(t) e^{-i\omega t} dt = \int_{-\infty}^{+\infty} \frac{1}{\sqrt{a}} \psi \left(\frac{t-b}{a} \right) e^{-i\omega t} dt \tag{5.18}$$

Assuming $t - b/a = \tau$, Eq. (5.18) becomes:

$$\begin{aligned} \hat{\psi}_{a,b}(\omega) &= \int_{-\infty}^{+\infty} \frac{1}{\sqrt{a}} \psi(\tau) e^{-i\omega(a\tau+b)} a d\tau = \sqrt{a} e^{-i\omega b} \int_{-\infty}^{+\infty} \psi(\tau) e^{-i\omega a\tau} \\ &= \sqrt{a} \hat{\psi}(a\omega) e^{-i\omega b} \end{aligned} \tag{5.19}$$

5.3.1 The Morlet Wavelet

Several study present in literature deal with the use of the wavelet transform applied to acoustic emission localization in isotropic and anisotropic structures (Gaul & Hurlebaus [1999], Jeong & Jang [2000] and Meo *et al.* [2005]). In this study, the complex Morlet wavelet was employed as, in contrast with real wavelets, is able to separate amplitude and phase, enabling the measurement of instantaneous frequencies and their temporal evolution (Mallat [1998]). Furthermore, it was experienced that Morlet wavelet enables the measurement of the localization frequency for signals with faster and slower oscillations, providing a flexible window that narrows at high frequencies and widens when observing low-frequency phenomena. The complex Morlet wavelet is expressed by the following equation (Teolis [1998]):

$$\psi(t) = \frac{1}{\sqrt{\pi F_b}} e^{i\omega_c t} e^{-\frac{t^2}{F_b}} = \frac{1}{\sqrt{\pi F_b}} e^{-\frac{t^2}{F_b}} [\cos(\omega_c t) + i \sin(\omega_c t)] \tag{5.20}$$

and its Fourier transform is:

$$\hat{\psi}(\omega) = e^{-\frac{F_b}{4}(\omega-\omega_c)^2} \tag{5.21}$$

A Morlet wavelet seems like an impulsive waveform with a *central frequency* $f_c = \omega_c/2\pi$ when its *shape control parameter* F_b (wavelet bandwidth) can be set to be a small value. Conversely, when F_b increases, the wavelet waveform

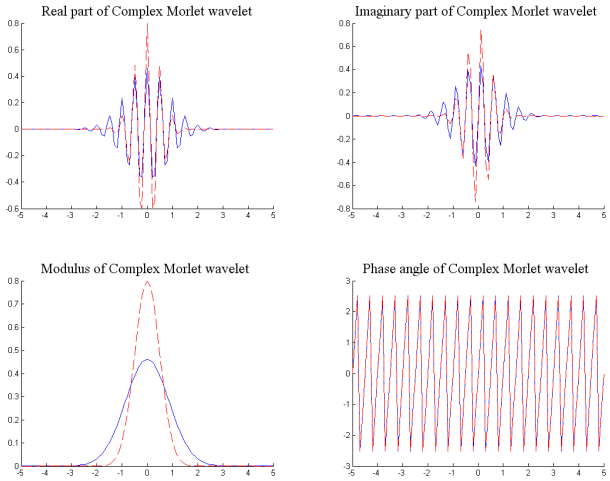

Figure 5.7: The Morlet wavelet with different values of Fb (1.5 blue continuous line, 0.1 red dashed line). In figures (a) and (b) are represented the real and imaginary part of the Morlet wavelet, whilst figures (c) and (d) depict the modulus and the phase angle

tends to be a harmonic waveform (Fig. 5.7). However, for practical purposes, because of the fast decay of its envelope towards zero, Morlet wavelet is considered admissible for $\omega_c \geq 5$. In this research work $\omega_c = 6$ and F_b was chosen equal to 0.1. In addition, the Morlet wavelet's real and imaginary parts as well as the modulus and the phase angle of $\psi(t)$ can be defined as follow:

$$\mathrm{Re}[\psi(t)] = \frac{1}{\sqrt{\pi F_b}} e^{-\frac{t^2}{F_b}} \cos(\omega_c t) \tag{5.22a}$$

$$\mathrm{Im}[\psi(t)] = j\frac{1}{\sqrt{\pi F_b}} e^{-\frac{t^2}{F_b}} \sin(\omega_c t) \tag{5.22b}$$

$$|\psi(t)| = \sqrt{\mathrm{Re}[\psi(t)]^2 + \mathrm{Im}[\psi(t)]^2} \tag{5.22c}$$

$$\angle\psi(t) = \arctan \frac{\mathrm{Im}[\psi(t)]}{\mathrm{Re}[\psi(t)]} \tag{5.22d}$$

The complex Morlet function (5.20) can be considered as a modulated Gaussian function centred at $t = 0$ and its Fourier transform (5.21) centred at $\omega = \omega_c$. The function $\psi_{a,b}(t)$ [Eq. (5.17)] using the Morlet as a mother wavelet is then centred at $t = b$ and its Fourier transform $\hat{\psi}_{a,b}(\omega)$ [Eq. (5.19)] is centred around $\omega = \omega_c/a$. Therefore, Eq. (5.13) can be thought in terms of the time-frequency

representation of the harmonic waveform $u(t)$ around $t = b$ and $\omega = \omega_c/a$.

5.3.2 Time of Arrival Identification

The waveforms recorded are analysed in terms of group (energy) velocity-frequency relationship. The group velocity is defined as the velocity of a modulated wave that is constructed considering a time harmonic motion of two waves of unit amplitude with slightly different frequencies ω_1 and ω_2 propagating in the x-direction of a thin plate, i.e. (Bernard *et al.* [2001]):

$$u(x,t) = e^{-i(k_1 x - \omega_1 t)} + e^{-i(k_2 x - \omega_2 t)} \tag{5.23}$$

where k_1 and k_2 are the wave numbers. Introducing $(k_1+k_2)/2 = k_0$, $(k_1-k_2)/2 = \Delta k$, $(\omega_1 + \omega_2)/2 = \omega_0$ and $(\omega_1 - \omega_2)/2 = \Delta\omega$, Eq. (5.23) becomes:

$$u(x,t) = 2\cos[\Delta k x - \Delta\omega t] e^{-i(k_0 x - \omega_0 t)} \tag{5.24}$$

Eq. (5.24) is a modulated wave formed by a carrier $e^{-i(k_0 x - \omega_0 t)}$ with frequency ω_0 and the modulation $\cos[\Delta k x - \Delta\omega t]$ with frequency $\Delta\omega$. The propagation velocity of the carrier is the phase velocity $c_{ph} = \omega_0/k_0$ and the propagation velocity of the envelope is the group velocity $c_g = d\omega/dk$ in the limit of $\Delta k \to 0$. Substituting Eq. (5.23) in (5.13) using Morlet wavelet (5.20), and assuming $\phi_1 = \omega_1 b - k_1 x$ and $\phi_2 = \omega_2 b - k_2 x$, we obtain:

$$CWT(x,a,b) = \sqrt{a}\left[\hat{\psi}^*(a\omega_1)e^{i\phi_1} + \hat{\psi}^*(a\omega_2)e^{i\phi_2}\right] \tag{5.25}$$

and its complex conjugate is:

$$CWT^*(x,a,b) = \sqrt{a}\left[\hat{\psi}(a\omega_1)e^{-i\phi_1} + \hat{\psi}(a\omega_2)e^{-i\phi_2}\right] \tag{5.26}$$

The squared modulus of the CWT, also known as *scalogram*, indicates the energy density of the signal at each scale at any time (Haase & Widjajakusuma [2003] and Mallat [1998]). Hence, it is able to reveal the highest local energy content of the waveform measured from each transducer. The squared modulus can be

expressed as:

$$|CWT(x,a,b)|^2 = CWT(x,a,b) \cdot CWT^*(x,a,b) \tag{5.27}$$

Substituting Eqs. (5.25) and (5.26) into (5.27), we have:

$$\begin{aligned}|CWT(x,a,b)|^2 = a \Big\{ &[\hat{\psi}(a\omega_1)]^2 + [\hat{\psi}(a\omega_2)]^2 + \hat{\psi}^*(a\omega_1)\hat{\psi}(a\omega_2)e^{i(\phi_1-\phi_2)} \\ &+\hat{\psi}(a\omega_1)\hat{\psi}^*(a\omega_2)e^{-i(\phi_1-\phi_2)} \Big\}\end{aligned} \tag{5.28}$$

If $\Delta\omega$ is sufficiently small such that $\hat{\psi}(a\omega_1) \cong \hat{\psi}(a\omega_2) \cong \hat{\psi}(a\omega_0)$, Eq. (5.28) becomes:

$$\begin{aligned}|CWT(x,a,b)|^2 &\approx 2a[\hat{\psi}(a\omega_0)]^2 \left[1 + \cos(\phi_1 - \phi_2)\right] \\ &\approx 2a[\hat{\psi}(a\omega_0)]^2 \left[1 + \cos(\Delta\omega b - \Delta k x)\right]\end{aligned} \tag{5.29}$$

Therefore, Eq. (5.29) shows that the squared modulus of the CWT using the complex Morlet wavelet reaches its peak value at $a = \omega_c/\omega_0$ and $b = \Delta k x/\Delta\omega = x/c_g$. Hence, the maximum value of the Continuous Wavelet Transform squared modulus coefficients (*ridges*), obtained at the angular frequency of interest ω_0, allows identifying the arrival time (b) of the group velocity c_g (Fig. 5.8).

As depicted in Fig 5.8a, a red patch in the scalogram is representative of the ridge, i.e. the local energy content of the waveform recorded. Fig. 5.8b shows that the red patch in the contour plot of the scalogram associated to the ridge is achieved at the instantaneous frequency $f_0 = 258.77$ kHz. Hence, each frequency of interest, chosen as the dominant frequency in the signal analysed by each sensor at each instant in time, indicates the arrival time of group velocity c_g and can be related to the scale parameter by the following relationship:

$$f_0 = \frac{f_c}{aT} \tag{5.30}$$

where f_0 is the frequency of interest, f_c is the central frequency of the wavelet used and T is the sampling period. The projection on the time domain of the ridge corresponds to the time of arrival (TOA) of the waves packets. Thus, the

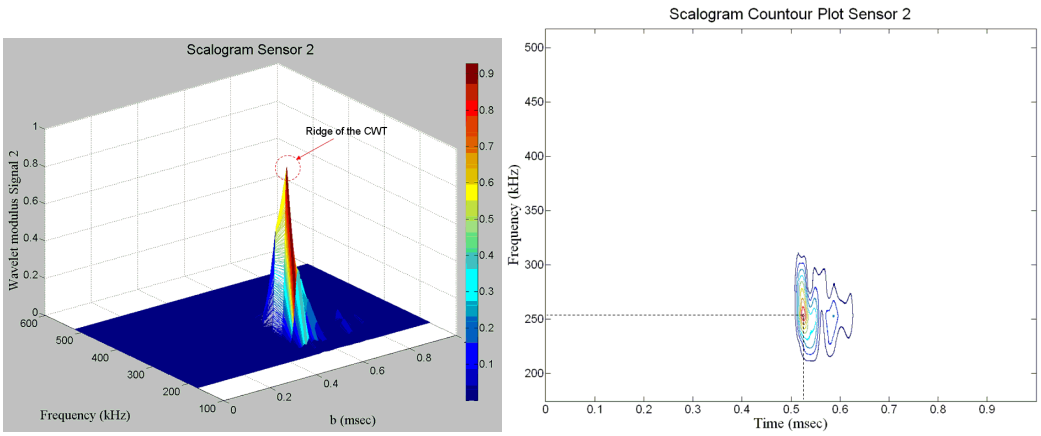

(a) (b)

Figure 5.8: Morlet wavelet scalogram (a) and associated contour plot (b) of the recorded flexural wave

time differences Δt_{1j} with respect to the master sensor can be calculated and substituted in Eqs. (5.5) and (5.9) for isotropic and anisotropic media, respectively. Thereby, the coordinates of the impact source location and group velocity can be identified through the optimization algorithm discussed in the next Section.

5.4 Newton's Method for Solving Systems of Nonlinear Equations

The strategy adopted to solve the set of Eqs. (5.5) and (5.9) and to make the algorithm robust and convergent from almost any guess point was to combine a *Newton's method* with *unconstrained optimization*.

Newton-Raphson or Newton's method is a very efficient iterative algorithm for finding the roots of non linear system of equations, since it locally converges from around an initial guess point $\mathbf{x}_0$ sufficiently close to the root (Dennis & Schnabel [1983]). Let assume $F_i : \mathbb{R}^n \rightarrow \mathbb{R}^n$, where $\mathbb{R}^n$ denotes n-dimensional Euclidean space, to be a twice *Lipschitz* continuously differentiable function. The set of non

linear equations (5.5) and (5.9) can be expressed as:

$$\mathbf{F}(\mathbf{x}) = 0 \tag{5.31}$$

where $\mathbf{F}$ is the vector of the functions F_i ($i = 1, \ldots, N$ with $N = 4$ or $N = 6$ depending on the algorithm used for isotropic or anisotropic media, respectively), and $\mathbf{x}$ is the vector of the unknowns x_j ($j = 1, \ldots, N$) corresponding to the coordinates of the impact location, the group velocities and the time of arrival at the master sensor. Eq. (5.31) has a zero at $\mathbf{x}^*$ such that $\mathbf{F}(\mathbf{x}^*) = 0$. Newton's method converges quadratically to $\mathbf{x}^*$ (i.e. the order of convergence is approximately two) by computing the Jacobian linearisation of the function $\mathbf{F}$ around a guess point $\mathbf{x}_0$, and then using this linearisation to move closer to the desired zero. The Newton iterate $\mathbf{x}^{n+1}$ from a current point $\mathbf{x}^n$ is given by:

$$\mathbf{x}^{n+1} = \mathbf{x}^n + \delta\mathbf{x}^n = \mathbf{x}^n - [\mathbf{J}(\mathbf{x}^n)]^{-1} \cdot \mathbf{F}(\mathbf{x}^n) \tag{5.32}$$

where $\delta\mathbf{x}$ is the Newton step and $\mathbf{J}(\mathbf{x})$ is the Jacobian matrix, which contains first derivatives of the objective function $\mathbf{F}(\mathbf{x})$ with respect to the unknowns of the problem:

$$\mathbf{J}(\mathbf{x}) = \frac{\partial \mathbf{F}(\mathbf{x})}{\partial \mathbf{x}} = \begin{pmatrix} \frac{\partial F_1(\mathbf{x})}{\partial x_1} & \frac{\partial F_1(\mathbf{x})}{\partial x_2} & \cdots & \frac{\partial F_1(\mathbf{x})}{\partial x_N} \\ \frac{\partial F_2(\mathbf{x})}{\partial x_1} & \frac{\partial F_2(\mathbf{x})}{\partial x_2} & \cdots & \frac{\partial F_2(\mathbf{x})}{\partial x_N} \\ \vdots & \vdots & \ddots & \vdots \\ \frac{\partial F_N(\mathbf{x})}{\partial x_1} & \frac{\partial F_N(\mathbf{x})}{\partial x_2} & \cdots & \frac{\partial F_N(\mathbf{x})}{\partial x_N} \end{pmatrix} \tag{5.33}$$

In practical optimization problem, different criteria for terminating the iteration are used. In particular, if $\mathbf{J}(\mathbf{x}^*)$ is well conditioned, a good indicator of the size of the error for Newtons method may be when the relative non linear residual $\|\mathbf{F}(\mathbf{x})\|/\|\mathbf{F}(\mathbf{x}_0)\|$ is small. Hence, introducing the relative error tolerance τ_r and absolute error tolerance τ_a, this condition can be expressed by:

$$\|\mathbf{F}(\mathbf{x})\| \leq \tau_r \|\mathbf{F}(\mathbf{x}_0)\| + \tau_a \tag{5.34}$$

Advantages	Disadvantages
Quadratically convergent from good starting guesses if $\mathbf{J}(\mathbf{x}^*)$ is not singular Exact solution at each iteration for any affine component functions of $\mathbf{F}(\mathbf{x}^n)$	Not globally convergent for many problems Requires the Jacobian matrix $\mathbf{J}(\mathbf{x}^n)$ at each iteration and the Newton step $\delta\mathbf{x}^n$ must not be too large

Table 5.1: Advantages and disadvantages of local Newton's method

Since the iterations are very sensitive to the initial iterate, if the starting point is near a root $\mathbf{x}^*$ or the computation and factorization of the Jacobian are inexpensive, the value of the norm of Newton step $\|\delta\mathbf{x}^n\|$ smaller than a desired tolerance, can be used as an accurate estimate of the error $\mathbf{e}^n$:

$$\|\mathbf{e}^n\| = \|\delta\mathbf{x}^n\| + o\left(\|\mathbf{e}^n\|^2\right) \tag{5.35}$$

The following table (Tab. 5.1) summarizes the advantages and disadvantages of Newton's method. However, such technique can be modified and enhanced in various ways for solving systems of nonlinear equations, but in particular conditions, when the starting point is not near the root, it may not converge (Nocedal & Wright [1999]). The reasons for this failure are that the direction of the current iterate $\mathbf{x}^n$ may differ to be a direction of descent for $\mathbf{F}$, and, even if a search direction is a direction of decrease of $\mathbf{F}$, the length of the Newton step $\delta\mathbf{x}$ may be too large. Hence, a globally convergent algorithm associated to a Newton's method can be designed to find the solution of a system of nonlinear equations from almost any guess point $\mathbf{x}_0$. The approach adopted in this thesis was to combine the Newton's method applied to the systems (5.5) and (5.9) with the unconstrained problem of minimizing the *objective function* $\mathbf{F}$:

$$\min_{\mathbf{x}\in\mathbb{R}^n} \mathbf{F} : \mathbb{R}^n \to \mathbb{R}^n \tag{5.36}$$

In unconstrained optimization, the most widely used function to be minimized (also known as *merit function*) is a scalar-valued function of $\mathbf{F}$, i.e. the squared

norm of $\mathbf{F}$:

$$h(\mathbf{x}) = \frac{1}{2}\|\mathbf{F}(\mathbf{x})\|^2 = \frac{1}{2}\mathbf{F}(\mathbf{x}) \cdot \mathbf{F}(\mathbf{x}) \tag{5.37}$$

where the factor $1/2$ is introduced for convenience. Obviously, any root of h fulfils the identity $h(\mathbf{x}^*) = 0$. Among the class of powerful algorithms for unconstrained optimization, in this thesis we will focus on the line search methods because of their simplicity, and because they do not depend on how the Jacobian is obtained. Furthermore, if the initial Newton step is proved to be unsatisfactory, the polynomial backtracking method will be considered.

5.4.1 Line Search Methods with Polynomial Backtracking

In line search method, the algorithm chooses a direction $\delta\mathbf{x}^n$ and searches along this direction from the current iterate to find out a new iterate $\mathbf{x}^{n+1}$ that guarantees a lower value of $h(\mathbf{x})$. The iteration is expressed by the following formula (Dennis & Schnabel [1983]):

$$\mathbf{x}^{n+1} = \mathbf{x}^n + \lambda^n \delta\mathbf{x}^n \qquad 0 < \lambda \leq 1 \tag{5.38}$$

where λ is called *step length*. Whether the initial iterate $\mathbf{x}_0$ is close to the solution, the common strategy is to use a full Newton step $\delta\mathbf{x}^n$ by setting $\lambda = 1$. Otherwise, a sufficiently small value of λ is tried by moving along the Newton direction until $\mathbf{x}^{n+1}$ satisfies the following criterion (known as *Armijo condition*):

$$h(\mathbf{x}^n + \lambda^n \delta\mathbf{x}^n) \leq h(\mathbf{x}^n) + \alpha\lambda^n \nabla[h(\mathbf{x}^n)]^T \cdot \delta\mathbf{x}^n \tag{5.39}$$

A good value of the parameter α is 10^{-4}. The *descent direction* of the Newton step from the current point $\mathbf{x}^n$ to a new point $\mathbf{x}^{n+1}$ is verified by the fact that the directional derivative of h at $\mathbf{x}^n$ in the direction $\delta\mathbf{x}^n$ is negative:

$$\begin{aligned} \nabla[h(\mathbf{x}^n)]^T \cdot \delta\mathbf{x}^n &= \frac{1}{2}\nabla\left[\mathbf{F}(\mathbf{x}^n) \cdot \mathbf{F}(\mathbf{x}^n)\right] \cdot \delta\mathbf{x}^n \\ &= \left[\mathbf{F}(\mathbf{x}^n) \cdot \mathbf{J}(\mathbf{x}^n)\right] \cdot \left\{-[\mathbf{J}(\mathbf{x}^n)]^{-1} \cdot \mathbf{F}(\mathbf{x}^n)\right\} < 0 \end{aligned} \tag{5.40}$$

In the second criterion (known as *curvature condition*) is required that the decrease of h from $\mathbf{x}^{n+1}$ in the descent direction must be larger than some fraction β of the rate of decrease of f at $\mathbf{x}^n$:

$$\nabla[h(\mathbf{x}^n + \lambda^n \delta\mathbf{x}^n)]^T \cdot \delta\mathbf{x}^n \geq \beta \nabla[h(\mathbf{x}^n)]^T \cdot \delta\mathbf{x}^n \qquad \beta \in (\alpha, 1) \tag{5.41}$$

Typical value of β is 0.9 when the search direction $\delta\mathbf{x}^n$ is chosen by a Newton's method. Both conditions (5.39) and (5.41) are known collectively as the *Wolfe condition*.

In practise, to avoid small steps, it would be more advantageous to perform a polynomial backtracking method (Dennis & Schnabel [1983]) rather than using the curvature condition (5.41). Such technique consists in finding the value of λ that minimizes the model of the following polynomial function:

$$g(\lambda^n) = h(\mathbf{x}^n + \lambda^n \delta\mathbf{x}^n) \tag{5.42}$$

Hence, given any descent direction $\delta\mathbf{x}^n$, Eq. (5.42) satisfies (5.39) and (5.40) such that:

$$g'(\lambda^n) = \nabla[h(\mathbf{x}^n)]^T \cdot \delta\mathbf{x}^n \tag{5.43}$$

Initially, the model of g is given and assumed linear:

$$\begin{aligned} g(0) &= h(\mathbf{x}^n) \\ g'(0) &= \nabla[h(\mathbf{x}^n)]^T \cdot \delta\mathbf{x}^n \end{aligned} \tag{5.44}$$

Settings $\lambda_0 = 1$, if the model satisfies the following condition:

$$g(1) > g(0) + \alpha g'(0) \tag{5.45}$$

the search is terminated. Otherwise, $g(\lambda)$ is expressed through a quadratic approximation by interpolating the three information available, $g(0)$, $g(1)$ and $g'(0)$:

$$g_q(\lambda) \approx [g(1) - g(0) - g'(0)]\lambda^2 + g'(0)\lambda + g(0) \tag{5.46}$$

The new value λ_1 is defined as the minimum of $g_q(\lambda)$:

$$\lambda_1 = -\frac{g'(0)\lambda_0^2}{2[g(1) - g(0) - g'(0)]} \tag{5.47}$$

If λ_1 is too small the quadratic model is poorly accurate and we set a limit value of λ, $\lambda_{\min} = 1$. Conversely, a cubic model of $g(\lambda)$ is more acceptable since it provides more accuracy especially in situations where h has a negative curvature:

$$g_c(\lambda) = a\lambda^3 + b\lambda^2 + g'(0)\lambda + g(0) \tag{5.48}$$

From Eq. (5.48), solving with respect to the coefficients a and b, we obtain a set of two equations using the last two previous values of λ [$g(\lambda_0)$ and $g(\lambda_1)$]:

$$\begin{pmatrix} a \\ b \end{pmatrix} = \frac{1}{\lambda_0^2\lambda_1^2(\lambda_1 - \lambda_0)} \begin{pmatrix} \lambda_0^2 & -\lambda_1^2 \\ -\lambda_0^3 & \lambda_1^3 \end{pmatrix} \begin{pmatrix} g(\lambda_1) - g(0) - g'(0)\lambda_1 \\ g(\lambda_2) - g(0) - g'(0)\lambda_2 \end{pmatrix} \tag{5.49}$$

By differentiating Eq. (5.48), the minimum point λ_2 is given by:

$$\lambda_2 = -\frac{-b + \sqrt{b^2 - 3ag'(0)}}{3a} \tag{5.50}$$

Therefore, if any λ_i is either too close and smaller than λ_{i-1}, λ_i must be limited between the values $\lambda_{\max} = 0.5\lambda_{i-1}$ and $\lambda_{\min} = 0.1\lambda_i$. This procedure allows obtaining reasonable progress in each iteration, and the final λ will not be too small. Thereby, the algorithm was optimized and using the code written in Matlab on a standard PC, the computational time for each source location was less than 1 s.

5.5 Experimental Set-up

Two different experiments were carried out for the validation of the algorithm for **isotropic materials**.

- In *test 1a*, an aluminium plate with dimensions 520 mm × 410 mm × 0.97 mm was employed with four commercially available piezoelectric-film (PVDF) sensors (thickness 110 μm, length 420 μm) adhesively surface bonded (Fig. 5.9). The impacts were generated by dropping a 9 mm

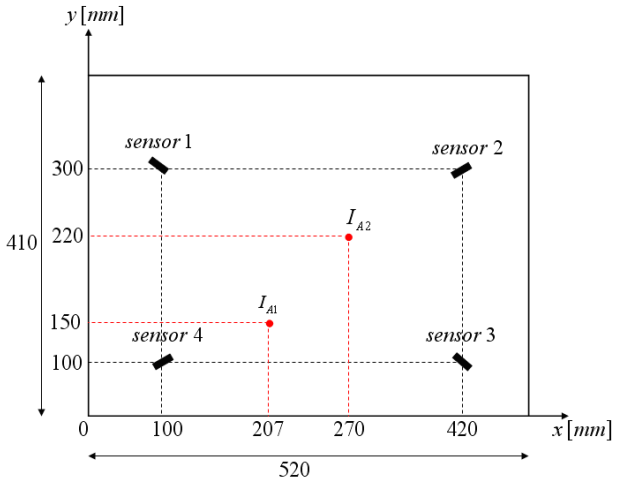

Figure 5.9: Experimental set-up and sensors arrangement in test 1a

	Sensor1	**Sensor2**	**Sensor3**	**Sensor4**	**Impact A1**	**Impact A2**
x-coordinate (mm)	100	420	420	100	207	270
y-coordinate (mm)	300	300	100	100	150	220

Table 5.2: Sensors and impact coordinates in test 1a, impacts A1 and A2

diameter steel ball on the surface of the plate in two different positions. Sensors location and impact source coordinates (referred as A1 and A2) are reported in Tab 5.2.

- *Test 2a* consisted of an aluminium plate with dimensions 1487 mm × 999 mm × 0.98 mm instrumented with four 300 kHz Acoustic Emission sensors, provided by courtesy of Airbus UK (Fig. 5.10). Each sensing unit is certified to provide high SNR (nearly 45 dB) and it is composed by acoustic emission sensors, preamplifiers, power supplies and pass-band filters, connected by low-noise cables. The gain of the preamplifiers is 40 dB, whilst the input impedance of the filters is 50 Ohm. The AE transducers were attached to the surface of the plate using non-corrosive coupling gel. They were firstly connected to pass-band filters with a frequency range between 200 and 400 kHz and then linked to pre-amplifiers. According to the g_{31} electromechanical coupling mechanism of the acoustic emission sensors (see Sec. 2.1.2.1),

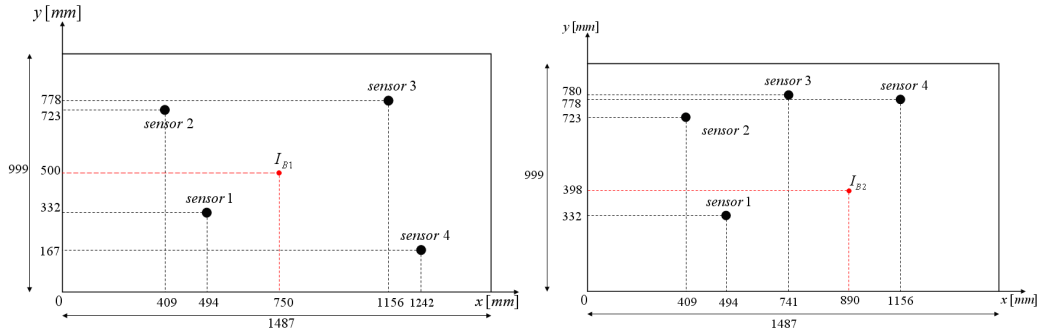

Figure 5.10: Experimental set-up and sensors arrangement in test 2a

	Sensor1	**Sensor2**	**Sensor3**	**Sensor4**	**Impact B1**
x-coordinate (mm)	494	409	1156	1242	750
y-coordinate (mm)	332	723	778	167	500

Table 5.3: Sensors and impact coordinates in test 2a, impact B1

at the mentioned finite bandwidth, only the fundamental antisymmetric Lamb wave A_0 was measured (Tzou [2003]). Two different configurations of the transducers location were studied, and the impacts were induced by a hand-held modal hammer, manufactured by Meggit-Endevco. Tab. 5.3 and 5.4 show the sensors and impact coordinates (referred as B1 and B2) in both configurations.

For the signal acquisition, a four channel oscilloscope (Tektronic TDS 3014) with a sampling rate of 2 MHz was used, and it was triggered by one of the sensors (master sensor). The time histories of the signals received by the sensors were stored on a computer and processed using a Matlab software code implemented by the author.

	Sensor1	**Sensor2**	**Sensor3**	**Sensor4**	**Impact B2**
x-coordinate (mm)	494	409	741	1156	890
y-coordinate (mm)	332	723	780	778	398

Table 5.4: Sensors and impact coordinates in test 2a, impact B2

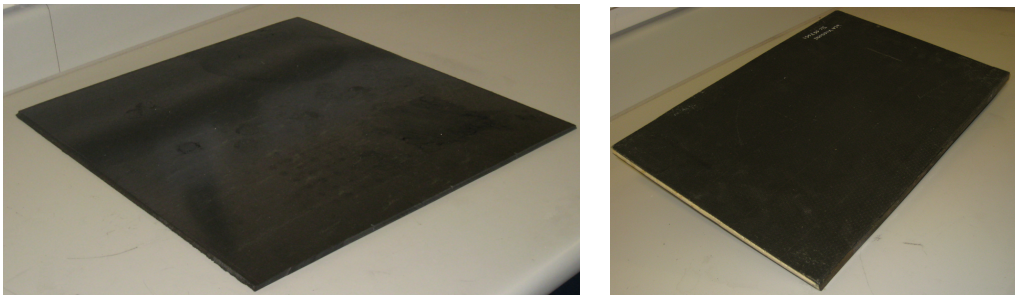

(a) (b)

Figure 5.11: CFRP composite laminate (a) and sandwich plate (b)

Young Mod. $\mathbf{E}_{11}(GPa)$	**Young Mod.** $\mathbf{E}_{22}(GPa)$	**Young Mod.** $\mathbf{E}_{33}(GPa)$	**Shear Mod.** $\mathbf{G}_{12}(GPa)$	**Shear Mod.** $\mathbf{G}_{23}(GPa)$	**Shear Mod.** $\mathbf{G}_{31}(GPa)$	**Poisson's ratio** ν_{12}	**Poisson's ratio** ν_{13}	**Poisson's ratio** ν_{23}
130	9.5	9.8	4.7	3.2	4.7	0.34	0.66	0.52

Table 5.5: T300/914 mechanical properties

To validate the impact detection algorithm for **anisotropic media**, experimental location tests were conducted on two different composite structures:

- In *test1b* a T300/914 carbon fibre reinforced plastic (CFRP) composite laminate with dimensions 502 mm × 437 mm × 6.94 mm and lay-up sequence of $[0/15/30/45/60/75/90]_{3s}$ was used (Fig. 5.11a). The ply properties are reported in Tab. 5.5.

- In *test2b* a sandwich composite plate with dimensions of 380 mm long, 254 mm wide (Fig. 5.11b) was employed. The core used in the sandwich was a 6.35 mm thick HRH-10-1/8-4.0 Aramid fibre/phenolic resin nomex. Facing skins (2mm thick) were made of four plies of AS4/8552 unidirectional carbon/epoxy prepreg composite on both sides of the core with lay-up sequence of [90/45/45/90]. The ply and sandwich properties are reported in Tab. 5.6 and 5.7, respectively.

The A_0 Lamb waves were generated using a hand-held modal hammer, and the waveforms were measured with the six acoustic emission sensors already employed

Young Mod. $\mathbf{E}_{11}(GPa)$	**Young Mod.** $\mathbf{E}_{22}(GPa)$	**Young Mod.** $\mathbf{E}_{33}(GPa)$	**Shear Mod.** $\mathbf{G}_{12}(GPa)$	**Shear Mod.** $\mathbf{G}_{23}(GPa)$	**Shear Mod.** $\mathbf{G}_{31}(GPa)$	**Poisson's ratio** ν_{12}	**Poisson's ratio** ν_{13}	**Poisson's ratio** ν_{23}
122	9.8	9.8	5.12	5.12	3.35	0.26	0.26	0.47

Table 5.6: AS4/8552 mechanical properties

Young Mod. compacted material (GPa)	**Transverse Mod.** (GPa)	**Shear Mod. expansion** (MPa)	**Shear Mod. ribbon** (MPa)	**Poisson's ratio**	**Densification strain**
1	0.41	89	44	0.25	0.8

Table 5.7: Sandwich core mechanical properties

in the experiments with the aluminium specimens. The signals were acquired using two four channels oscilloscopes (Picoscope 4224) with 16 bits of resolution and a sampling rate of 25 MHz. Both systems were synchronized in way that all the transducers were triggered by one of the sensors (master sensor). Sensors location and impact source coordinates are reported in Tab. 5.8 for test 1b with CFRP (referred as impacts C1 C2 and C3) and Tab. 5.9 and 5.10 for test 2b with sandwich plate (referred as impacts S1 S2 and S3).

5.6 Impact Localization Results

According to Sec. 5.3.2, the signals were analysed in terms of group (energy) velocity-frequency relationship. Numerical routines were developed to find the A_0 Lamb wave mode peaks in isotropic and anisotropic structures, in order to extract the wave packets' arrival times with largest energy contribution (ridges

	Sens. 1	**Sens. 2**	**Sens. 3**	**Sens. 4**	**Sens. 5**	**Sens. 6**	**Imp. C1**	**Imp. C2**	**Imp. C3**
x-coordinate (mm)	120	110	250	280	430	420	280	270	420
y-coordinate (mm)	100	120	390	390	250	230	170	240	70
d_{km} (mm)	22.3		30		22.3				

Table 5.8: Sensors and impact coordinates in test 1b, impacts C1, C2 and C3

	Sensor1	Sensor2	Sensor3	Sensor4	Sensor5	Sensor6	Impact S1
x-coordinate (mm)	120	110	190	210	320	330	210
y-coordinate (mm)	50	70	210	190	140	120	90
d_{km} (mm)	22.3		28.3		22.3		

Table 5.9: Sensors and impact coordinates in test 2b, impact S1

	Sensor 1	Sensor 2	Sensor 3	Sensor 4	Sensor 5	Sensor 6	Impact S2	Impact S3
x-coordinate (mm)	100	90	170	190	310	290	190	50
y-coordinate (mm)	50	70	220	210	140	120	140	225
d_{km} (mm)	22.3		22.3		28.3			

Table 5.10: Sensors and impact coordinates in test 2b, impact S2 and S3

of the scalogram).

5.6.1 Source Location Results on Aluminium Plates

The maxima coefficients of the scalogram in both experiments were found at two different frequencies, 3452 Hz for test 1a with the PVDF sensors (Fig. 5.12) and 273.4 kHz for test 2a with acoustic emission transducers (Fig. 5.13 and 5.14). Therefore, arrival times of the flexural waves were identified at these instantaneous frequencies. Nevertheless, it was noticed that the frequencies of interest 3452 Hz for the impacts A1 and A2 and 273.4 kHz for impacts B1 and B2 were not the same for all four sensors. This can be seen in sub-figure (c) of Fig. 5.12, sub-Fig. (a) and (c) of Fig. 5.13 and sub-figure (c) of Fig. 5.14, wherein the time representation of the wavelet coefficients does not seem to match the maximum of contour plot of the relative scalogram. However, for those transducers for which the scalogram maximum coefficients resulted different, the associated frequency was approximately the same (a maximum difference of 10 Hz) with respect to the values mentioned above. This means that the arrival time evaluation error due to this frequency shift is negligible.

The results of the predicted impact source location for both configurations in test 1a and 2a are shown in Fig. 5.15.

Tab. 5.11 reports the results of source location in terms of location error ξ defined

	Impact A1	Impact A2	Impact B1	Impact B2
x_{algor} (mm)	209.8	267.2	752.23	891.69
x_{real} (mm)	207	270	750	890
y_{algor} (mm)	148.6	218.4	497.67	401.42
y_{real} (mm)	150	220	500	398
ξ (mm)	3.13	3.22	3.21	3.63

Table 5.11: Impact positions and errors for test 1a and 2a

by the following formula:

$$\xi = \sqrt{(x_{\text{real}} - x_{\text{algor}})^2 + (y_{\text{real}} - y_{\text{algor}})^2} \tag{5.51}$$

where $(x_{\text{real}}, y_{\text{real}})$ are the coordinates of the real impact position and $(x_{\text{algor}}, y_{\text{algor}})$ the coordinates of the impact location using the algorithm reported in Sec. 5.1.

As it can be seen from Tab. 5.11, this algorithm generates results with reasonable accuracy (maximum error in estimation of the coordinates of the impact location was less than 4 mm) for both types of impacts considered. In addition, from the test 2a it was observed that whether the distance of the transducer from the impact source was bigger than 650 mm, the effects from the edges of the plate and the reflected waves led to a wrong estimation of the stress waves arrival time. Hence, an error of 27% on the impact source location was induced. This information can be useful for the optimal location of sensors bonded in large isotropic structures.

5.6.2 Source Location Results on CFRP Laminate

The maxima coefficients in test 1b with a quasi-isotropic CFRP plate were found at the instantaneous frequency of 258.77 kHz. Fig. 5.16 illustrates the procedure for extracting the TOA at the above frequency of interest for the sensor configuration reported in test 1b and impact C1. Fig. 5.17 shows the results of the source location for impacts C1, C2 and C3 in test 1b. As in Fig. 5.15, the real source location is represented by an open circle (o), whilst the calculated source impact position is illustrated by a star symbol (*).

Tab. 5.12 depicts the evaluated impact positions and the error as expressed by Eq. (5.51). As it can be seen from Tab. 5.12, this algorithm provides results

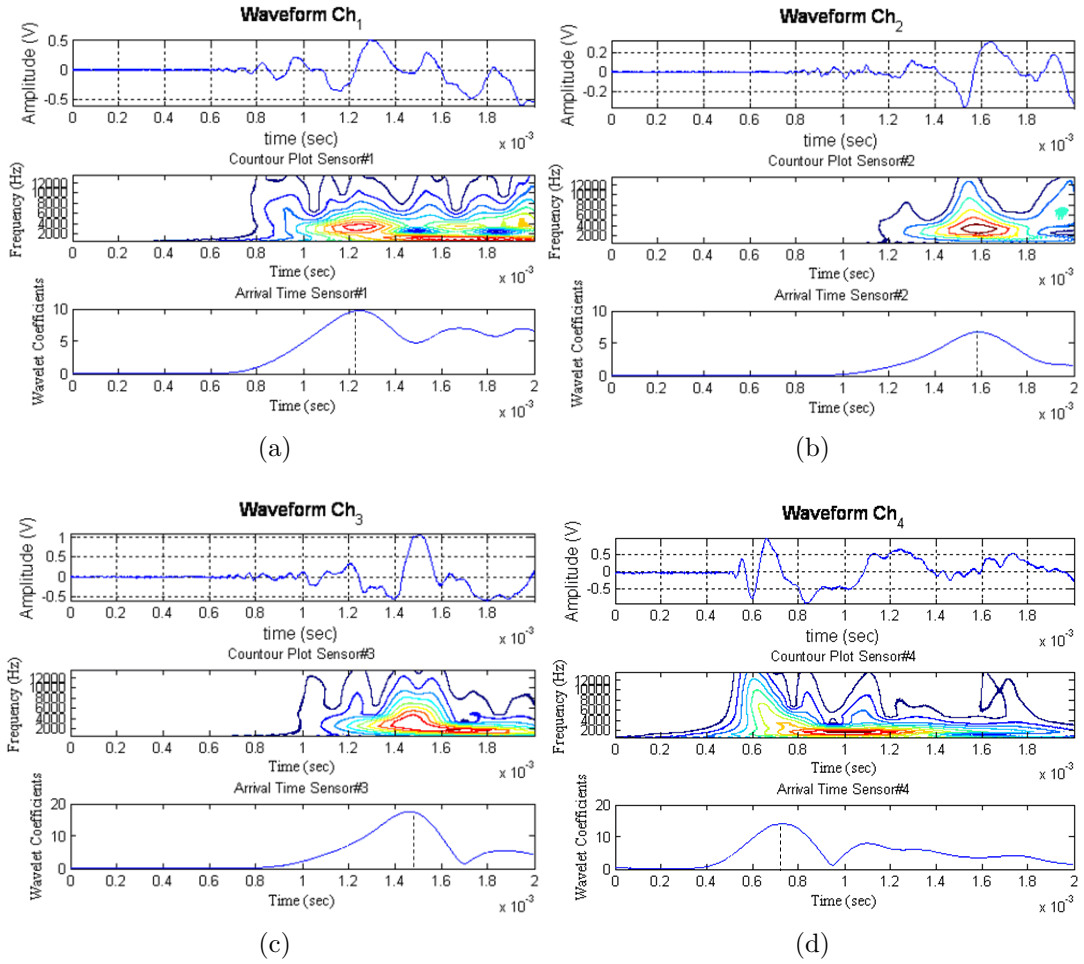

Figure 5.12: Each sub-figure illustrates the time histories of the four signals measured by the PVDF transducers, the contour-plot of the scalogram of the CWT and line profile of the scalogram illustrating the procedure to extract the TOA at $f_0 = 3452$ Hz for test 1a and impact A1

	Impact C1	**Impact C2**	**Impact C3**
x_{algor} (mm)	277.56	268.32	417.89
x_{real} (mm)	280	270	420
y_{algor} (mm)	172.43	242.12	67.35
y_{real} (mm)	170	240	70
ξ (mm)	3.44	2.7	3.38

Table 5.12: Impact positions and errors for test 1b

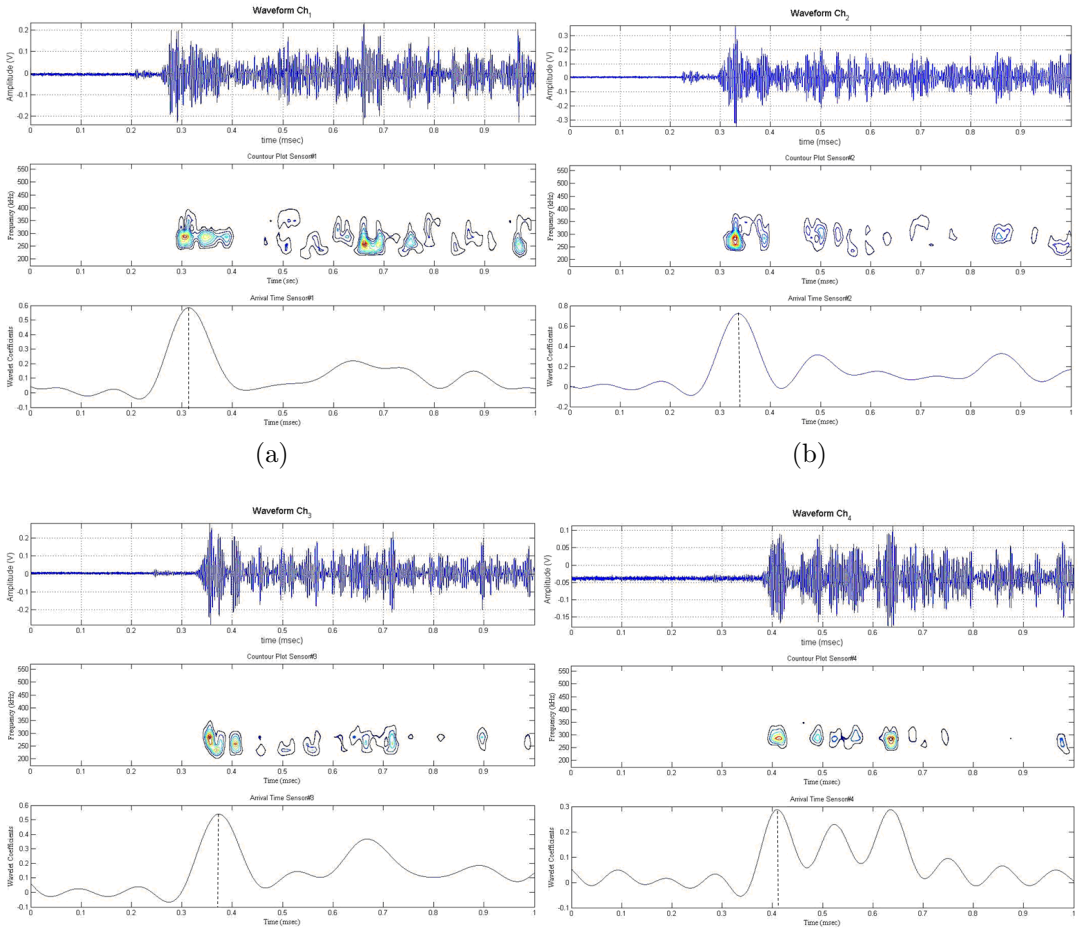

Figure 5.13: Each sub-figure illustrates the time histories of the four signals measured by the acoustic emission transducers, the contour-plot of the scalogram of the CWT and line profile of the scalogram illustrating the procedure to extract the TOA at $f_0 = 273.4$ kHz for test 2a and impact B1

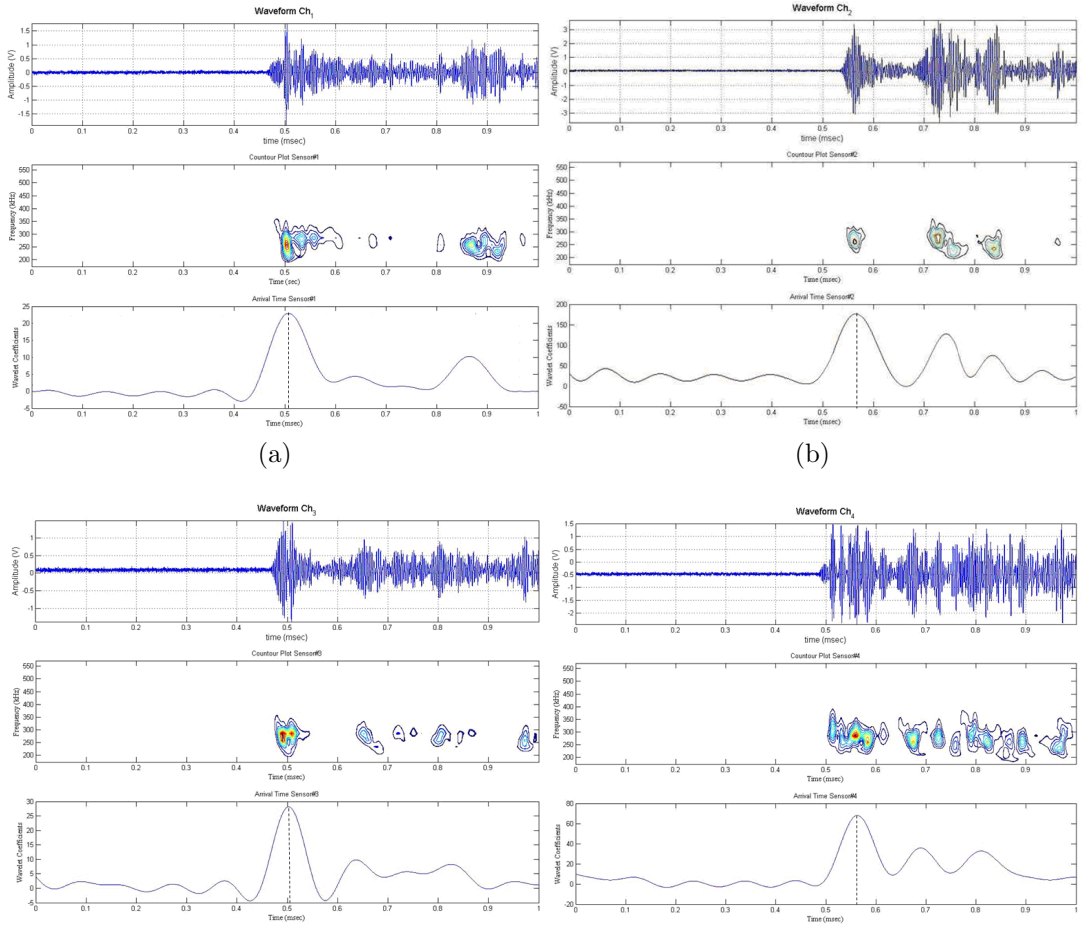

Figure 5.14: Each sub-figure illustrates the time histories of the four signals measured by the acoustic emission transducers, the contour-plot of the scalogram of the CWT and line profile of the scalogram illustrating the procedure to extract the TOA at $f_0 = 273.4$ kHz for test 2a and impact B2

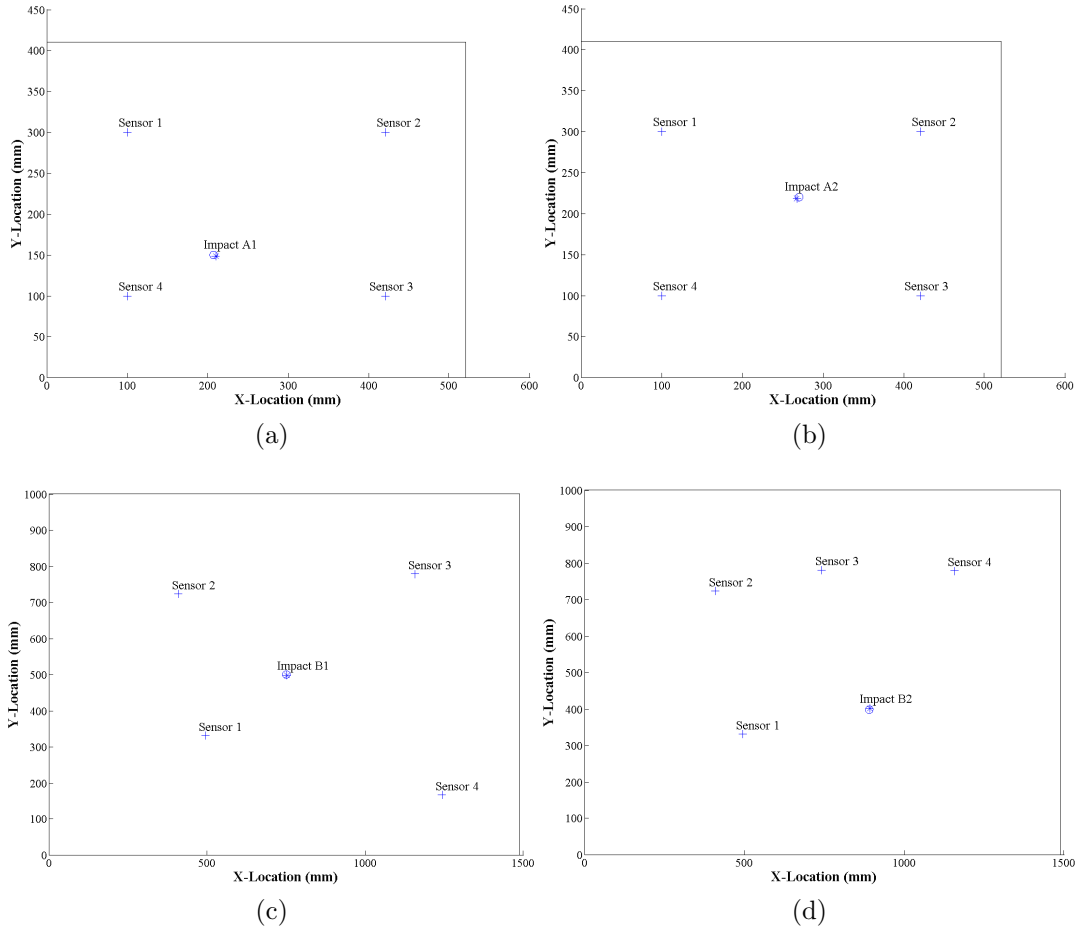

Figure 5.15: Source location results of test 1a (a) - (b) and test 2a (c) - (d). The calculated and true impact positions are shown as an open circle (o) and a star (*), respectively. The sensor positions are represented by a plus sign (+)

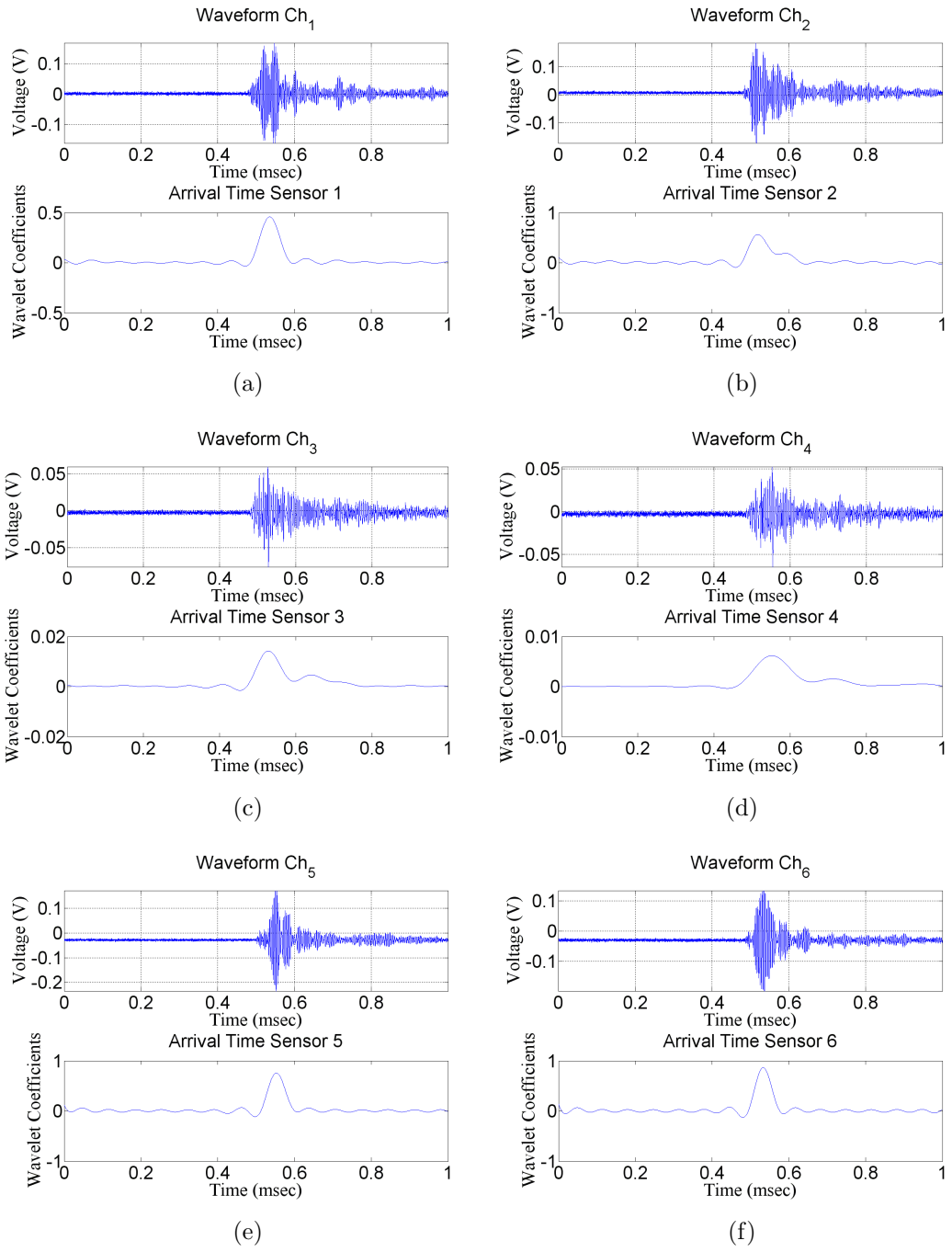

Figure 5.16: Time histories of the six recorded waveform (upper side) and the line profile of the scalogram (lower side) at the frequency $f_0 = 258.77$ kHz for the time of arrival identification in impact C1

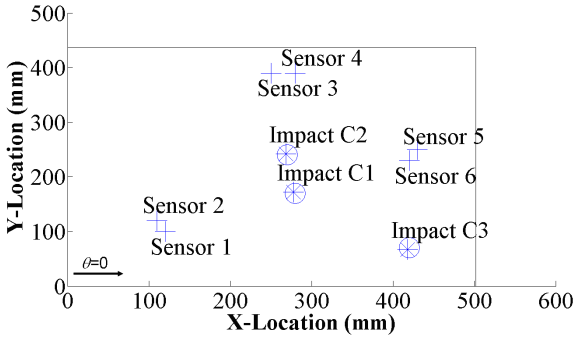

Figure 5.17: Source location results for impacts C1, C2 and C3

	Impact S1	**Impact S2**	**Impact S3**
x_{algor} (mm)	211.71	188.23	51.67
x_{real} (mm)	210	190	50
y_{algor} (mm)	89.18	141.07	226.45
y_{real} (mm)	90	140	225
ξ (mm)	1.89	2.07	2.21

Table 5.13: Impact positions and errors for test 2b

with satisfactory accuracy (maximum error in estimation of the coordinates of the impact location was approximately 3 mm) for all the impacts considered, even outside the area defined by the sensors.

5.6.3 Source Location Results on Sandwich Panel

The scalogram maxima coefficients test 2b with the sandwich plate were found at the instantaneous frequency of 348.27 kHz. Fig. 5.18 shows the procedure for extracting the TOA at the above frequency of interest, for the configuration reported in test 2b, impact S1. Fig. 5.19 depicts the results of the source location for for impacts S1, S2 and S3 in test 2b. Tab. 5.13 reports the evaluated impact positions and the associated errors.

As it can be seen from Tab. 5.13, this algorithm generates results with reasonable accuracy (maximum error in estimation of the coordinates of the impact location was approximately 2 mm) even in complex structures as sandwich panels. In the experiments on both CFRP and sandwich plate, according to Eq. (5.7), the maximum distance between any pair of sensors was assumed equal to

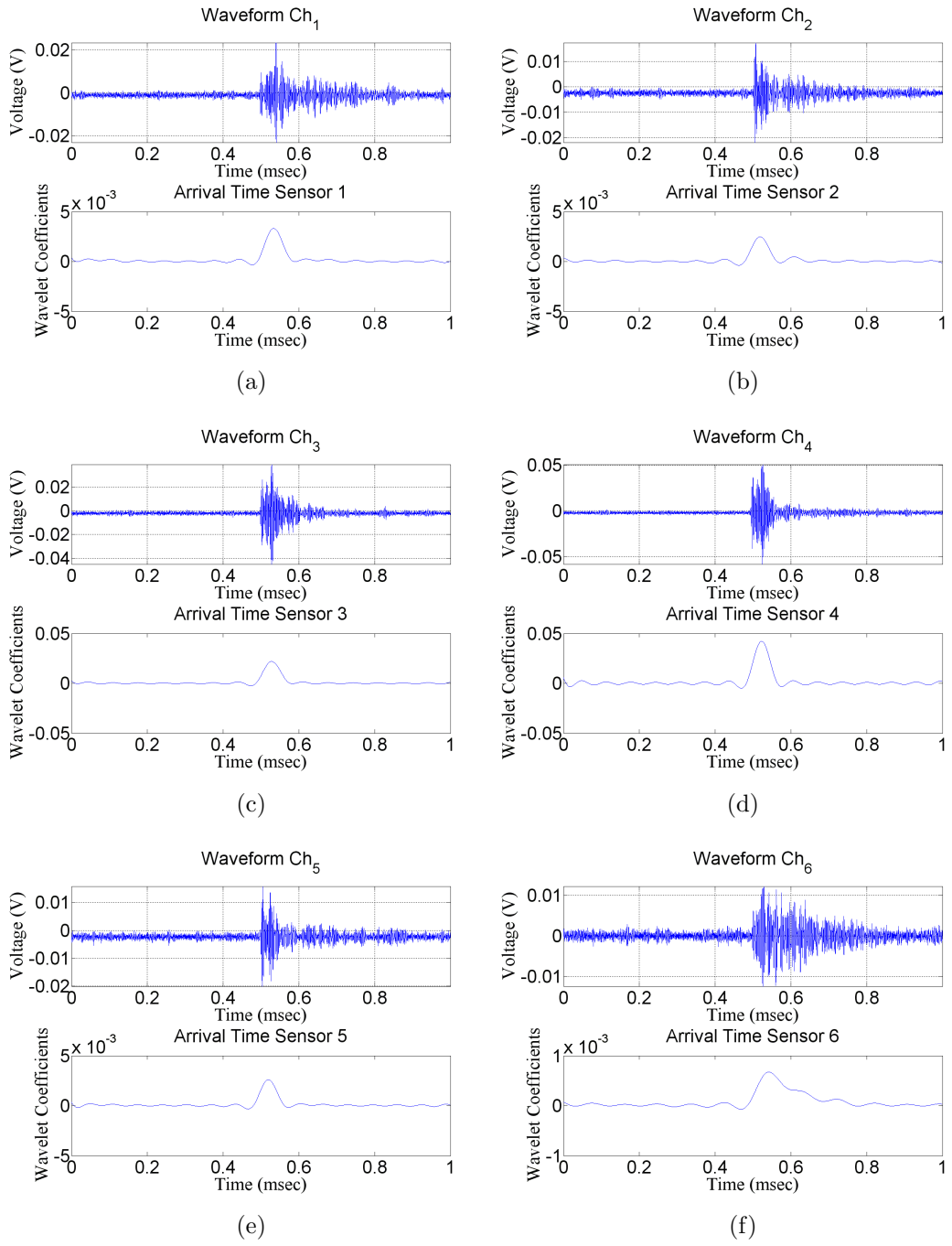

Figure 5.18: Time histories of the six recorded waveform (upper side) and the line profile of the scalogram (lower side) at the frequency $f_0 = 348.27$ kHz for the time of arrival identification in impact S1

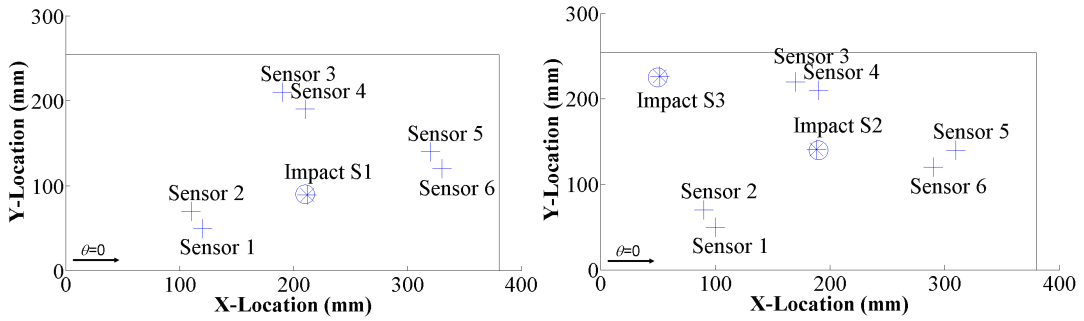

Figure 5.19: Source location results for impact S1, S2 (a) and S3 (b)

approximately one third of the distance of the closest transducer from the impact location. It was observed during the test on the sandwich plate that due to the severe attenuation in the resin core, the peak magnitude of the scalogram for each pair of transducers occurred at slightly different frequencies (within a band Δf_0 of 10 Hz) with respect to the nominal value of 348.27 kHz. This means that the TOA evaluation error due to this frequency shift was negligible.

5.7 Group Velocity Results

The values of the fundamental antisymmetrical Lamb mode A_0 obtained from the optimization algorithms were compared with those determined through an analytical approach using the Rayleigh-Lamb frequency relations (see Sec. 3.2) and a semi-analytical finite element method (see Sec. 3.3) for isotropic and anisotropic materials, respectively.

5.7.1 Group Velocity Evaluation on Aluminium Plates

Tab. 5.14 reports the values of the flexural group speed A_0 in the aluminium specimens for both test 1a and 2a determined in the optimization procedure, and those obtained from the dispersion curve defined by Eq. (3.34), and illustrated in Fig. 5.20.

From Tab. 5.14 it can be clearly seen that the maximum error in the estimation of the wave velocity for both test 1a and 1b was about 3 m/s.

	Impact A1	Impact A2	Impact B1	Impact B2
A_0 from algorithm (m/s)	439.4	442.6	1364.34	1353.05
A_0 from dispersion curves (m/s)	441	441	1350	1350

Table 5.14: Flexural Lamb wave velocity results for test 1a and 2a

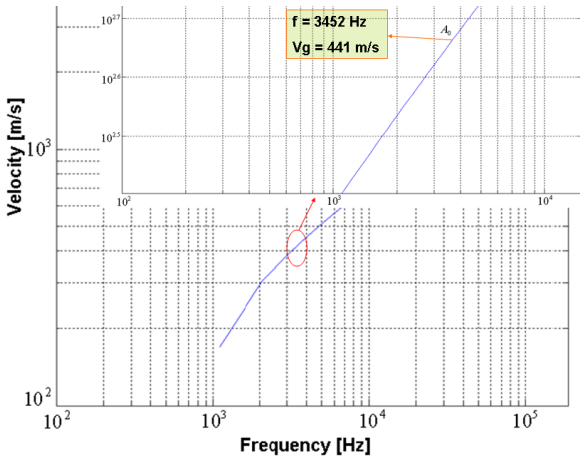

(a)

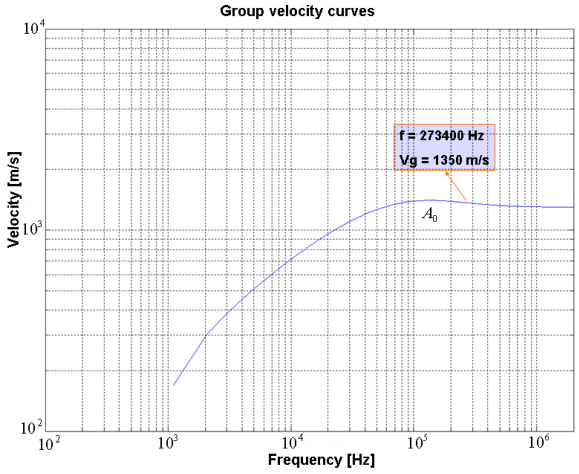

(b)

Figure 5.20: Dispersion curves of fundamental antisymmetrical Lamb mode for both aluminium plates. From test 1a (a), @ 3452 Hz the correspondent group velocity is at 441 m/s, whilst in test 2a (b), @ 273.4 kHz the correspondent group velocity is at 1350 m/s

		Impact C1	Impact C2	Impact C3
A_0 from algorithm (m/s)	Sensor 1-2	1618.32	1617.22	1621.46
	Sensor 3-4	1624.56	1622.12	1617.87
	Sensor 5-6	1616.44	1619.78	1619.07

Table 5.15: Flexural Lamb wave velocity results for test 1b

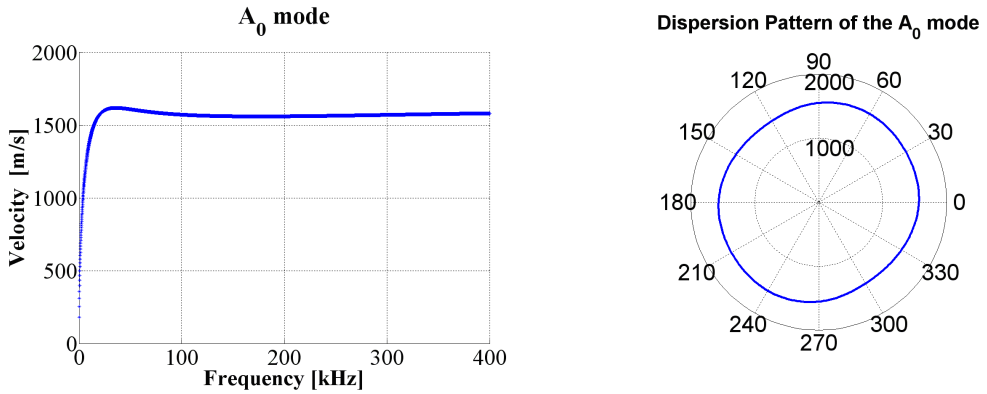

(a) (b)

Figure 5.21: Dispersion curves for the A_0 flexural Lamb mode at $\theta = 0$ (a) and angular-group velocity pattern at 258.77 kHz (b)

5.7.2 Group Velocity Evaluation on CFRP Laminate

Tab. 5.15 provides the values of the flexural group velocities calculated from the algorithm in the CFRP laminate, whilst Fig. 5.21 illustrates the dispersion curves for the Lamb wave A_0 and the angular-dispersion pattern at the instantaneous frequency of 258.77 kHz.

According to the quasi-isotropic nature of the CFRP composite plate, the angular-group velocity pattern was nearly circular (Fig. 5.21b) and the A_0 Lamb mode calculated by the algorithm for any pair of transducers was approximately the same (close to the value of 1620 m/s, i.e. the maximum value for A_0 reported in Fig. 5.21a).

5.7.3 Group Velocity Evaluation on Sandwich Panel

In relation to the previous Section, the group speeds values obtained from the optimization algorithm were compared with those determined by the SFEM method

		Impact S1	Impact S2	Impact S3
A_0 from algorithm (m/s)	Sensor 1-2	2810.08	2768.15	3117.45
	Sensor 3-4	3200.23	3078.86	2987.23
	Sensor 5-6	2840.74	2942.43	3002.29

Table 5.16: Flexural Lamb wave velocity results for test 2b

for the sandwich plate. Tab. 5.16 reports the group velocities calculated from the algorithm, whilst in Fig. 5.22 the dispersion curves for the Lamb wave A_0 and the angular-dispersion pattern at the instantaneous frequency of 348.27 kHz are displayed.

Although the calculated group velocity matched very well with those obtained from the dispersion curves in the CFRP case (Tab. 5.15 and Fig. 5.21), for the sandwich plate the predicted values from the algorithm were slightly different from the reconstructed response provided by the dispersion relations (Tab. 5.16 and Fig. 5.22). Indeed, as it can be seen from Fig. 5.22a, the value of the flexural group velocity at 348.27 kHz is approximately 2800 m/s. This is mainly due to the high attenuations in the sandwich core that are not included in the SFEM model. Therefore, this algorithm proved to be an efficient way to overcome the drawbacks related to the uncertainty of the group estimation provided by the dispersion curves, and the limits of *a-priori* prediction with an accurate model of the structural response of complex structures.

5.8 Summary of the Impact Localization Algorithms

This chapter has reported two *in-situ* SHM methods to locate the impact point and to determine the velocity of guided Lamb waves in plate-like isotropic and composite structures. The proposed methods are based on the differences of the stress waves measured with high SNR by either four or six surface attached PZT transducers. The peak magnitude of the scalogram of the CWT was employed to identify the arrival time (TOA) of the flexural A_0 Lamb mode. Then, the coordinates of the impact location and the group speed were obtained by solving a set

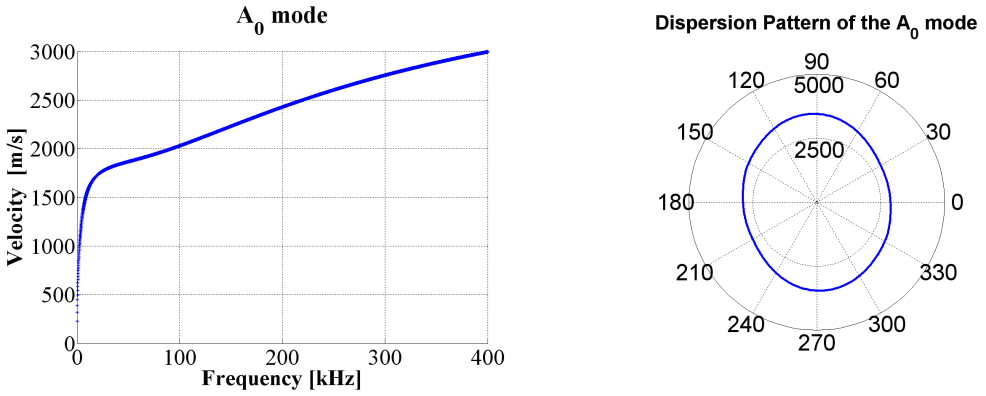

(a) (b)

Figure 5.22: Dispersion curves for the A_0 flexural Lamb mode at $\theta = 0$ (a) and angular-group velocity pattern at 348.27 kHz (b)

of nonlinear equations through a combination of local Newton's iterative method associated to a global unconstrained optimization (line search and polynomial backtracking technique). The experimental results conducted on two aluminium structures, a quasi-isotropic CFRP laminate and a sandwich panel showed that the identification of the impact source location was achieved with satisfactory accuracy. In particular, maximum error in estimation of the impact location was less than 4 mm for the isotropic structures, approximately 3 mm for the quasi-isotropic CFRP panel and nearly 2 mm for the sandwich plate. Moreover, good agreement between the flexural group velocities calculated by the algorithms and the values obtained from the Rayleigh-Lamb relations and a semi-analytical SFEM method was found. Hence, the algorithms described in this chapter are able to satisfy the following requirements:

- they do not require *a-priori* knowledge of the mechanical properties, cross section, as well as lay-up and anisotropic angular-group velocity pattern of the AE in a composite structure
- they exhibit a suitable approach for the time of arrival identification using the CWT
- they provide a flexible trade-off in terms of efficiency and accuracy as they are able to identify the impact source in real-time requiring nearly 1 s

However, a number of issues still need to be addressed:

- the dispersive nature of guided Lamb waves as well as the presence of multiple scattering and mode conversion (*fully diffuse wave field*) in complex structures may alter the resulting signal, leading to a wrong estimation of TOA
- only the information from the coherent part of the wave field arriving first to the sensors (*ballistic wave*) is used, regardless of the contribution of multiple scattering and reflection from the boundaries (know from seismology as *coda*)

Chapter 6

Imaging of the Impact Location in Complex Anisotropic Structures

This chapter presents an imaging method for the localization of the impact point in complex anisotropic structures with diffuse field conditions, using only one passive transducer. The proposed technique is based on the *reciprocal time reversal* approach (*inverse filtering*) applied to a number of waveforms stored into a database containing the experimental Green's function of the structure. The present method allows achieving the optimal focalization of the impact source in the time and spatial domain as it overcomes the drawbacks of other ultrasonic techniques. This is mainly due to the dispersive nature of guided Lamb waves as well as the presence of multiple scattering and mode conversion that can degrade the quality of the focusing, causing poor localization. Conversely, according to Sec. 4.4 the reverberation of a diffuse wave field in a complex medium improve the spatial resolution of the focusing. Indeed, the presence of linear scatterers (stiffeners, holes, voids, etc ...) within the medium allows the evanescent waves to propagate in the far field, where the TRM is located. These modes, carrying the information of the impact source, can participate to the focusing process (*kaleidoscopic effect*, see Fig. 4.3). Compared to a classical time reversal (TR) approach, the optimal re-focusing of the back propagated wave field at the impact

point is accomplished through a "virtual" imaging process, which does not require any iterative algorithms and a priori knowledge of the mechanical properties and the anisotropic group speed. The robustness of the inverse filtering technique is experimentally demonstrated on a dissipative stiffened composite panel and the source position can be retrieved with a high level of accuracy in any position of the structure.
The layout of the chapter is as follow: in Sec. 6.1, the imaging method for the localization of the impact source is theoretically presented with a classical time reversal process and the inverse filtering technique. Sec. 6.2 reports the experimental set-up whilst Sec. 6.4 compares the robustness and focus quality of both methods, showing the imaging results for two different impact points. Then, the summary of the chapter is presented.

6.1 One-Channel Impact Localization Method

This imaging method, in its physical principle, is closer to a recent work presented by Sabra et al. (Sabra *et al.* [2008]) consisting in the estimation of the local Green's function of aeronautical structures with a *Correlation of a Diffuse Field* (CDF) technique. However, in that work, all the information contained in the reverberant acoustic wave field was recorded using two passive sensors and the experimental impulse response was compared to theoretical predictions. Here, the CDF method is combined with the advantages of a reciprocal time reversal process. The proposed technique is aimed to overcome the limitations of most impact detection methods and to obtain the optimal focusing of the source in real-time, by using only one passive sensor placed on a generic point of the structure. The methodology was divided in two steps. In the first step, the impulsive responses of the structure were acquired and stored into a computer. Then, exploiting the benefits of multimodal conversion and scattering effects, a "virtual" reciprocal time reversal experiment was carried out. Hence, in order to obtain the optimal re-focusing at the impact source, the transfer matrix of the structure $\mathbf{H}(\omega)$ is first introduced, and then both time reversal and inverse filtering imaging techniques are analysed.

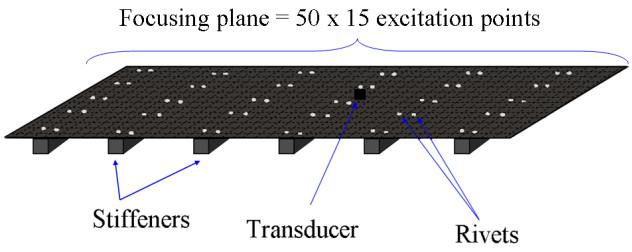

Figure 6.1: Experimental set-up

6.1.1 The Structural Transfer Matrix $\mathbf{H}(\omega)$

In a first step, the surface structure (*focusing plane*) was entirely divided in $M = 50 \times 15$ "excitation points" distributed along a grid at interval of 2 cm. At each point, the acoustic emission was generated by impact loads (Fig. 6.1).

Due to linearity, according to Eq. (4.33), the acoustic field measured by the receiver transducer from the mth excitation point is:

$$f(t) = \sum_{m=1}^{M} h_m(t) \otimes e_m(t) = \int_{-\infty}^{+\infty} \sum_{m=1}^{M} h_m(\tau) \otimes e_m(t-\tau) d\tau \tag{6.1}$$

where, as reported in Sec. 4.2.2, the symbol "$\otimes$" represents a temporal convolution and $h_m(t)$ $(1 \leq m \leq M)$ is the linear propagator operator defining the Green's function measured by the sensor. This term includes all the propagation effects through the medium from the mth excitation point to the receiver (including its acoustic-electric response). $e_m(t)$ is the input signal sent by the mth source on the focusing plane and $f(t)$ is the output signal measured by the transducer at each instant in time. In the frequency domain, Eq. (6.1) is:

$$\hat{f}(\omega) = \sum_{m=1}^{M} \hat{h}_m(\omega)\hat{e}_m(\omega) \tag{6.2}$$

which can be written in matrix form as:

$$\underbrace{F(\omega)}_{1\times 1} = \underbrace{\mathbf{H}_m(\omega)}_{1\times M}\underbrace{\mathbf{E}_m(\omega)}_{M\times 1} \tag{6.3}$$

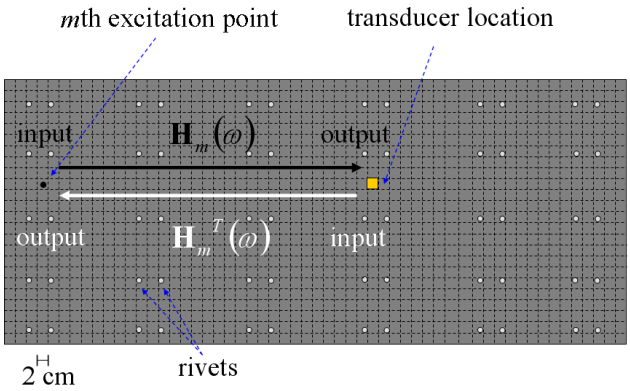

Figure 6.2: Schematic outline of the reciprocity condition of the transfer matrix $\mathbf{H}_m(\omega)$

where the matrix $\mathbf{H}_m(\omega)$ is the transfer matrix of the system (Fourier transform of the Green's function) and represents the amplitude of the ith guided Lamb mode associated to the ith eigenfrequency. For the spatial reciprocity condition, the transpose of $\mathbf{H}_m$ ($\mathbf{H}_m^T$) corresponds to the propagation between the transducer and the excitation points (Fig. 6.2):

$$\mathbf{E}_m(\omega) = \mathbf{H}_m^T(\omega)F(\omega) \tag{6.4}$$

Hence, the M signals representing a library of impulse responses $\mathbf{H}_m(\omega)$ of the structure were recorded by the transducer and stored into the computer memory.

6.1.2 Time Reversal Focusing Approach

The second step consisted in recognition of the optimal refocusing procedure at the source location. The basic idea was to time reverse not only the Green's function associated to the AE source, but also to neighbouring points ("excitation points"). Thereby, a new impact was applied in one of the points (of unknown location) of the focusing plane and its impulse response was measured by the sensor. In accordance with Sec. 4.4, TR behaves as a spatio-temporal matched filter that maximizes the ratio between the amplitude of the output signal (waveform acquired) and the square root of the input energy (impulse applied). Hence, assuming that the impact source in the second step is located at m_0, the input

waveform $e_{m0}(t)$ from the mth excitation point can be mathematically approximated to a temporal delta function $\delta(t)$ only when $m = m_0$. In the frequency domain, the emitted signal is $\mathbf{E}_{m0}(\omega) = \{0, \ldots, 0, 1, 0, \ldots, 0\}^T$. According to Eq. (6.3), the wave field received by the transducer is:

$$F_{m0}(\omega) = \mathbf{H}_{m0}(\omega)\mathbf{E}_{m0}(\omega) \tag{6.5}$$

and the time reversal operation of the Green's function $[h_{m0}(-t)]$ in the time domain is equivalent to taking its complex conjugate in the Fourier domain. Hence, time reversing the spectrum of the transducer output, we have:

$$F^*_{m0}(\omega) = \mathbf{H}^*_{m0}(\omega)\mathbf{E}^*_{m0}(\omega) = \mathbf{H}^*_{m0}(\omega)\mathbf{E}_{m0}(\omega) \tag{6.6}$$

where the asterisk denotes complex conjugate and $\mathbf{E}_{m0}(\omega)$ is real. Combining Eqs. (6.4) and (6.6), the back-propagated signal at the source is:

$$\mathbf{E}_{TR}(\omega) = \mathbf{H}^T_m(\omega)F^*_{m0}(\omega) = \mathbf{H}^T_m(\omega)\mathbf{H}^*_{m0}(\omega)\mathbf{E}_{m0}(\omega) \tag{6.7}$$

and $\mathbf{H}^T_m(\omega)\mathbf{H}^*_{m0}(\omega)$ is called the *TR operator*. Since Eq. (6.7) has a maximum at the focus point, the information associated to the AE source location can be extracted from a "virtual" TR experiment. Fig. 6.3 illustrates the procedure for obtaining the imaging focusing with a TR analysis.

6.1.3 Reciprocal Time Reversal Focusing Approach

As reported in Sec. 4.1, the spherical symmetry of TR holds only in the case of lossless media. Indeed, from the study of the elastodynamics wave equation [Eq. (4.3)], the TR invariance is due to the presence of the even order (2^{nd} order) time partial derivative operator. This condition cannot be satisfied in dissipative media, as the wave equation presents a time partial derivative operator of the first order (Tanter *et al.* [1998]). Therefore, although spatial reciprocity and time reversal invariance hold in diffuse wave fields or anisotropic media, such conditions cannot not satisfied because of the following reasons:

- Limited transducer bandwidth (the effect is to broaden the TR focus)

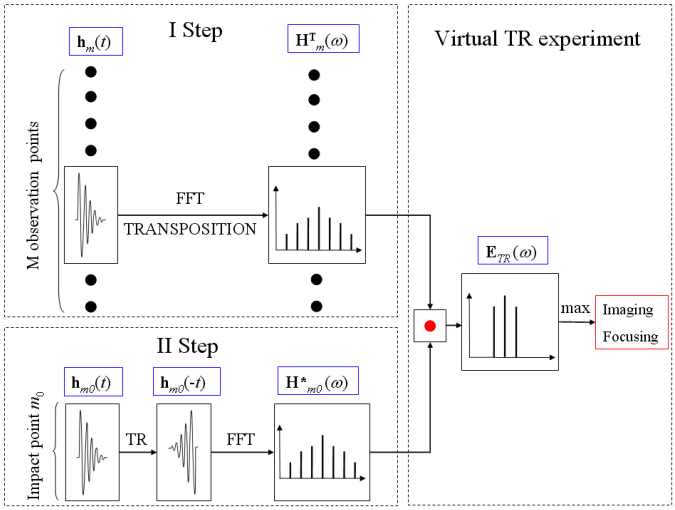

Figure 6.3: Architecture of the time reversal imaging process

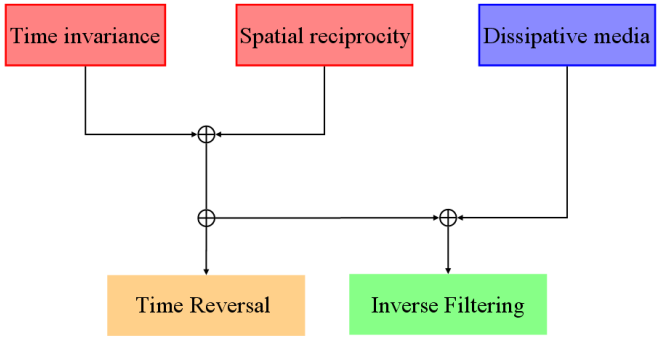

Figure 6.4: Focusing conditions for TR and IF methods

- Shock waves formation (energy loss which makes the elastic waves no longer reversible) (Cunningham *et al.* [2001])
- Absorptions and nonlinear attenuation with the wave amplitude

These aberrations generate phase and amplitude distortions of the propagating wave front, and the behaviour of a TRM becomes very difficult to be predicted. However, Tanter et al. (Tanter *et al.* [2000]) showed that the *reciprocal time reversal* or *Inverse Filtering* (IF) approach allows recovering the optimal focusing, even in dissipative media (Fig. 6.4).

The IF approach is based on the inversion of the transfer matrix $\mathbf{H}(\omega)$. Compared to a classical time reversal experiment, the inverse filtering technique is able to increase the contrast C, i.e. the ratio of the averaged energy of the refocused signal at the time t=0 and the averaged energy of the recompressed signal at all other times (Derode *et al.* [1999]):

$$C = \frac{\langle e_X^2(t=0)\rangle}{\langle e_X^2(t\neq 0)\rangle} \tag{6.8}$$

where $e_X(t)$ is the back-propagated field at the impact source (in the time domain) and the subscript X indicates either TR or IF operation. As the TR experiments, a new impact was applied in m_0 and its experimental Green's function was recorded by the transducer. In the general case of M excitation points and an array of N receivers ($N > 1$), Tanter et al. (Tanter *et al.* [2000]) showed that the inversion of the transfer matrix $\mathbf{H}$ could be performed through a *Singular Value Decomposition* (SVD) in order to avoid singularity problems (propagator operator ill conditioned). In our case, the field distribution $F_{m0}(\omega)$ of a single receiver, when the acoustic emission propagation is generated by an impact $\mathbf{E}_{m0}(\omega)$, is obtained multiplying both members of Eq. (6.4) for the complex conjugate of $\mathbf{H}_{m0}(\omega)$ as follows:

$$\mathbf{H}_{m0}^*(\omega)\mathbf{E}_{m0}(\omega) = \mathbf{H}_{m0}^*(\omega)\mathbf{H}_{m0}^T(\omega)F_{m0}(\omega) = \|\mathbf{H}(\omega)\|^2 F_{m0}(\omega) \tag{6.9}$$

Hence, we obtain:

$$F_{m0}(\omega) = \tilde{\mathbf{H}}(\omega)\mathbf{E}_{m0}(\omega) \tag{6.10}$$

where $\tilde{\mathbf{H}}(\omega) = \mathbf{H}_{m0}^*(\omega)/\|\mathbf{H}(\omega)\|^2$ is the inversion of the propagation operator and $\|\mathbf{H}(\omega)\|^2$ is the squared norm of the vector $\mathbf{H}_{m0}^T(\omega)$ which represents the square of the modal energy of the system. Thereby, the optimal focusing with the reciprocal time reversal method is:

$$\mathbf{E}_{IF}(\omega) = \mathbf{H}_m^T(\omega)F_{m0}(\omega) = \mathbf{H}_m^T(\omega)\tilde{\mathbf{H}}(\omega)\mathbf{E}_{m0}(\omega) \tag{6.11}$$

and the operator $\mathbf{H}_m^T(\omega)\tilde{\mathbf{H}}(\omega)$ is referred to as the *IF operator*. As Eq. (6.7), also Eq. (6.11) has a maximum at the focus point, i.e. when $m = m_0$. Therefore, the

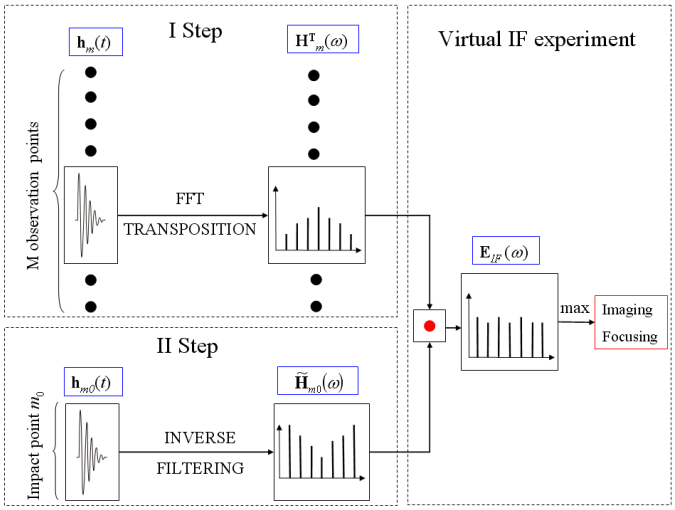

Figure 6.5: Architecture of the inverse filtering imaging process

imaging focusing of the impact location can be obtained through a "virtual" IF experiment (Fig. 6.5).

6.2 Experimental Set-up

The experiments were carried out on a reverberant carbon-fibre composite plate (100 cm × 30 cm × 3 mm) reinforced with six vertical stiffeners and connected with rivets (7.9 mm of diameter) (Fig. 6.6). For the library of signal needed to implement the technique, the impacts were applied to 750 excitation points spaced 2 cm apart using a hand-held modal hammer. The experimental Green's function from each excitation point was acquired using an acoustic emission sensor instrumented with an oscilloscope (Picoscope 4224) with a sampling rate of 25 MHz. The passive sensor employed was the same acoustic emission transducer used for the experiments reported in Sec. 5.5, with a central frequency of 300 kHz. The time histories of the signal received by the sensor were stored on a computer and processed using a Matlab software code implemented by the authors. In accordance with the AE sensors frequency bandwidth and Nyquist theorem, due to the long reverberation present in the signal, a 100 ms duration time window was chosen (Fig. 6.7).

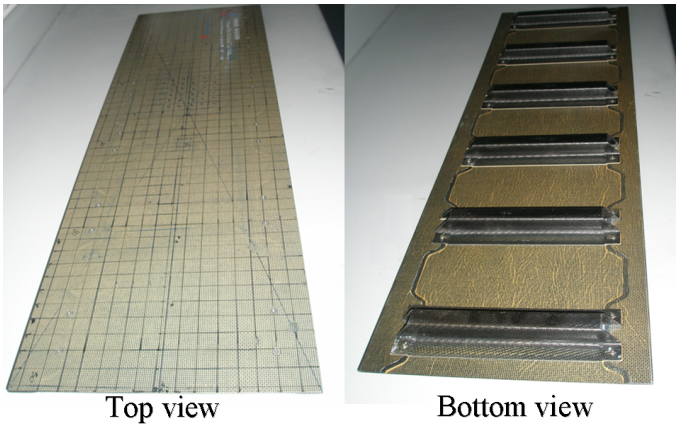

Figure 6.6: Top and bottom view of the stiffened carbon-fibre composite panel used in the experiments

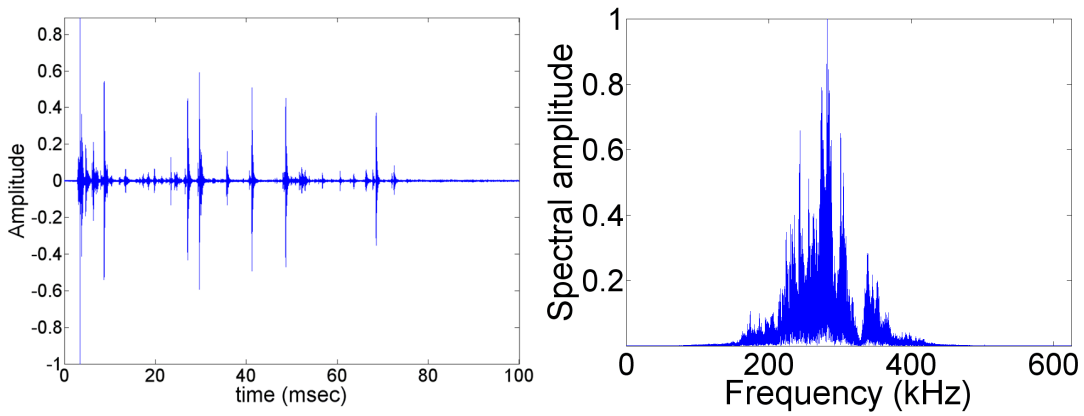

(a) (b)

Figure 6.7: Normalized time history (a) of one the focusing point and its frequency content (b). In figure (a), a reverberant impulse response is clearly visible

	X-coordinate (cm)	Y-coordinate (cm)
Sensor position (case I1)	60	16
Sensor position (case I2)	24	14
Impact I1	40	10
Impact I2	80	26

Table 6.1: Sensors and impact coordinated in case I1 and I2

Sensor locations and impact source coordinates are reported in Tab. 6.1 for two different cases (referred as impacts I1 and I2).

6.3 Imaging Localization Results

Since the imaging method is based on a "virtual" focusing process, *spatial resolution* and localization precision (*accuracy*) are highly related. In particular, accuracy is defined as the degree of closeness of the maximum value of the normalized correlation coefficients obtained for the mth excitation point with respect to the true impact point (located in m_0). It can be expressed (in percentage) by the ratio between the localization error ξ_m given by the formula $\xi_m = (x_m - x_{m0})^2 + (y_m - y_{m0})^2$ and the total length of the plate, where x_m and y_m are the coordinated of the mth excitation point and x_{m0} and y_{m0} are the coordinates of the true impact source. On the other hand, resolution is the system's ability to distinguish neighbouring points and it can be defined as the -3 dB width of the normalized correlation coefficients patterns at the focus point (Ing *et al.* [2005]). The imaging results are illustrated in Fig. 6.8 and 6.9 for the two different cases I1 and I2, showing a comparison of focalization between the IF method and TR analysis. According to Sec. 6.1, the refocusing wave fields at the source location are represented by a normalized gray-scale 2D map and the maxima of $\mathbf{E}_{TR}(\omega)$ and $\mathbf{E}_{IF}(\omega)$ [Eq. (6.7) and (6.11)] are deduced from the values nearest to 1, with a computational time lower than 1 sec.

From the above figures, the TR experiments provided a maximum value of the normalized correlation coefficient equal to 1, even in points close to the true impact source (see the points at x = 38 cm and y = 10 cm for case I1 in Fig. 6.8b and x = 80 cm and y = 28 cm for case I2 in Fig. 6.9b). Such ambiguities might be

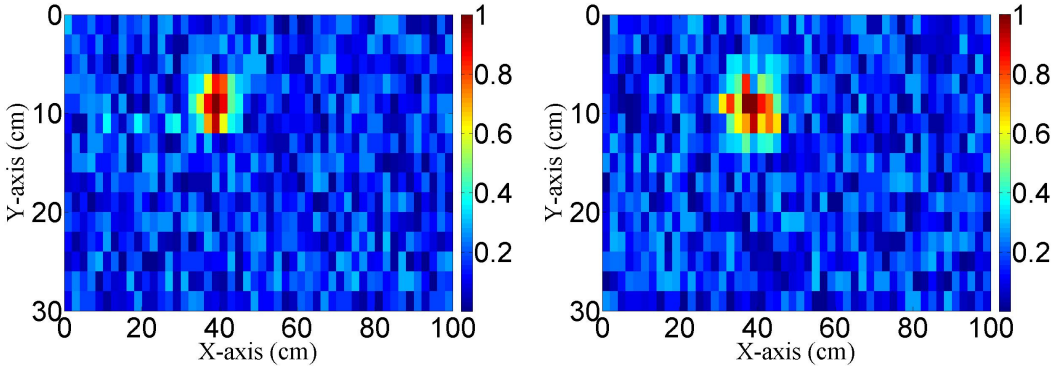

Figure 6.8: 2D map of the maxima normalized correlation coefficients with the IF approach (a) and the TR analysis (b) for the case I1

due to the effects of distortion (nonlinear attenuation) in the complex dissipative structure. Conversely, in the IF technique an optimal focusing with a 0% error on the estimation of the impact location was achieved. This can be explained as follows. In the TR process [Eq. (6.7)] only the flexural Lamb modes with higher energy are used for the refocusing process, whilst the modes with lower energy are vanished (see Fig. 6.3). On the other hand, in the IF approach, contrast is enhanced through the introduction of the modes weighted by the inverse of the energy at each eigenfrequency [Eq. (6.11)]. Indeed, the modes with weak amplitude are re-emitted at higher energy, whilst the modes with bigger amplitude are back propagated at lower energy (Fig. 6.5). Hence, the reciprocal TR technique can be assumed as a "whitening process", wherein the number of modes (and thus the quantity of information) employed for the back propagation at the focal point can be increased. This effect is fundamental to understand the significant improvement of the contrast with the IF technique compared with the TR method in reverberant dissipative media. Indeed, assuming the linear propagator operator $h_m(t)$ for the mth excitation point as a non-stationary Gaussian signal with zero mean and variance $\sigma^2(t)$, it can be defined for a dissipative medium

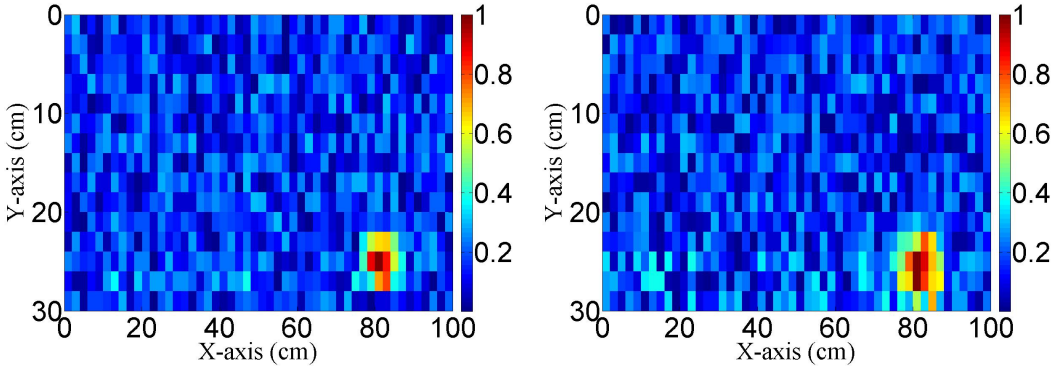

(a) (b)

Figure 6.9: 2D map of the maxima normalized correlation coefficients with the IF approach (a) and the TR analysis (b) for the case I2

with diffuse field conditions as (Quieffin [2004]):

$$h_m(t) = \sum_{i=0}^{\infty} \alpha_i \sin(\omega_i t) e^{-t/\tau_a} \tag{6.12}$$

where α_i are the amplitudes of the ith Lamb mode contained in the wave field associated to the ith eigenfrequency ω_i, and τ_a represents the decay time of the elastic field which depends on the scattering properties and the elastic attenuation of the structure (Evans & Cawley [1999]). Under the hypothesis of diffusive wave field, substituting expression (6.12) in the inverse Fourier transform of Eq. (6.7), according to the analytical formulation obtained by Quieffin (Quieffin [2004]), the contrast defined in Eq. (6.8) becomes:

$$C = \frac{8\pi^{3/2} Bn}{a} \tag{6.13}$$

where B is the frequency bandwidth of the acoustic emission transducers, n is the modal density of the structure, a is the flatness factor, i.e. the ratio of mean fourth power of a mode amplitude to the square of the mean square. The product Bn represents the number of modes contained in the retro-focused signal, whilst a for dissipative media varies between 2 and 3 (Lobkis & Weaver [2000]). Since the effect of IF is to increase the number of modes for the back propagation at

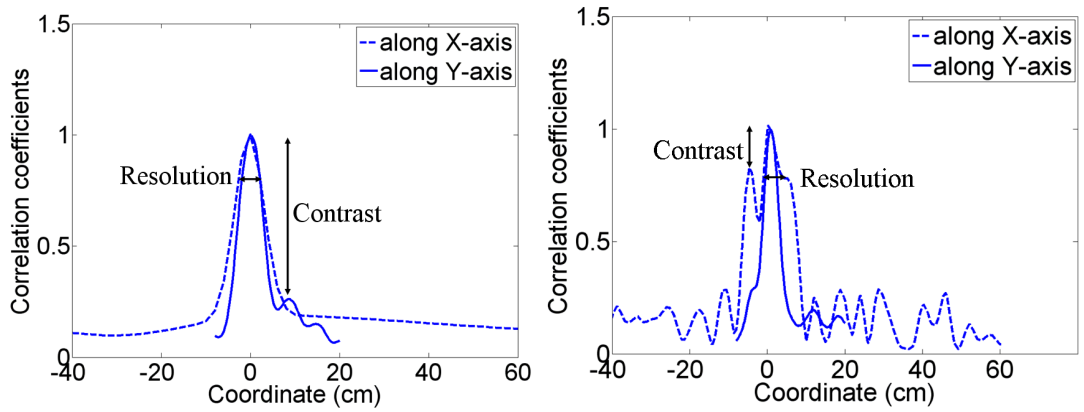

Figure 6.10: Normalized correlation coefficients patterns along the X and Y-axis with the maximum at the focus point with IF method (a) and TR approach (b) for case I1

the focal point (a remains the same for TR and IF), according to Eq. (6.13), with such method the contrast can be significantly enhanced (Bou Matar *et al.* [2009]). Therefore, from the normalized correlation coefficients patterns along the X and Y-axis in Fig. 6.10 and 6.11 two main conclusions were drawn:

- since the maximum error reported for TR and IF experiments was less than 3% and 0%, respectively, in accordance with the benefits of a diffuse wave field, a high spatial resolution was obtained and the number of sensors used did not need to be increased.

- the real effect of IF method was to improve the accuracy of the impact location (compensation of the distortions effects in a dissipative medium in combination with the benefits of a diffuse wave field) and to enhance the contrast and thus the focusing efficiency (accuracy) up to 0% localization error even using one passive transducer.

Hence, compared to other ultrasonic impact localization systems, this method presents the great advantage that it does not require any iterative algorithms as well as a priori knowledge of the TOA, mechanical properties, lay-up and anisotropic angular-group velocity pattern of the medium. In addition, since

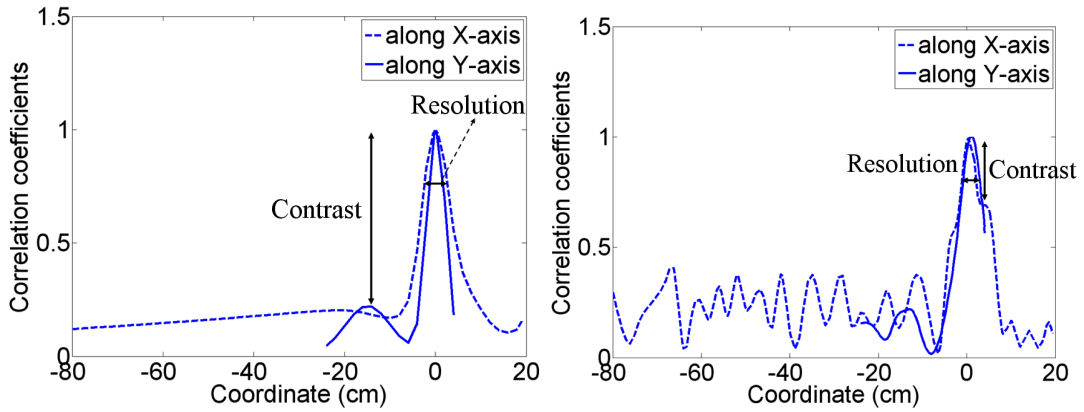

Figure 6.11: Normalized correlation coefficients patterns along the X and Y-axis with the maximum at the focus point with IF method (a) and TR approach (b) for case I2

only one passive transducer is needed for the imaging of the impact source, an effective decrease of the number of sensors, resulting in significant costs and weights savings, can be accomplished. Nevertheless, during the experiments it was observed that a decrease of the number of observation points led to an increase of the maximum error in retrieving the impact location, with lower values of $\max \mathbf{E}_{TR}(\omega)$ compared to the previous case (Fig. 6.12). In particular, assuming 200 observation points the location error was found nearly 10% for impact I1 (Fig. 6.12a) and approximately 12% for impact I2 (Fig. 6.12b).

6.4 Summary of the Imaging Localization Method

In this chapter, an *in-situ* imaging method able to detect in real-time the impact source in dissipative complex composite structures with diffuse field conditions is presented. This technique based on the reciprocal time reversal (inverse filtering) approach, is directly applied to the experimental impulse responses of the structure recorded by only one passive sensor and stored into a database. The proposed method allows achieving the optimal focalization of the acoustic emission source as it is able to compensate the distortion effects in a dissipative medium. Moreover, exploiting the benefits of a diffuse wave field, a high refocusing quality, with

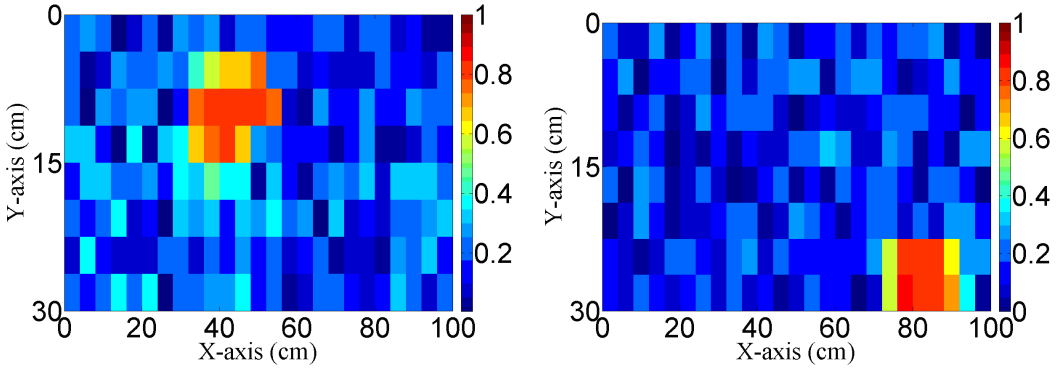

Figure 6.12: 2D map of the optimal refocusing for impact I1 (a) and I2 (b) with 200 observation points

only one sensor was accomplished. Compared to a simple time reversal process, the robustness of this approach was experimentally demonstrated on a stiffened composite plate and the results showed that the IF technique provides an optimal focusing with a 0% error on the estimation of the impact location. Moreover, for the imaging process, no iterative algorithms as well as a priori knowledge of the mechanical properties, lay-up, thickness and the dispersive and anisotropic group velocity pattern of the medium are required.

Chapter 7

Imaging Non-Classical Elastic Nonlinearities in Complex Anisotropic Structures

Damages in complex composite materials such as matrix cracking, fibre debonding, delamination, etc., increase their heterogeneity and the complexity of the structure in terms of alteration between grainy regions and binding medium (see Sec. 2.2.1). Hence, damaged composite laminates may give raise to non-classical nonlinearity wave effects generated by material hysteretic behaviour, which is enhanced with the increase of the damaged state. Indeed, such media display nonlinear mesoscopic elasticity that appears to be much like that in rock or concrete (Johnson [2006] and Meo & Zumpano [2005]). Thus, for damaged complex materials such as sandwich structures, *third harmonic* is the lowest harmonic with the larger energy content predicted by Eq. (2.7), and can be chosen to assess the damage. In the last few years, nonlinear elastic wave spectroscopy (NEWS) and Phase Inversion (PI) methods have been combined with time reversal technique in order to focus acoustic energy and illuminate secondary sources (damages) into a medium (see Sec. 2.4.1.1). In particular, PI technique takes into account only the even nonlinear harmonic part (second order nonlinearity), regardless of the linear and odd nonlinear harmonic contribution. Hence, this approach does not work satisfactorily to extract the third order nonlinear signature in damaged media

that manifest non-classical nonlinear phenomena. However, PI can be considered as a particular case of a general paradigm based on the invariant properties of nonlinear systems, called *phase symmetry analysis* (PSA).

This chapter presents an imaging method aimed to locate the third order nonlinearity in damaged complex anisotropic structures with diffuse filed conditions, using only two sensors in pitch-catch mode. The proposed technique is based on a combination of reciprocal TR and phase symmetry analysis with frequency modulation (FM) excitation, in order to obtain the optimal refocusing on the nonlinear scatterer due to the presence of cracks and delamination. In particular, PSA was employed to characterize the third order nonlinear response of a damaged reverberant anisotropic medium with hysteretic behaviour, by exploiting its invariant properties with the phase angle ϕ of the chirp excitation signals. In other words, this method allows determining the phase angle of the input waveforms, in order to discern only the odd nonlinear harmonic part from the received output. Then, a "virtual" Inverse Filtering (IF) or reciprocal TR approach was used as it allows recovering the optimal focusing at the nonlinear source, even in dissipative media (see Sec. 6.1.3). Indeed, nonlinear attenuation with the wave amplitude breaks the time reversal symmetry, generating phase and amplitude distortions of the propagating wave front. Nevertheless, IF technique was used to "illuminate" the defect taking advantage of multiple linear scattering as mode conversion and boundaries reflections. The robustness of this methodology was experimentally demonstrated on a damaged sandwich panel, and the nonlinear source, induced by low-velocity impact loading, was retrieved with a high level of accuracy.

The layout of the chapter is as follows: in Sec. 7.1, the imaging technique is theoretically illustrated by introducing phase symmetry analysis and the nonlinear inverse filtering process. Sec. 7.2 presents the experimental set-up whilst Sec. 7.3 shows the results of the nonlinear imaging method. Then, a summary of the chapter is reported.

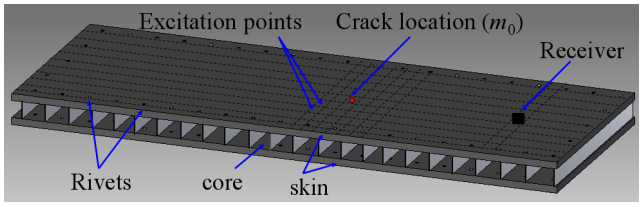

Figure 7.1: Representation of the sandwich structure with diffuse field conditions

7.1 Nonlinear Imaging Method

Symmetry (or invariance) properties of physical phenomena have been widely used for the analysis of nonlinear systems. For instance, the symmetries associated to the infinitesimals of Lie groups were employed to determine the motion of particles propagating in a medium with non-classical nonlinearity (Dos Santos *et al.* [2004]). In addition, the invariance properties of Korteweg-de Vries stationary solutions (solitary waves) were used as a signature of the dispersive and nonlinear features of the structure (Daraio [2009]). Similarly to Sec. 6.1.3, the nonlinear imaging process was divided into two steps. In the first step, the third order nonlinear transfer matrices of the structure obtained after PSA process were acquired and stored into the computer memory. Then, exploiting the benefits of multimodal conversion and boundary reflections, a "virtual" re-focusing procedure of the recorded signals on the nonlinear source was performed using IF method.

7.1.1 Extraction of Third Order Nonlinear Impulse Response

In the first step, an impact loading was applied to a sandwich composite structure in order to barely indent the medium and to generate delamination localized at the impact site, almost invisible from the top surface (BVID). Then, the damaged zone surrounding the impact point focusing area was divided in $M = 7 \times 6$ "excitation points" distributed along a grid at interval of 2 cm (Fig. 7.1). The rest of the sample remains undamaged, so that the nonlinear signature is only present in the region around the defect. In each of the m ($1 \leq m \leq M$) excitation

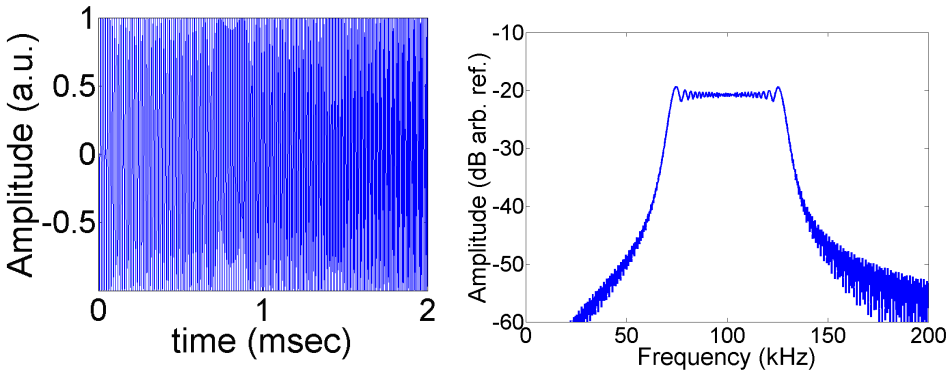

(a) (b)

Figure 7.2: Signal emitted from one of the M excitation points (a) and its spectrum (b)

points a longer duration frequency modulated (FM) signal with wide frequency bandwidth was transmitted. The general chirp signal can be expressed in complex notation as (Misaridis & Jensen [2005a]):

$$x(t) = c(t)e^{i\phi} = e^{i\left[2\pi\left(f_0 t + \frac{\mu}{2}t^2\right)+\phi\right]} \quad -\frac{T}{2} \leq t \leq \frac{T}{2} \tag{7.1}$$

where f_0 is the central frequency, T is the signal duration (uncompressed pulse width), ϕ is the phase angle, $\mu = B/T$ is the FM slope and B is the total bandwidth that is swept, i.e. the difference between the highest and lowest frequencies within the uncompressed pulse. In our case B= 70-130 kHz and T=2 ms. Since linear chirp signal has a quadratic phase modulation function, the instantaneous frequency is linear and given by:

$$f_i = \frac{1}{2\pi}\frac{d\left[2\pi\left(f_0 t + \frac{\mu}{2}t^2\right)+\phi\right]}{dt} = f_0 + 2\mu t \tag{7.2}$$

The expression above represents the spectral band of a FM signal in which the energy is concentrated at the time t. If the the time-bandwidth product TB is sufficiently large ($TB > 15$), the signal's spectrum is assumed to be approximately a rectangular distribution (Fig. 7.2). Chirp signal was chosen in order to improve the signal-to-noise ratio (SNR), the penetration depth and to keep the sidelobes below the limiting level of the typical dynamical range of an ultra-

sound image (Misaridis & Jensen [2005a]). Then, a *mismatched filter* (weighted pulse compression) was performed as it allows converting the FM transmitted signal into a band-limited pulse of greater peak power. Indeed, according to App. C, a weighted pulse compression consists of a correlation between the received and the transmitted chirp signal multiplied by a window function (Blackman or Dolph-Chebyshev). The mismatched filter is expressed by the following equation:

$$e_m(t) = e^{i\phi}\frac{1}{2\pi}\int_{-\infty}^{+\infty}\hat{c}(\omega)\hat{h}_{MF}(\omega)e^{i\omega t}d\omega \cong \delta(t)e^{i\phi} \tag{7.3}$$

wherein $e_m(t)$ is the new input signal to be time reversed from each excitation point, $\hat{c}(\omega)$ is the Fourier transform of the transmitted FM input function with null phase angle, $\hat{h}_{MF}(\omega) = \hat{w}(\omega)\hat{c}^*(\omega)$, where $\hat{w}(\omega)$ is the Fourier transform of the window function and the asterisk corresponds to a complex conjugate operation. Assuming that the nonlinear behaviour of the medium is described through a third order nonlinear system, the output $f(t)$ received by the sensor placed far from the focusing area can be expressed through a *Volterra functional series* as follows (Bussang *et al.* [1974]) (Fig. 7.3):

$$\begin{aligned} f(t) &= \sum_{n=1}^{3} f_n(t) = f_1(t) + f_2(t) + f_3(t) \\ &= \int_{-\infty}^{+\infty}\sum_{m=1}^{M} h_m^{(1)}(\tau_1)e_m(t-\tau_1)d\tau_1 \\ &+ \beta\int_{-\infty}^{+\infty}d\tau_1\int_{-\infty}^{+\infty}\sum_{m=1}^{M} h_m^{(2)}(\tau_1,\tau_2)e_m(t-\tau_1)e_m(t-\tau_2)d\tau_2 \\ &+ \gamma\int_{-\infty}^{+\infty}d\tau_1\int_{-\infty}^{+\infty}d\tau_2\int_{-\infty}^{+\infty}\sum_{m=1}^{M} h_m^{(3)}(\tau_1,\tau_2,\tau_3)e_m(t-\tau_1)e_m(t-\tau_2)e_m(t-\tau_2)d\tau_3 \end{aligned} \tag{7.4}$$

where $e_m(t)$ is the column vector of the input signal sent by the mth excitation point, $f_1(t)$, $f_2(t)$, $f_3(t)$, are the system partial responses of the linear, second, and third order, respectively, and β and γ are the second and third or-

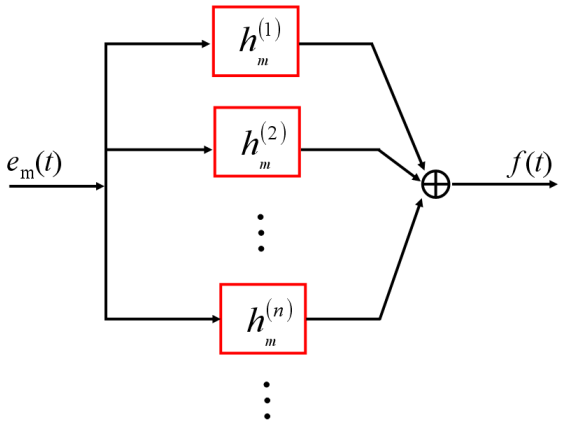

Figure 7.3: Schematic representation of a Volterra series model

der nonlinear coefficients. The nth order kernel of Eq. (7.4), $h_m^{(n)}(\tau_1, \ldots, \tau_n)$, is called the *nonlinear impulse response* of order n. This term includes all the nonlinear propagation effects through the medium and the coda from the mth excitation point to the receiver (Kazakov *et al.* [2002]). Its Fourier transform is called the *nonlinear transfer function* of order n (the sum term is omitted for clarity reasons):

$$\hat{h}_m^{(n)}(\omega_1, \ldots, \omega_n) = \int_{-\infty}^{+\infty} \cdots \int_{-\infty}^{+\infty} h_m^{(n)}(\tau_1, \ldots, \tau_n) e^{-[i(\omega_1\tau_1 + \cdots + \omega_n\tau_n)]} d\tau_1 \cdots d\tau_n \tag{7.5}$$

Since $h_m^{(n)}(\tau_1, \ldots, \tau_n)$ is a symmetric function of the arguments $(\tau_1, \ldots, \tau_n)$, it follows that $\hat{h}_m^{(n)}(\omega_1, \ldots, \omega_n)$ is symmetric for $(\omega_1, \ldots, \omega_n)$. In addition, from Eq. (7.5), it can be noted that the usual properties of spectral conjugation still hold:

$$\hat{h}_m^{(n)*}(\omega_1, \ldots, \omega_n) = \hat{h}_m^{(n)}(-\omega_1, \ldots, -\omega_n) \tag{7.6}$$

However, as the nonlinear impulse response is a function of n variables, the nonlinear system can be simplified by replacing the kernel $h_m^{(n)}(\tau_1, \ldots, \tau_n)$ with its symmetric representation [*Wiener model* (Greblicki [1997])]:

$$h_m^{(n)}(\tau_1, \ldots, \tau_n) = \prod_n h_m'^{(n)}(\tau) \tag{7.7}$$

where $h_m'^{(n)}(\tau)$ is called the sub-kernel of order n. Substituting Eq. (7.7) into the second and third order nonlinear impulse responses of Eq. (7.4), we have:

$$\begin{aligned} h_m^{(2)}(\tau_1,\tau_2) &= h_m'^{(2)}(\tau_1)h_m'^{(2)}(\tau_2) \\ h_m^{(3)}(\tau_1,\tau_2,\tau_3) &= h_m'^{(3)}(\tau_1)h_m'^{(3)}(\tau_2)h_m'^{(3)}(\tau_3) \end{aligned} \tag{7.8}$$

Hence, assuming that the defect is located at m_0, solving the multiple integrals of Eq. (7.4), the following terms are obtained:
Linear term:

$$f_1(t) = \int_{-\infty}^{+\infty} h_m^{(1)}(\tau_1)e_m(t-\tau_1)d\tau_1 = e^{i\phi}\int_{-\infty}^{+\infty} h_m^{(1)}(\tau_1)\delta_{m0}(t-\tau_1)d\tau_1 = h_m^{(1)}(t)e^{i\phi} \tag{7.9}$$

where $h_m^{(1)}(\tau_1)$ corresponds to the linear impulse response (Green's function) of the structure and δ_{m0} is a temporal and spatial delta function distribution that is null everywhere, except for $m = m_0$.
Second order term:

$$\begin{aligned} f_2(t) &= \beta \int_{-\infty}^{+\infty} d\tau_1 \int_{-\infty}^{+\infty} h_m^{(2)}(\tau_1,\tau_2)e_m(t-\tau_1)e_m(t-\tau_2)d\tau_2 \\ &= \beta \int_{-\infty}^{+\infty} d\tau_1 \int_{-\infty}^{+\infty} h_m'^{(2)}(\tau_1)h_m'^{(2)}(\tau_2)e_m(t-\tau_1)e_m(t-\tau_2)d\tau_2 \\ &= \beta e^{i2\phi}\int_{-\infty}^{+\infty} h_m'^{(2)}(\tau_1)\delta_{m0}(t-\tau_1)d\tau_1 \int_{-\infty}^{+\infty} h_m'^{(2)}(\tau_2)\delta_{m0}(t-\tau_2)d\tau_2 \\ &= \beta\left[h_m'^{(2)}(t)\right]^2 e^{i2\phi} = \beta h_m^{(2)}(t)e^{i2\phi} \end{aligned} \tag{7.10}$$

Third order term:

$$\begin{aligned} f_3(t) &= \gamma \int_{-\infty}^{+\infty} d\tau_1 \int_{-\infty}^{+\infty} d\tau_2 \int_{-\infty}^{+\infty} h_m^{(3)}(\tau_1,\tau_2,\tau_3)e_m(t-\tau_1)e_m(t-\tau_2)e_m(t-\tau_3)d\tau_3 \\ &= \gamma\left[h_m'^{(3)}(t)\right]^3 e^{i3\phi} = \gamma h_m^{(3)}(t)e^{i3\phi} \end{aligned} \tag{7.11}$$

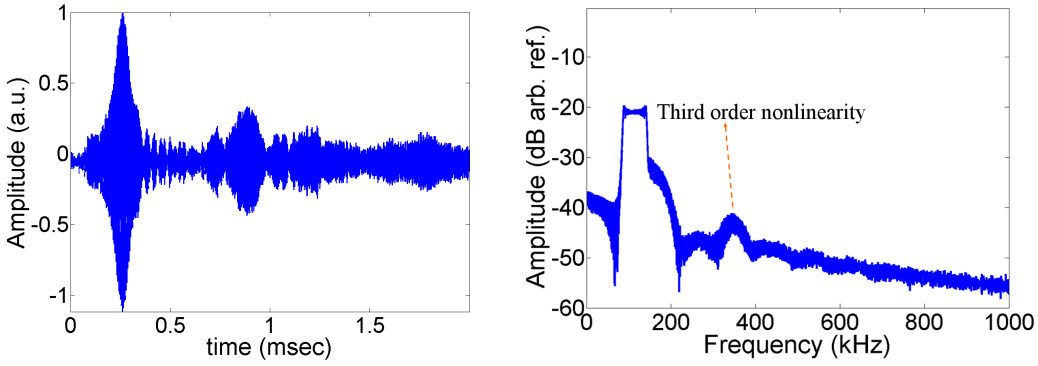

(a) (b)

Figure 7.4: Acquired signal from the mth excitation point (a) and its spectrum containing higher harmonics (b). From this figure is clearly visible that third order contribution is higher than second order

Hence, according to Eqs. (7.9-7.11), Eq. (7.4) becomes:

$$f(t) = h_m^{(1)}(t)e^{i\phi} + \beta h_m^{(2)}(t)e^{i2\phi} + \gamma h_m^{(3)}(t)e^{i3\phi} \tag{7.12}$$

Fig. 7.4 illustrates the output recorded by the receiver from one of the mth excitation points in the time domain and its spectrum containing higher harmonics. The results showed that third order nonlinearity contribution is larger than second order, highlighting the presence of hysteretic material behaviour. Similar results were also experienced by Meo and Zumpano (Meo & Zumpano [2005]).

Therefore, phase symmetry analysis can be used to eliminate the linear part and the even nonlinear harmonics contribution from the signal acquired by the transducers, by simply imposing the third order symmetry condition, $3i\phi = \pm 2\pi ki$, with $k \in \mathbb{N}$, where $\mathbb{N}$ is the set of all natural numbers. Such invariant condition is fulfilled for three different phase angles, $\phi = 0$, $\phi = 2/3\pi$ and $\phi = -2/3\pi$. Indeed, PSA consists in sending three phase shifted FM waveforms into the dam-

aged structure, in order to extract only the nonlinear third order signature:

$$f_0(t) \underbrace{=}_{\phi=0} h_m^{(1)}(t) + \beta h_m^{(2)}(t) + \gamma h_m^{(3)}(t) \tag{7.13a}$$

$$\begin{aligned} f_{2/3\pi}(t) &\underbrace{=}_{\phi=2/3\pi} \mathrm{Re}\left[h_m^{(1)}(t)e^{i2/3\pi} + \beta h_m^{(2)}(t)e^{i4/3\pi} + \gamma h_m^{(3)}(t)e^{i2\pi}\right] \\ &= -\frac{1}{2}h_m^{(1)}(t) - \frac{\beta}{2}h_m^{(2)}(t) + \gamma h_m^{(3)}(t) \end{aligned} \tag{7.13b}$$

$$\begin{aligned} f_{-2/3\pi}(t) &\underbrace{=}_{\phi=-2/3\pi} \mathrm{Re}\left[h_m^{(1)}(t)e^{-i2/3\pi} + \beta h_m^{(2)}(t)e^{-i4/3\pi} + \gamma h_m^{(3)}(t)e^{-i2\pi}\right] \\ &= -\frac{1}{2}h_m^{(1)}(t) - \frac{\beta}{2}h_m^{(2)}(t) + \gamma h_m^{(3)}(t) \end{aligned} \tag{7.13c}$$

where Re[·] indicates that only the real part of the signal was considered for the analysis. Hence, is straightforward that:

$$f_{PSA}(t) = \frac{f_0(t) + f_{2/3\pi}(t) + f_{-2/3\pi}(t)}{3} = \gamma h_m^{(3)}(t) \tag{7.14}$$

where $h_m^{(3)}(t)$ is the *third order nonlinear impulse response*, and in the angular frequency domain Eq. (7.14) becomes:

$$\hat{f}_{PSA}(\omega) = \gamma \hat{h}_m^{(3)}(\omega)\hat{y}_{m0}(\omega) \tag{7.15}$$

which can be written in matrix form as follows:

$$F_{PSA}(\omega) = \gamma \mathbf{H}_m^{(3)}(\omega)\mathbf{Y}_{m0}(\omega) \tag{7.16}$$

where an ideal focusing pattern vector $\mathbf{Y}_{m0}(\omega)$ of length $M \times 1$ was introduced, which corresponds to the signal originating from the defect located at m_0. Its components are $\mathbf{Y}_{m0} = 1$ for $m = m_0$ and $\mathbf{Y}_{m0} = 0$ for $m \neq m_0$. Fig. 7.5 shows the extraction of the third order nonlinear signature by the sum of the responses coming from the same signals sent with different phase angles mentioned previously. For the spatial reciprocity condition, the transpose of the third order nonlinear transfer function, $\mathbf{H}_m^{(3)T}(\omega)$, corresponds to the propagation between

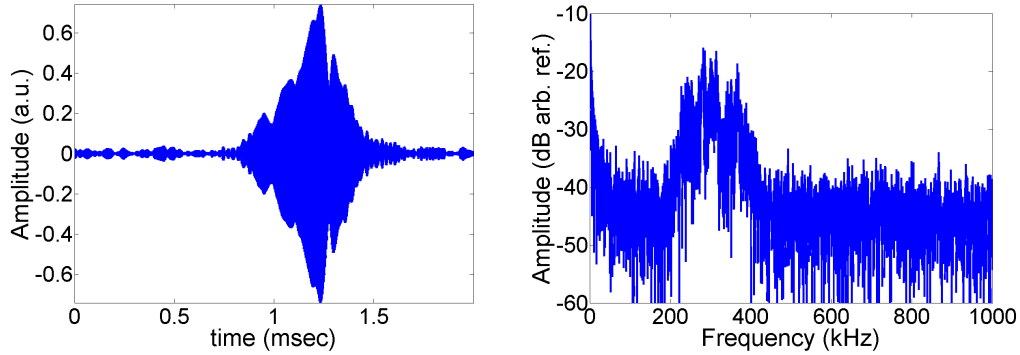

(a) (b)

Figure 7.5: Signal filtered using PSA (a) and its frequencies spectrum (b). From figure (b) it can be clearly seen that only the 3^{rd} order contribution is left

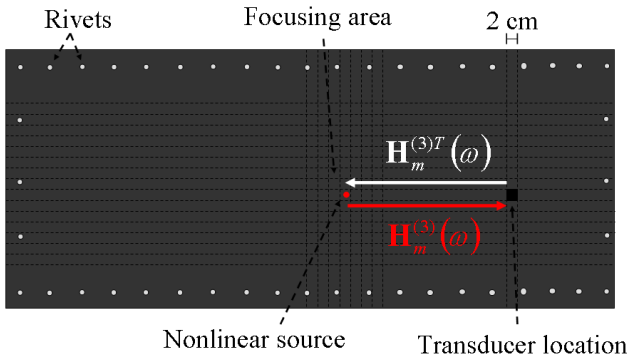

Figure 7.6: Reciprocity condition of the transfer matrix $\mathbf{H}_m^{(3)T}(\omega)$

the receiver and the mth excitation point in the focusing area (Fig. 7.6):

$$\mathbf{Y}_{m0}(\omega) = \gamma \mathbf{H}_m^{(3)T}(\omega) F_{PSA}(\omega) \tag{7.17}$$

Therefore, the M signals, representing a library containing the third order nonlinear impulse response of the medium from each excitation point to the receiver, were recorded and stored.

7.1.2 Nonlinear Inverse Filtering Approach

Similarly to Sec. 6.1.3, the second step consists in focusing energy not only at the location of the nonlinearity (m_0), but also to neighbouring points (M excitation points). Indeed, IF method consists of determining the optimal field distribution on the receiver by simply inverting the third order nonlinear transfer matrix $\mathbf{H}_m^{(3)T}(\omega)$. Such process would give rise after propagation to the field distribution $\mathbf{Y}_{IF}(\omega)$ on the focusing plane. Hence, the nonlinear impulse responses stored were digitized over one-bit and broadcast from their original source location to the focusing area. To one-bit a signal, depending on the sign of the recorded signals, the re-transmitted waveforms were set to ± 1 (the dynamic range limits of the source signal output) in order to increase the amplitude response with a typical gain of approximately 4 dB (Derode *et al.* [1999]).
The optimal wave field distribution $F_{IF}(\omega)$ is obtained by multiplying both the left and right members of Eq. (7.17) for the complex conjugate of $\mathbf{H}_m^{(3)T}(\omega)$ as follows:

$$\mathbf{H}_m^{(3)*}(\omega)\mathbf{Y}_{m0}(\omega) = \mathbf{H}_m^{(3)*}(\omega)\gamma\mathbf{H}_m^{(3)T}(\omega)F_{IF}(\omega) = \gamma\|\mathbf{H}_m^{(3)}(\omega)\|F_{IF}(\omega) \tag{7.18}$$

i.e.

$$F_{IF}(\omega) = \frac{1}{\gamma}\tilde{\mathbf{H}}_m^{(3)}(\omega)\mathbf{Y}_{m0}(\omega) \tag{7.19}$$

where $\tilde{\mathbf{H}}_m^{(3)}(\omega) = \mathbf{H}_m^{(3)*}(\omega)/\|\mathbf{H}_m^{(3)}(\omega)\|$ is the inversion of the third order nonlinear operator and $\|\mathbf{H}_m^{(3)}(\omega)\|$ is the squared norm of $\mathbf{H}_m^{(3)}(\omega)$, which represents the square of the third order nonlinear system's modal energy. According to Sec. 6.4, such inversion increases the number of modes employed for the back-propagation at the focal point (nonlinear source). Indeed, the modes contained in the signal are weighted by the inverse of the energy at each eigenfrequency. In other words, contributions from modes with weak amplitudes are emitted at higher energies, whilst contributions from modes with larger amplitudes are back propagated at lower energies. Hence, with the IF approach, even those modes with weak energy, which are poorly exploited in a simple TR experiment, can participate to the focusing process. Therefore, all the waveforms previously acquired (and 1-bit digitized) from the same excitation points processed with PSA, are broadcast

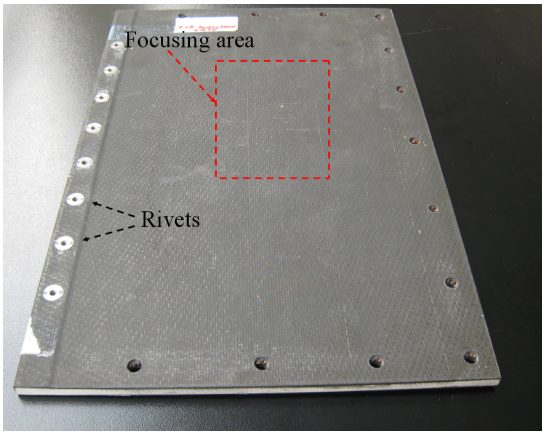

Figure 7.7: Sandwich test sample used in the experiments

into the medium, and the back propagated signal at the damage location is:

$$\mathbf{Y}_{IF}(\omega) = \left[\gamma \mathbf{H}_m^{(3)T}(\omega)\right]_{IF} F_{IF}(\omega) = \left[\mathbf{H}_m^{(3)T}(\omega)\right]_{IF} \tilde{\mathbf{H}}_m^{(3)}(\omega)\mathbf{Y}_{m0}(\omega) \tag{7.20}$$

and the operator $\left[\mathbf{H}_m^{(3)T}(\omega)\right]_{IF} \tilde{\mathbf{H}}_m^{(3)}(\omega)$ is referred to as the *third order nonlinear IF operator*. The above equation results in a maximum at the focus point (nonlinear scatterer location), i.e. when $m = m_0$. Therefore, the focusing on the nonlinear scattering source can be obtained through a nonlinear "virtual" IF experiment.

7.2 Experimental Set-up

The experiments were carried out on a reverberant sandwich plate (750 mm x 405 mm) with rivets (7.9 mm of diameter) (Fig. 7.7). The core used in the sandwich plate was a 6.35 mm thick HRH-10-1/8-4.0 Aramid fibre/phenolic resin nomex. Facing skins were made of four plies of AS4/8552 unidirectional carbon/epoxy prepreg composite on both sides of the core with lay-up sequence of [90/45/45/90]. A dropped-weight impact test machine with a hemispherical tip was used for hitting the test panel at 12 J. Such energy level was chosen in order to inflict damage in the sandwich panel face sheet corresponding to a BVID. A qualitative image of the defect was obtained through an *Active Pulse*

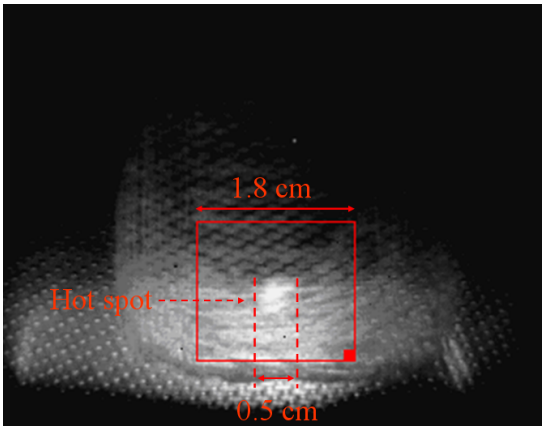

Figure 7.8: Image of the impacted area obtained through an *Active Pulse Thermography*

Thermography, wherein the surface of the sample was actively heated by an external source (a lamp) and the thermal degradation of the heated material was recorded by a high speed Infrared (IR) camera (Pickering & Almond [2008]). As subsurface temperature decay is governed by heat diffusion, retention of heat due to delamination was detected by the camera as a "hot spot" (Fig. 7.8). Two acoustic emission transducers (20mm diameter, 10 mm thickness) with a central frequency of 150 kHz connected to a preamplifier were used to transmit the waveforms from each of the M excitation points ($M = 42$), and to receive the nonlinear elastic responses. In particular, one sensor was instrumented with an oscilloscope (Picoscope 4224) with a sampling rate of 10 MHz. The other AE transducer was linked to an arbitrary signal generator (TTi-TGA12104) to send the chirp signals in the first step and then to send back into the structure the inverted nonlinear responses. The frequency band $B = 70 - 130$ kHz of the FM waveforms was chosen to maximize the efficiency of the available transducers. Moreover, in accordance with the Nyquist theorem, due to the long reverberation present in the signal, a $T = 2$ ms duration time window was chosen. The time histories of the received signals were stored on a computer and processed using a Matlab software code.

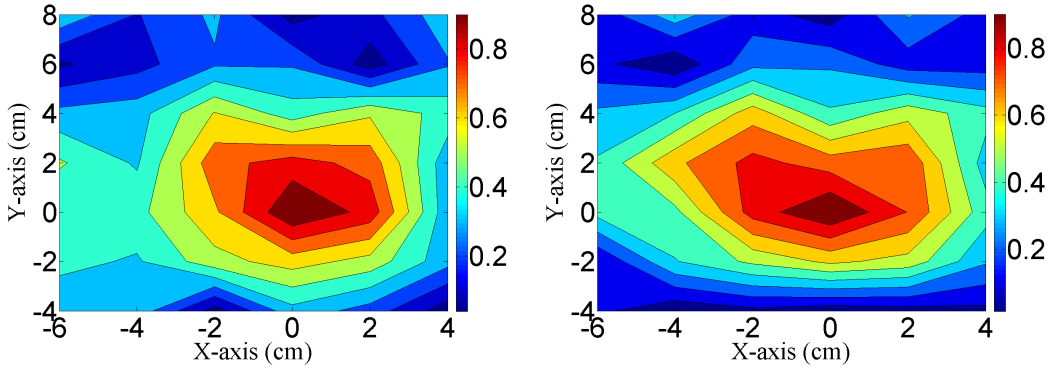

Figure 7.9: 2-D map of the maxima normalized correlation coefficients with the nonlinear imaging method for case 1 (a) and case 2 (b)

7.3 Nonlinear Imaging Results

In order to show the feasibility of this "virtual" imaging method, two different cases were analysed with the receiver sensor placed in two different positions. In case 1, the transducer was positioned at $x_1 = 60$ cm and $y_1 = 17$ cm, whilst, in case 2, it was located close to the lateral boundary of the sandwich plate, with coordinates $x_2 = 4$ cm and $y_2 = 22$ cm. According to Sec. 7.1.2, the refocusing wave fields at the nonlinear signature location (placed at $x = 38$ cm and $y = 24$ cm) are represented by a normalized 2D map of the correlation coefficients represented by Eq. (7.20), and the maxima $\mathbf{Y}_{IF}(\omega)$ in both cases are deduced from the values nearest to 1 (Fig. 7.9). The results indicate that a satisfactory image of the defect was obtained in both cases, with high accuracy. Moreover, due to very simple signal processing, this method requires very little computational time (lower than 1 sec). In accordance with Sec. 6.4, the reciprocal TR technique in reverberant dissipative media is able to increase the contrast, by simply increasing the number of modes participating to the focusing process. In this manner, the effects of distortion (nonlinear attenuation) can be compensated leading to unambiguous retro focusing.

Furthermore, from the results obtained in Fig. 7.9, the following considerations were drawn. First, the focusing can be achieved even when the receiver transducer

is close to the boundary of the reverberant sandwich plate (case 2). Such a result demonstrates experimentally that linear scattering from boundary reflections and modes conversion does not influence negatively the "illumination" of the damage, but only carries the information of the nonlinear source to the far field, where the sensor is located. Hence, the IF method in combination with the benefits of a diffuse wave field was able to enhance the focusing efficiency (accuracy) up to 0% localization error within the grid spacing of 2 cm, even using one receiver transducer. In addition, as the nonlinear coefficient γ is not involved in the imaging process [Eq. (7.20)], compared to other nonlinear TR techniques (Ulrich *et al.* [2008]), such methodology does not require any normalization with the amplitude of the fundamental frequency. Therefore, in principle, this imaging technique can be applied also for those damages wherein the nonlinearity can be described by *Classical Nonlinear Theory*. Moreover, for the nonlinear imaging process, no iterative algorithms nor any a priori knowledge of the mechanical properties of the medium are required.

7.4 Summary of the Nonlinear Imaging Method

In this chapter, an imaging technique of the nonlinear damage signature in a dissipative complex anisotropic structure with hysteretic behaviour is reported. The proposed method relies on a combination of phase symmetry analysis with FM excitation and the nonlinear inverse filtering approach, and it was divided into two steps. In the first step, a number of phase shifted waveforms containing the nonlinear impulse responses of the medium were acquired and summed to extract the third order nonlinearity present in the signals due to delaminations and cracks. Then, a "virtual" nonlinear reciprocal time reversal imaging process was employed as it allows achieving the optimal focusing at the nonlinear source by a compensation of the distortion effects in a dissipative medium. Moreover, exploiting the benefits of a diffuse wave field, a high quality localization, with only one sensor and one transmitter, was accomplished. The efficiency of such a technique was experimentally demonstrated on a dissipative sandwich panel, and the nonlinear source was retrieved with a high level of accuracy with little computational time (less than 1 sec).

Chapter 8

Conclusions

The aim of this thesis was to develop ultrasonic guided wave SHM systems for the localization of the acoustic emission source due to impact events and the assessment of damages in aircraft components. For the identification of the impact point, two main *passive* approaches were considered, an *algorithm-based* and an *imaging-based* method.

The former approach is based on the differences of the stress waves measured by a network of piezoelectric transducers surface bonded on plate-like structures. In particular four PZT films and acoustic emission sensors were used to measure the antisymmetrical A_0 Lamb mode in isotropic materials, whilst six AE transducers were employed to record the wave packets in composite laminates. The waveforms acquired were processed by the analysis of the Continuous Wavelet Transform, and the information contained in the ridge of the scalogram were used to reveal the time of arrival of the stress waves. Then, the coordinates of the impact location and the flexural group speed were obtained by solving a system of nonlinear equations through a combination of local Newton's method associated to line search and polynomial backtracking techniques. One of the main advantages of the proposed optimization algorithm is that it is able to converge from almost any guess point. In addition, the computational time for each source location using Matlab was less than 1 s, meaning that the impact coordinates could be obtained in real time using a compiled code. To validate the *algorithm-based* methods, a number of experiments were carried out using two aluminium structures, a quasi-isotropic composite laminate and a sandwich panel. Good agreement between

the theoretical and experimental results showed that impact point and the group velocities could be predicted with high level of accuracy. Indeed, from the tests conducted on the aluminium structures, the maximum error in estimation of the impact location was less than 4 mm and about 3 m/s for the flexural group velocities. From the experimental results achieved on a quasi-isotropic CFRP laminate and a sandwich panel, the maximum error in estimation of the impact location was approximately 3 mm for the former structure and nearly 2 mm for the latter. Moreover, similar results between the group speeds calculated by the algorithm and the values obtained from the dispersion solutions through a SFEM method were obtained. The *imaging-based* method was developed to detect in real-time the impact source in dissipative composite structure with complex geometries (stiffened panels with rivets and holes). This technique based on the reciprocal time reversal (inverse filtering) approach, was directly applied to the experimental impulse responses (Green's function) of the structure recorded by only one passive sensor and stored into a database. The proposed method allowed achieving the optimal focalization of the AE source as it was able to compensate the distortion effects in a aberrating medium and the dispersive behaviour of guided Lamb waves. Moreover, exploiting the benefits of a diffuse wave field, a high refocusing quality with only one PZT sensor was accomplished. Compared to a simple time reversal process, the robustness of this approach was experimentally demonstrated on a stiffened composite plate and the results showed that the IF technique provides an optimal focusing with a 0% error on the estimation of the impact location. Moreover, for the imaging process, no iterative algorithms were needed.

The most important contribution of the *algorithm-based* and the *imaging-based* approaches is that, in contrast to the current impact localization techniques, they do not require *a priori* knowledge of the mechanical properties, thickness and anisotropic angular-group velocity pattern for the composite laminate. Hence, with a combination of both methodologies, complex computations and numerical models, which are often uncertain and not fully validated with experimental measurements, can be avoided. In this way, both techniques can be integrated into an automated system, which can be used to obtain the impact source location for any kind of composite structure, making the AE source localization problem

more cost effective. In addition, even if the impact localization methods are based on measuring the flexural Lamb mode A_0, such techniques can be applied to the inspection of the extensional Lamb mode.
This thesis also extended *active* ultrasonic guided wave methods to the specific case of dissipative structures showing hysteretic behaviour. Indeed, a nonlinear imaging method, was developed to detect the nonlinear signature in damaged complex anisotropic materials with diffuse field condition. The proposed methodology is based on a combination of inverse filtering approach with phase symmetry analysis and chirp excitation. Phase symmetry analysis was used to characterize the third order nonlinearity of the structure by exploiting its invariant properties with the phase angle of the input waveforms. Then, a "virtual" reciprocal time reversal imaging process, using only one receiver sensor, was used to focus the remitted waveforms on the defect taking advantage of multiple linear scattering. The robustness of this technique was experimentally demonstrated on sandwich panel undergone to barely visible impact damage, and the nonlinear source was retrieved with a high level of accuracy. Its minimal processing requirements make this method a valid alternative to the traditional nonlinear elastic wave spectroscopy techniques for materials showing either classical or non-classical nonlinear behaviour.

8.1 Future Works

The use of ultrasonic guided waves methods for the localization of the impact source and the evaluation of damage mechanisms has shown considerable promise in both isotropic and anisotropic structures. However, additional research is necessary in order to make the transition from the laboratory to a full-scale, operational aircraft.
Specific to the work considered within this thesis, a more powerful language programming should be used to further reduce the computational costs and to perform a simulation tool suitable for industry or embedded in wireless systems. In addition, to give an insight of the Lamb wave propagation within complex structures, a detailed SFEM model that takes into account the material attenuation is

needed. In this manner, a better estimation of the difference between the analytical and experimental group velocities can be provided. Moreover, the methods presented here for the impact source localization must be validated on a wide range of structures of practical engineering interest. The specimens tested during this research represent only a small subset of those being used in the industry, and additional effects (environmental conditions, aero-elastic and aero-acoustic phenomena) are expected while implementing the techniques in real applications. Time reversal has proven to be a very robust method of detecting AE sources and nonlinear scatterers (cracks and delamination). Indeed, the nonlinear imaging methods with time reversal was suitable for the damage detection in complex composite structures. However, while a 2-D spatial/temporal back propagation to find buried features has been successfully demonstrated, a 3-D focusing (through the thickness) still need to be experimentally verified. Moreover, for a better understanding of damage mechanisms, numerical quantitative simulations of the material's nonlinear features must be performed. Indeed, FE analysis would be extremely helpful for the prediction of modulation and higher harmonic generation phenomena within the medium.
In conclusion, current study for impact source identification and damage detection need to be extended to localize multiple impact points and nonlinear scatterers within the material.

8.2 PhD Activities

During the PhD programme a number of scientific papers has been published in international peer-reviewed journals and a number of oral sessions has been presented at international conferences.

Peer-reviewed Journals:

1. Pinto, F., **Ciampa, F.**, Meo, M and Polimeno, U. Multifunctional SMArt Composite material for in situ NDT/SHM and de-icing. *Composite Structures*, 2012. Manuscript in review.

2. **Ciampa, F.** and Meo, M. Nonlinear elastic imaging using reciprocal time reversal and phase symmetry analysis. *Journal of Acoustical Society of America*, 2012. Manuscript accepted for publication.

3. **Ciampa, F.**, Meo, M. and Barbieri, E. Impact localization in anisotropic structures of arbitrary cross-section. *Structural Health Monitoring*, 2012. Manuscript accepted for publication.

4. **Ciampa, F.** and Meo, M. Acoustic emission localization in complex dissipative anisotropic structures using a one-channel reciprocal time reversal method. *Journal of Acoustical Society of America*, 130 (1), pp. 168-175, 2011.

5. **Ciampa, F.** and Meo, M. Acoustic emission source localization in anisotropic structures with diffuse field conditions using a time reversal approach. Proceedings of SPIE - The International Society for Optical Engineering, 7984, 798416, 2011.

6. **Ciampa, F.** and Meo, M. Impact detection in anisotropic materials using a time reversal approach. *Structural Health Monitoring, doi: 10.1177/1475921710395815*, 2011.

7. **Ciampa, F.** and Meo, M. A new algorithm for acoustic emission localization and flexural group velocity determination in anisotropic structures. *Composites: Part A, doi:10.1016/j.compositesa.2010.08.013*, 2010.

8. **Ciampa, F.** and Meo, M. Acoustic emission source localization and velocity determination of the fundamental mode A_0 using wavelet analysis and a Newton-based optimization technique. *Smart Materials and Structures*, **22**(3), pp. 482-489, 2010.

9. Capezzuto, F., **Ciampa, F.**, Carotenuto. G., Meo, M., Milella, E., Nicolais F. A smart multifunctional polymer nanocomposites layer for the estimation of low-velocity impact damage in composite structures. *Composite Structures*, **92**(8), pp. 1913-1919, 2010.

Book Sections:

1. **Ciampa, F.** and Meo, M., 2011. Acoustic emission localization in a composite stiffened panel using a time reversal algorithm. In: Composite Science and Technology. Zurich-Durnten: Trans Tech Publications, pp. 910-915.

Conference Papers:

1. Imaging non-classical elastic nonlinearities using reciprocal time reversal and phase symmetry analysis. **Ciampa, F.**, Meo, M. In:*Proceedings of the SPIE Smart Structures/NDE Conference*, 11 - 15 March 2012, San Diego, California, USA.

2. In-situ damage detection in SMA reinforced CFRP. Pinto, F., **Ciampa, F.**, Meo, M and Polimeno, U. In:*Proceedings of the SPIE Smart Structures/NDE Conference*, 11 - 15 March 2012, San Diego, California, USA.

3. Impact detection in anisotropic materials using a time reversal approach. **Ciampa, F.** and Meo, M. In: *Proceedings of the 8th International Conference On Composite Science And Technology*, 22 - 24 March 2011, Kuala Lumpur, Malaysia.

4. A new wavelet based algorithm for impact identication and group velocity determination in composite structures. **Ciampa, F.** and Meo, M. In: *Proceedings of the 5th European Workshop on Structural Health Monitoring*, 29 June - 02 July 2010, Sorrento, Naples, Italy.

5. A new smart multifunctional polymer nanocomposites layer for the detection of low velocity impact damage in composite structures. Capezzuto, F., **Ciampa, F.**, Carotenuto. G., Meo, M., Milella, E., Nicolais F. In: *Proceedings of the 17th International Conference on Composite Materials*, 27-31 July 2009, Edinburgh, UK.

Moreover, a number of technical meetings on Structural Health Monitoring systems for impact localization and damage detection with Airbus personnel at the University of Bath and in Bristol has been attended.

Appendix A

Elastodynamic Green's Function in Isotropic Media

Let us consider the Green's function for the three-dimensional wave equation resulting from a point source in an unbounded domain. Its Fourier Transform is:

$$\hat{G}(\mathbf{r},\omega;\mathbf{r}_0,\omega_0) = \int_{-\infty}^{+\infty} G(\mathbf{r},t;\mathbf{r}_0,t_0)e^{-i\omega t}d\omega \tag{A.1}$$

whilst the inverse transform of the Green's function in time is:

$$G(\mathbf{r},t;\mathbf{r}_0,t_0) = \frac{1}{2\pi}\int_{-\infty}^{+\infty} \hat{G}(\mathbf{r},\omega;\mathbf{r}_0,\omega_0)e^{i\omega t}d\omega \tag{A.2}$$

For free-space with sound speed c, the Fourier transform of both sides of Eq. (4.6) is (note that $t = t_0 = 0$ for causality reasons) (Duffy [2001]):

$$c^2\int_{-\infty}^{+\infty} \nabla^2 G(\mathbf{r},\mathbf{r}_0;t)e^{-i\omega t}dt - \int_{-\infty}^{+\infty} \frac{\partial^2 G(\mathbf{r},\mathbf{r}_0;t)}{\partial t^2}e^{-i\omega t}dt = -\int_{-\infty}^{+\infty} \delta(\mathbf{r}-\mathbf{r}_0)\delta(t)e^{-i\omega t}dt \tag{A.3}$$

The third term of Eq. (A.3) becomes:

$$\int_{-\infty}^{+\infty} \delta(\mathbf{r}-\mathbf{r}_0)\delta(t)e^{-i\omega t}dt = \delta(\mathbf{r}-\mathbf{r}_0) \tag{A.4}$$

and Eq. (A.3) can be written as the *inhomogeneous Helmholtz's* equation (Barton [1989]):

$$\left(\nabla^2 + k^2\right)\hat{G}(\mathbf{r},\mathbf{r}_0;\omega) = -\delta(\mathbf{r}-\mathbf{r}_0) \tag{A.5}$$

with $k^2 = \omega^2/c^2$. In free space without boundaries, G is a function of only $\|\mathbf{r}-\mathbf{r}_0\|$ that is the distance between the source $\mathbf{r}_0$ and the observation point $\mathbf{r}$, where $\|\cdot\|$ indicates the standard Euclidean vector norm. Thus, Eq. (A.5) in spherical coordinates becomes:

$$\frac{1}{\|\mathbf{r}-\mathbf{r}_0\|}\frac{d^2}{d\|\mathbf{r}-\mathbf{r}_0\|^2}\left[\|\mathbf{r}-\mathbf{r}_0\|\hat{G}(\mathbf{r},\mathbf{r}_0;\omega)\right] + k^2\hat{G}(\mathbf{r},\mathbf{r}_0;\omega) = -\delta(\mathbf{r}-\mathbf{r}_0) \tag{A.6}$$

Its solution is:

$$\hat{G}(\mathbf{r},\mathbf{r}_0;\omega) = \frac{\left(Ae^{ik\|\mathbf{r}-\mathbf{r}_0\|} + Be^{-ik\|\mathbf{r}-\mathbf{r}_0\|}\right)}{4\pi\|\mathbf{r}-\mathbf{r}_0\|} \tag{A.7}$$

and applying the inverse transform to the above equation, we have [4]

$$\begin{aligned} G(\mathbf{r},\mathbf{r}_0;t) &= \frac{1}{2\pi}\int_{-\infty}^{+\infty}\frac{\left(Ae^{ik\|\mathbf{r}-\mathbf{r}_0\|} + Be^{-ik\|\mathbf{r}-\mathbf{r}_0\|}\right)}{4\pi\|\mathbf{r}-\mathbf{r}_0\|}e^{i\omega t}d\omega \\ &= AG_d(\mathbf{r},\mathbf{r}_0;t) + BG_c(\mathbf{r},\mathbf{r}_0;t) \end{aligned} \tag{A.8}$$

where $G_d(\mathbf{r},\mathbf{r}_0;t)$ corresponds to an impulsive diverging spherical wave:

$$G_d(\mathbf{r},\mathbf{r}_0;t) = \frac{1}{4\pi\|\mathbf{r}-\mathbf{r}_0\|}\delta\left(t - \frac{\|\mathbf{r}-\mathbf{r}_0\|}{c}\right) \tag{A.9}$$

[4] $\delta(x) = \lim_{a\to+\infty}\frac{\sin(ax)}{\pi x} = \lim_{a\to+\infty}\frac{1}{2\pi}\int_{-a}^{+a}e^{ixt}dt$

and $G_c(\mathbf{r}, \mathbf{r}_0; t)$ define the impulse converging spherical wave:

$$G_c(\mathbf{r}, \mathbf{r}_0; t) = \frac{1}{4\pi\|\mathbf{r} - \mathbf{r}_0\|}\delta\left(t + \frac{\|\mathbf{r} - \mathbf{r}_0\|}{c}\right) \tag{A.10}$$

The second term of Eq. (A.8) is usually rejected ($B \equiv 0$ and $A = 1$) because it predicts a response to an event occurring in the future $t > 0$. Hence, only the first integral contributes, and the Green's function $G_d(\mathbf{r}, \mathbf{r}_0; t)$ is sometimes called the *retarded Green's function* that takes into account the heterogeneities and the boundaries of the medium (Duffy [2001]).

Appendix B

The Short Time Fourier Transform

The standard Fourier Transform (FT) states that any arbitrary periodic function of time $u(t)$ with period T can be written as the sum of a set of sinusoids:

$$\hat{u}(\omega) = \int_{-\infty}^{+\infty} u(t) e^{-i\omega t} dt \tag{B.1}$$

Eq. (B.1) gives a representation of the frequency content of $u(t)$ obtained averaging over the whole length of the signal. Since FT uses sinusoidal basis function that are localized in frequency but non in time, the identification of high frequency bursts or the characteristics of non-stationary signals may be potentially hindered.

An alternative method to obtain a time-localization is the *Short Time Fourier Transform* (STFT) or *Spectogram* (Mallat [1998]). The key feature of the STFT consists of shifting a window function $g(t)$ to time τ and then computing the

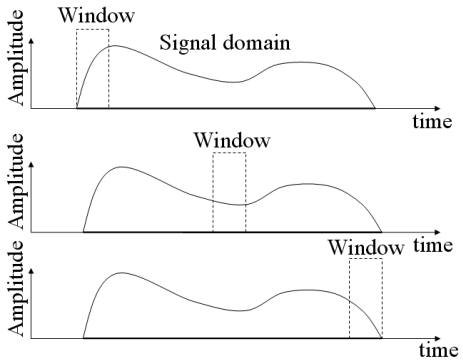

Figure B.1: The Short Time Fourier Transform

Fourier Transform of the product of the signal and the window:

$$\hat{u}^{\text{win}}(\omega,\tau) = \int_{-\infty}^{+\infty} u(t)g(t-\tau)e^{-i\omega t}dt \tag{B.2}$$

where $u(t)$ is the signal to be analysed and $g(t-\tau)e^{-i\omega t}$ a time shifted and modulated version of the window function $g(t)$. The superscript *win* indicates the dependency of the transformed signal on the chosen window function g (Fig. B.1).

Essentially, Eq. (B.2) is a time-frequency cross-correlation of the signals $u(t)$ and $g(t)$, obtained by considering scalar products of $u(t)$ and shifted copies of $g(t)$ of the form $g(t-\tau)e^{-i\omega t}$ (with $\tau,\omega \in \mathbb{R}$). The time-frequency localization provided by the STFT is measured introducing two important parameters, the standard deviation or root mean square (RMS) duration Δt and the RMS bandwidth Δf:

$$\Delta t = \frac{1}{|g(t)|^2}\sqrt{\int_{-\infty}^{+\infty}(t-t_*)^2|g(t)|^2dt} \tag{B.3a}$$

$$\Delta f = \frac{1}{|\hat{g}(f)|^2}\sqrt{\int_{-\infty}^{+\infty}(f-f_*)^2|\hat{g}(f)|^2df} \tag{B.3b}$$

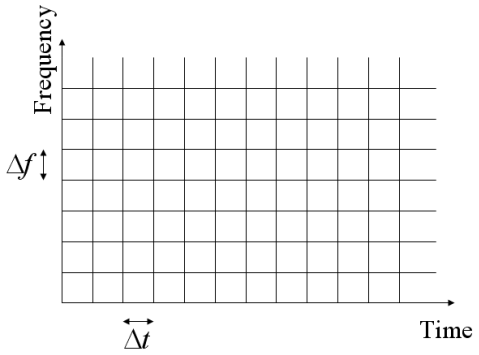

Figure B.2: Tiling of the Heisenberg box for STFT

where $t_* = \int_{-\infty}^{+\infty} t|g(t)|^2 dt / \int_{-\infty}^{+\infty} |g(t)|^2 dt$ and $f_* = \int_{-\infty}^{+\infty} f|\hat{g}(f)|^2 df / \int_{-\infty}^{+\infty} |\hat{g}(f)|^2 df$ are the temporal centre and the central frequency of $g(t)$ and $\hat{g}(f)$, respectively, with $\hat{g}(f)$ the Fourier Transform of the window function. For any time-frequency point (τ_0, f_0), if $g(t)$ has centre t_* and RMS duration Δt, $g(t-\tau)e^{-i\omega t}$ has centre $t'_* = t_* + \tau_0$ and RMS duration $\Delta t' = \Delta t$. Hence, the *time resolution* is Δt. In the frequency domain, assuming that $\hat{g}(f)$ has centre f_* and RMS bandwidth Δf, in a analogous way to the time domain, the new centre is given by $f'_* = f_* + f_0$ and the RMS bandwidth is $\Delta f' = \Delta f$. Therefore, the frequency resolution is Δf. Thus, according to the *uncertainty principle* (also known as *Heisenberg inequality*) that constrains the product of resolution in time and frequency (Teolis [1998]):

$$\Delta t \Delta f \geq \frac{1}{4} \tag{B.4}$$

the time-frequency localization provided by STFT is over the rectangle characterized by an area of $A = \Delta t \Delta f$. Thereby, STFT is not suitable for analysing signals with both very high and very low frequencies (Fig. B.2).

Despite these limitations, the STFT is used in a wide variety of problems, especially those where only high frequency components are of interest and frequency resolution is not critical.

Appendix C

Matched and Mismatched filter Responses of a Chirp Signal

The *pulse compression* or *matched filter* concept is a theoretical framework aimed to process a received broadband signal in order to maximize the sigma-to-noise ratio (SNR) in the presence of white Gaussian noise (Misaridis & Jensen [2005a] and Misaridis & Jensen [2005b]). Indeed, a matched filter behaves as a linear time-invariant system with the output $r(t)$ given by:

$$r(t) = h(t) \otimes y(t) = \int_{-\infty}^{+\infty} \hat{h}(f)\hat{y}(f)e^{i2\pi ft}df \tag{C.1}$$

where $h(t)$ is the time impulse response and $y(t)$ is the input signal. Let us assume the output of the linear system as a sum of a deterministic signal and noise as follows:

$$r(t) = r_s(t) + r_n(t) \tag{C.2}$$

where $r_s(t)$ is a deterministic signal and $r_n(t)$ is the noise. The requirement on the matched filter is that the output signal has to be as large as possible compared to noise at the delay time $t = t_d$, i.e. we want to find an expression for $h(t)$ that

yields the highest SNR η at its output:

$$\eta = \frac{|r_s(t_d)|^2}{|r_n(t)|^2} \tag{C.3}$$

where the numerator and denominator of Eq. (C.3) are the output power and the noise power, respectively. The deterministic output of a pulse-compressed signal at the delay time t_d is:

$$r_s(t_d) = \int_{-\infty}^{+\infty} \hat{h}(f)\hat{y}(f)e^{i2\pi f t_d} df \tag{C.4}$$

where $\hat{h}(f)$ is the transfer function of the system and $\hat{y}(f)$ is the Fourier transform of the input signal. The output power is proportional to the square of the signal amplitude, so that we have:

$$|r_s(t_d)|^2 = \left| \int_{-\infty}^{+\infty} \hat{h}(f)\hat{y}(f)e^{i2\pi f t_d} df \right|^2 \tag{C.5}$$

The noise is assumed to be Gaussian with zero mean and has a flat power spectrum with all the frequencies represented by the same amount of power density N_0. Hence, the spectral density of the input noise is equal to:

$$\hat{y}_{ni}(f) = \frac{N_0}{2} \quad \text{[Watts/Hz]} \tag{C.6}$$

Therefore, the spectral density of the output noise is (Misaridis & Jensen [2005b]):

$$\hat{y}_{no}(f) = \frac{N_0}{2}|\hat{h}(f)|^2 \tag{C.7}$$

and the noise power is equal to:

$$|r_n(t)|^2 = \frac{N_0}{2} \int_{-\infty}^{+\infty} |\hat{h}(f)|^2 df \tag{C.8}$$

Combining Eqs. (C.5) and (C.8), Eq. (C.3) becomes:

$$\eta = \frac{\left| \int_{-\infty}^{+\infty} \hat{h}(f)\hat{y}(f)e^{i2\pi f t_d} df \right|^2}{\frac{N_0}{2} \int_{-\infty}^{+\infty} |\hat{h}(f)|^2 df} \tag{C.9}$$

Using the Schwartz inequality:

$$\left| \int_{-\infty}^{+\infty} \hat{h}(f)\hat{y}(f)e^{i2\pi f t_d} df \right|^2 \leq \int_{-\infty}^{+\infty} |\hat{h}(f)|^2 df \int_{-\infty}^{+\infty} |\hat{y}(f)|^2 df \tag{C.10}$$

the equality is reached if $\hat{y}^*(f)$ is proportional to $\hat{h}(f)$, i.e.:

$$\hat{h}(f) = ke^{-i2\pi f t_d}\hat{y}^*(f) \tag{C.11}$$

where the asterisk denotes complex conjugate and k is an arbitrary constant known as *gain factor*. Substituting Eq. (C.10) into (C.9), we get:

$$\eta \leq \frac{2}{N_0} \int_{-\infty}^{+\infty} |\hat{y}(f)|^2 df \tag{C.12}$$

and the maximum of the above equation is equal to:

$$\max \eta|_{t=t_d} = \frac{2}{N_0} \int_{-\infty}^{+\infty} |\hat{y}(f)|^2 df \tag{C.13}$$

Therefore, the maximum SNR, i.e. the maximum of the peak voltage to noise power ratio, depends only on the transmitted energy and the noise power density. In addition, based on Eq. (C.11) the matched filter has an impulse response equal to the input signal reversed with time except for k and t_d:

$$h(t) = ky(t_d - t) \tag{C.14}$$

As the output response of a pulse-compressed waveform can be written as the convolution of the emitted signal with the impulse response, substituting Eq. (C.11) into (C.1), the following equation is obtained:

$$r(t) = k \int_{-\infty}^{+\infty} \hat{y}(f)\hat{y}^*(f)e^{-i2\pi f(t-t_d)}df = k \int_{-\infty}^{+\infty} |\hat{y}(f)|^2 e^{-i2\pi f(t-t_d)}df = kR_{yy}(t - t_d) \tag{C.15}$$

Hence, a pulse compression response is mathematically equivalent to the auto-correlation R_{yy} of the transmitted signal, shifted by t_d.
If the input signal is a linear FM modulated signal given by the following equation (Misaridis & Jensen [2005a]):

$$c(t) = e^{i\left[2\pi\left(f_0 t + \frac{\mu}{2}t^2\right)\right]} \quad -\frac{T}{2} \leq t \leq \frac{T}{2} \tag{C.16}$$

where f_0 is the central frequency, T is the signal duration, $\mu = B/T$ is the FM slope and B is the total bandwidth that is swept, according to Eq. (C.15), the matched filter output becomes:

$$R_{cc}(t) = \int_{-\infty}^{+\infty} c(t)c(t+\tau)dt = T\frac{\sin\left[\pi BT\frac{t}{T}\left(1 - \frac{t}{T}\right)\right]}{\pi BT\frac{t}{T}}e^{i2\pi f_0 t} \tag{C.17}$$

Pulse compression removes any frequency modulation and the result is a band limited impulse response at the carrier frequency f_0 with a *sinc* shape. The resolution τ_r of such process can be obtained by calculating the first zero of Eq.

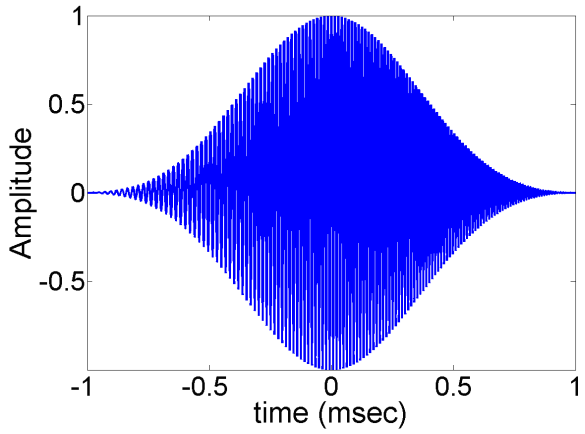

Figure C.1: Windowed (Blackman) chirp excitation

(C.17) through a binomial expansion and taking only the first order term:

$$\tau_r = \frac{T}{2}\left(1 - \sqrt{1 - \frac{4}{BT}}\right) \approx \frac{T}{2}\left[1 - \left(1 - \frac{2}{BT}\right)\right] \approx \frac{1}{B} \tag{C.18}$$

Since imaging with a short (conventional) pulse of width T would lead to resolution of $\tau_r = 1/B$, resolution for a short and for a FM modulated excitation are roughly the same, when the signals use the same bandwidth. However, the side effects of the matched filter mechanism with linear FM are the resulting *sinc* sidelobes, which represents source of mutual interference that can obscure weaker signals.

C.1 The Mismatched Filter

Reduction of the compressed pulse range sidelobes can be accomplished by shaping the transmitted pulse envelope, i.e. by applying a window function (Hanning, Blackman or Dolph-Chebyshev) on the matched filter [Eq. (C.17)] (Fig. C.1). In this manner, the weighted matched filter is referred to *mismatched filter* and Eq.

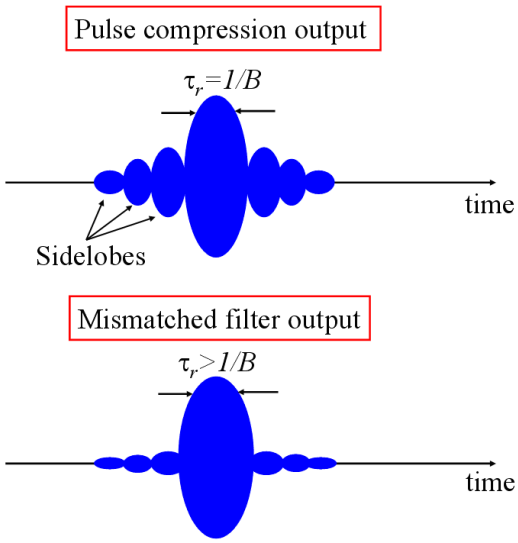

Figure C.2: Matched filter output (a) and mismatched filter output (b) with sidelobes reduction

(C.17) becomes (Mitchell & Rihaczek [1968]):

$$R_{cc}^{w}(t) = \int_{-\infty}^{+\infty} \hat{c}(f)\hat{h}_{MF}(f)e^{i2\pi f_0 t}df \cong h(t) \otimes R_{cc}(t) \tag{C.19}$$

where $\hat{c}(f)$ is the Fourier transform of the linear FM input function, $\hat{h}_{MF}(f) = \hat{w}(f)\hat{c}^*(f)$, $\hat{w}(f)$ is the Fourier transform of the window function and $R_{cc}(t)$ is the autocorrelation function of the input signal $c(t)$. As the linear FM signal has uniform spectral density, we have:

$$R_{cc}(t) = c(t) \otimes c(-t) \cong \delta(t) \tag{C.20}$$

and the output measured in the mismatched filter is proportional to the impulse response $h(t)$. Hence, compared to a simple pulse compression, the effect of a mismatched filter is to reduce the sidelobes well below the level required for diagnostic imaging (Fig. C.2). However, as it can be seen from Fig. C.2, the undesired effect of a mismatched filtering is to widen the axial main lobe of the

output thus slightly decreasing the resolution (although the level is still acceptable) and to reduce the SNR improvement of nearly 1dB (Misaridis & Jensen [2005b]).

References

Achenbach, J. (1984). *Wave Propagation in Elastic Solids*. NorthHolland, New York. 17, 44, 53, 65

Auld, B. (1973). *Acoustic Fields and Waves in Solids*. Wiley-Interscience, New York. 9, 45, 74

Aymerich, F. & Staszewski, W. (2010). Experimental study of impact-damage detection in composite laminates using a cross-modulation vibro-acoustic technique. *Structural Health Monitoring*, **9**, 541–553. 33

Balageas, D., Fritzen, C.P. & Gemes, A. (2006). *Structural Health Monitoring*. London: ISTE LTD. xvii, 2, 3, 9

Barbieri, E. & Meo, M. (2010). Time reversal dort method applied to non-linear elastic wave scattering. *Wave Motion*, **47 (7)**, 452467. 40

Barbieri, E., Cammarano, A., De Rosa, S. & Franco, F. (2009). Waveguides of a composite plate by using the spectral finite element approach. *J. Vibr. Contr.*, **15(3)**, 347367. 55, 56

Barton, D.P. (2009). *Comparative Vacuum Monitoring (CVM)*. John Wiley & Sons, Ltd. 14

Barton, G. (1989). *Elements of Green Functions and Propagation: Potentials, Diffusion and Waves*. Oxford Univ. Press, New York. 48, 66, 69, 158

Bas, P.Y.L., Abeele, K.V.D., Santos, S.D., Goursolle, T. & Matar, O.B. (2006). Experimental analysis for nonlinear time reversal imaging of damaged materials. 26

Bent, A.A., Hagood, N.W. & Rodgers, J.P. (1995). Anisotropic actuation with piezoelectric fiber composites. *Journal of Intelligent Material Systems and Structures*, **6**, 338–349. 19

Bernard, A., Lowe, M.J.S. & Deschamps, M. (2001). Guided waves energy velocity in absorbing and non-absorbing plates. *The Journal of the Acoustical Society of America*, **110**, 186–196. 93

Blomgren, P., Papanicolaou, G. & Zhao, H. (2002). Super-resolution in time-reversal acoustics. *J. Acoust. Soc. Am.*, **111**, 230–248. 79

Bou Matar, O., Li, Y.F. & K., V.D.A. (2009). On the use of a chaotic transducer in nonlinear elastic imaging. *Appl. Phys. Lett.*, **95**, 141913. 132

Brown, L.F. (2000). Disposable pvdf ultrasonic transducers for non-destructive testing applications. *IEEE Transaction on Ultrasonics, Ferroelectrics, and Frequency Control*, **43, No. 3**, 560–568. 17

Brunner, A.J., Birchmeier, M., Melnykowycz, M.M. & Barbezat, M. (2009). Piezoelectric fiber composites as sensor elements for structural health monitoring and adaptive material systems. *Journal of Intelligent Material Systems and Structures*, **20**, 1045–1055. 20

Bussang, J.J., Ehrman, L. & Graham, J.W. (1974). Analysis of nonlinear systems with multiple inputs. *Proc. IEEE*, **62**, 1088–1119. 139

Butrus, K.Y., Cheng, C.H., Degertekin, F.L., Ergun, S., Hansen, S., Jin, X.C. & Oralkan, O. (2000). Silicon micromachined ultrasonic transducers. *Japanese Journal of Applied Physics*, **39**, 2883–2887. 14

Campillo, M. & Paul, A. (2003). Long-range correlations in the diffuse seismic coda. *Science*, **299**, 547549. 79

Capezzuto, F., Ciampa, F., Carotenuto, G., Meo, M., Milella, E. & Nicolais, F. (2010). A smart multifunctional polymer nanocomposites layer for the estimation of low-velocity impact damage in composite structures. *Composite Structures*, **92**, 1913 – 1919. 14

Carminati, R., Saenz, J.J., Greffet, J.J. & Nieto-Vesperinas, M. (2000). Reciprocity, unitarity, and time-reversal symmetry of the s matrix of fields containing evanescent components. *Phys. Rev. A*, **62**, 012712. 79

Cassereau, D. & Fink, M. (1992). Time-reversal of ultrasonic fields. iii. theory of the closed time-reversal cavity. *IEEE Trans. Ultrason. Ferroelectr. Freq.*, **39**, 579592. 70, 73, 74

Cassereau, D., Wu, F. & Fink, M. (1990). Limits of self-focusing using closed time-reversal cavities and mirrors-theory and experiment. In *Ultrasonics Symposium, 1990. Proceedings., IEEE 1990*, 1613 –1618 vol.3. 71, 73

Catheline, S., Queffin, N., Ing, R.K. & Fink, M. (2007). Acoustic source localization model using in-skull reverberation and time reversal. *Appl. Phys. Let.*, **90**, 063902. xii, 41, 42

Cawley, P. (1994). The rapid non-destructive inspection of large composite structures. *Composites*, **25**, 351–357. 10

Chakraborty, A. & Gopalakrishnan, S. (2006). A spectral finite element model for wave propagation analysis in laminated composite plate. *J. Vibr. Acoust.*, **128**, 477–488. 59

Chang, F.K. (1999). Structural health monitoring, a summary report on the first international workshop on structural health monitoring. In *The 2nd International Workshop on Structural Health Monitoring, Stanford University*. 2, 9

Cook, R., Malkus, D., Plesha, M. & Witt, R. (1989). *Concepts and Applications of Finite Element Analysis*. Wiley, New York. 54

Crawley, E. & Anderson, E. (1990). Detailed models of piezoceramic actuation of beams. *Journal of Intelligent Material and Structures*, **1, No. 1**, 4–25. 14

Croxford, A., Wilcox, P., Drinkwater, B. & Konstantinidis, G. (2007). Strategies for guided-wave structural health monitoring. *Proceedings of the Royal Society A: Mathematical, Physical and Engineering Science*, **463**, 2961–2981. 37

Culshaw, B. (1996). *Smart Materials and Structures*. Artech House, Boston, MA. 15

Cunningham, K.B., Hamilton, M.F., Brysev, A.P. & Krutyansky, L.M. (2001). Time reversed sound beams of finite amplitude. *J. Acoust. Soc. Am.*, **109**, 26682674. 125

Daraio, C.U.R.P.P.P.U., Chiara (Pasadena (2009). Method and apparatus for nondestructive evaluation and monitoring of materials and structures. 137

David, J. & Cheeke, N. (2002). *Fundamental and Applications of Ultrasonic Waves*. Boca Raton, FL: CRC. xi, 13, 14

De Rosny, J. & Fink, M. (2002). Overcoming the diffraction limit in wave physics using a time-reversal mirror and a novel acoustic sink. *Phys. Rev. Lett.*, **89(12)**, 124301. 79

Deng, M. (1999). Cumulative second-harmonic generation of lamb-mode propagation in a solid plate. *Journal of Applied Physics*, **85**, 3051 –3058. 26

Deng, M. (2003). Analysis of second-harmonic generation of lamb modes using a modal analysis approach. *Journal of Applied Physics*, **94**, 4152 –4159. 27

Dennis, J.E. & Schnabel, R.B. (1983). *Numerical Methods for Unconstrained Optimization and Nonlinear Equations*. Englewood Cliffs, NJ: Prentice Hall. 95, 98, 99

Derode, A., Roux, P. & Fink, M. (1995). Robust acoustic time reversal with high-order multiple scattering. *Phys. Rev. Lett.*, **75**, 4206. 79

Derode, A., Tourin, A. & Fink, M. (1999). Ultrasonic pulse compression with one bit time reversal through multiple scattering. *J. App. Phys.*, **85 (9)**, 6343–6352. 126, 145

Derode, A., Larose, A., Campillo, M. & Fink, M. (2003a). How to estimate the green's function of a heterogeneous medium between two passive sensors? application to acoustic waves. *Appl. Phys. Lett.*, **83 (15)**, 3054–56. 79

Derode, A., Larose, E. & Tanter, J.T.A.C.M.F.M., M.and De Rosny (2003b). Recovering the greens function from field-filed correlations in an open scattering medium (l). *J. Acoust. Soc. Am.*, **113 (6)**, 29732976. 79

Diamanti, K., Hodgkinson, J.-M. & Soutis, C. (2002). Damage detection of composite laminates using pzt generated lamb waves. In *Proceedings of the First European Workshop Structural Health Monitoring*. 10, 18

Diamanti, K., Soutis, K.., Hodgkinson & J.-M. (2007). Piezoelectric transducers arrangement for the inspection of large composite structures. *Composites: Part A*, **38**, 1121–1130. 18

Doebling, S.W., Farrar, C.R., Prime, M.B. & Shevitz, D.W. (1996). Damage identification and health monitoring of structural and mechanical system from change in their vibration characteristics: A literature review. *Los Alamos National Laboratory report, LA-13070-MS*. 10, 11, 12

Doebling, S.W., Farrar, C.R. & Prime, M.B. (1998). A summary review of vibration-based damage identification methods. *The Shock and Vibration Digest*, **30, No. 2**, 91–105. 11

Dorme, C. & Fink, M. (1995). Focusing in transmit-receive mode through inhomogeneous media: The time reversal matched filter approach. *J. Acoust. Soc. Am.*, **98 (2)**, 11551162. 78

Dos Santos, S., Haumesser, L., Vander Meulen, F. & Bou Matar, O. (2004). Optimized excitation sources and exact solutions for ultrasonic field propagation in a nonlinear medium with hysteretic behaviour. *IEEE Trans. Ultrason. Ferroelect. Freq. Contr.*, **2**, 930–933. 137

Draeger, C. & Fink, M. (1997). One-channel time reversal of elastic waves in a chaotic 2d-silicon cavity. *Phys. Rev. Lett.*, **79**, 407. 80

Duffy, D. (2001). *Green's Function with Applications*. CRC Press, Boca Raton. 66, 72, 157, 159

El youbi, F., Grondel, S. & Assaad, J. (2004). Signal processing for damage detection using two different array transducers. *Ultrasonics*, **42**, 803–806. 18

Evans, M.J. & Cawley, P. (1999). Measurement and prediction of diffuse fields in structures. *J. Acoust. Soc. Am.*, **106 (6)**, 334861. 79, 131

Fink, M. (1992). Time reversal of ultrasonic fields. i: Basic principles. *IEEE Trans. Ultrason. Ferroelec. Freq. Contr.*, **39(5)**, 555566. 39, 71, 75

Fink, M. (1997). Time reversed acoustics. *Physics Today*, **50**, 3440. 77

Finnveden, S. (2004). Evaluation of modal density and group velocity by a finite element method. *J. Sound Vib.*, **273(1)**, 5175. 62

Gao, Y. & Spencer, F.J. (2002). Damage localisation under ambient vibration using changes in flexibility. *Journal of Earthquake Engineering and Earthquake Vibration*, **1, No. 1**, 136–144. 12

Gaul, L. & Hurlebaus, S. (1999). Determination of the impact force on a plate by piezoelectric film sensors. *Arch. Appl. Mech.*, **69**, 691–701. 18, 23, 91

Gaul, L., Hurlebaus, S. & Jacobs, L.J. (2001). Localization of a synthetic acoustic emission source on the surface of a fatigue specimen. *Res. Nondestruct. Eval.*, **13**, 105–117. 34

Gentilman, R., McNeal, K. & Schmidt, G. (2003). Enhanced performance active fiber composites. In *Proceedings of SPIEs 10th Symposium on Smart Structures and Materials Conference*. 19

Giurgiutiu, V. (2002). Lamb wave generation with piezoelectric wafer active sensors for structural health monitoring. In *SPIEs 10th Annual International Symposium on Smart Structures and Material and 8th Annual International Symposium on NDE for Health Monitoring and Diagnostics, San Diego, CA*. 10, 17, 18

Giurgiutiu, V. & Zagrai, A.N. (2000). Characterization of piezoelectric wafer active sensors. *Journal of Intelligent Material Systems and Structures*, **11**, 959–976. 14

Goursolle, T., Call, S. & Dos Santos, O., S.and Bou Matar (2007). A two dimensional pseudospectral model for time reversal (tr) and nonlinear elastic wave spectroscopy (news). *J. Acoust. Soc. Am.*, **122 (6)**, 32203229. 40

Greblicki, W. (1997). Nonparametric approach to wiener system identification. *IEEE Trans. Circ. Syst. - I: Fundamental Theory and Applications*, **44 (6)**, 538545. 140

Gruber, F.K., Marengo, E.A. & Devaney, A.J. (2004). Time-reversal imaging with multiple signal classification considering multiple scattering between the targets. *J. Acoust. Soc. Am.*, **115(6)**, 3042– 3047. 39

Guyer, R.A. & Johnson, P.A. (1999). Nonlinear mesoscopic elasticity: evidence for a new class of materials. *Phys Today*, **52**, 30–36. 26, 27, 32

Guyer, R.A., Mc Call, K.R. & Boitnott, G.N. (1994). Hysteresis, discrete memory and nonlinear wave propagation in rock: a new paradigm. *Phys Rev Lett*, **74**, 3491–94. 28

Haase, M. & Widjajakusuma, J. (2003). Damage identification based on ridges and maxima lines of the wavelet transform. *Int. J. Eng. Sci.*, **41**, 1423–1443. 93

Hayashi, T., Song, W.J. & Rose, J.L. (2003). Guided wave dispersion curves for a bar with an arbitrary cross-section, a rod and rail example. *Ultrasonics*, **41**, 175183. 55

Hodges, C.H., Power, J. & Woodhouse, J. (1985). The use of the spectrogram in structure acoustic and an application to the vibrations of cylindrical shells. *Journal of Sound and Vibration*, **101, No. 2**, 203–218. 21

Hurlebaus, S., Niethmmer, M., Jacobs, L. & Valle, C. (2001). Automated methodology to locate notches with lamb waves. *Acoustic Research Letters Online*, **2, No. 4**, 97–102. 10

Hutchins, D.A., Jansen, D.P. & Edwards, C. (1993). Lamb wave tomography using non-contact transduction. *Ultrasonics*, **31**, 97–103. 38

Ihn, J.B. & Chang, F.K. (2004). Detection and monitoring of hidden fatigue crack growth using a built-in piezoelectric sensor/actuator network: Ii.validation using riveted joints and repair patches. *Smart Materials and Structures*, **13**, 621. 21

Ihn, J.B. & Chang, F.K. (2008a). Detection and monitoring of hidden fatigue crack growth using a built-in piezoelectric sensor/actuator network: I diagnostics. *Smart Materials and Structures*, **7**, 5–15. xii, 36, 37

Ihn, J.B. & Chang, F.K. (2008b). Pitch-catch active sensing methods in structural health monitoring for aircraft structures. *Structural Health Monitoring*, **13, No. 3**, 443–450. xi, 24, 25

Ikeda, T. (1996). *Fundamentals of Piezoelectricity*. Oxford Univ. Press, New York. 16

Ing, R.K., Quieffin, N., Catheline, S. & Fink, M. (2005). In solid localization of finger impacts using acoustic time-reversal process. *Appl. Phys. Lett.*, **87**, 204104. 42, 129

Jackson, D.R. & Dowling, D.R. (1991). Phase conjugation in underwater acoustics. *J. Acoust. Soc. Amer.*, **89**, 171181. 77

Jeong, H. & Jang, Y.S. (2000). Fracture source location in thin plates using the wavelet transform of dispersive waves. *IEEE Transaction on Ultrasonics, Ferroelectrics, and Frequency Control*, **47, No. 3**, 612–619. 23, 54, 91

Jin, Y., O'Donoughue, N. & Moura, J.M. (2008). Position location by time reversal in communication networks. In *International Conference on Acoustics, Speech, and Signal Processing, Las Vegas, CA*. 42

Johnson, P.A. (1999). The new wave in acoustic testing. *Materials World*, **7**, 544546. xi, 27, 29, 32

Johnson, P.A. (2006). *The Universality of Nonclassical Nonlinearity (with application to Nondestructive Evaluation and Ultrasonics)*. Springer New York. xii, 30, 31, 135

Kang, I., Schulz, M.J., Kim, J.H., Shanov, V. & Shi, D. (2006). A carbon nanotube strain sensor for structural health monitoring. *Smart Materials and Structures*, **15**, 737. 14

Kazakov, V.V., Sutin, A. & Johnson, P.A. (2002). Sensitive imaging of an elastic nonlinear wave-scattering source in a solid. *Appl. Phys. Lett*, **81**, 646648. 140

Kehlenback, M. & Hanselka, H. (2003). Automated structural integrity monitoring based on broadband lamb wave excitation and matched filtering. In *The 44th AIAA/ASME/ASCE/AHS Structures, Structural Dynamics, and Materials Conference, Norfolk, Virginia*. 24

Kosel, T., Grabec, I. & Kosel, F. (2003). Intelligent location of simultaneously active acoustic emission sources. *Aircraft Engineering and Aerospace Technology*, **75, No. 1**, 11–17. 22

Kundu, T., Das, S. & V.-J., K. (2009). Detection of the point of impact on a stiffened plate by the acoustic emission technique. *Smart Materials and Structures*, **18**, 1–9. xii, 34, 35

Kurokawa, Y., Mizutani, Y. & Mayozumi, M. (2005). Real-time executing source location system applicable to anisotropic thin structures. *Journal of Acoustic Emission*, **23**, 224–232. xii, 35, 36

Lanza Di Scalea, F., Matt, H., Bartoli, I., Coccia, S., Park, G. & Farrar, C. (2007). Health monitoring of uav wing skin-to-spar joints using guided waves and macro fiber composite transducers. *Journal of Intelligent Material Systems and Structures*, **18**, 373–388. 20

Latif, R., Aassif, E.H., Maze, G., Moudden, A. & Faiz, B. (1999). Determination of the group and phase velocities from time-frequency representation of wigner-ville. *NDT&E International*, **32, No. 7**, 415–422. 21

Le, T.P. & Argoul, P. (2004). Continuous wavelet transform for modal identification using free decay response. *J. Sound Vib.*, **277**, 73–100. 88

Lee, U. & Shin, J. (2001). Frequency response-based structural damage identification method. *Computer and Structures*, **80**, 117–132. 11

Leonard, K.R., Malyarenko, E.V. & Hinders, M.K. (2002). Ultrasonic lamb wave tomography. *Inverse Problems*, **18**, 1795–1808. xii, 37, 38

Lin, M. & Chang, F.K. (2002). The manufacture of composite structures with a built-in network of piezoceramics. *Composites Science and Technology*, **62**, 919 – 939. 21

Lin, M., Qing, X., Kumar, A. & Beard, S.J. (2001). Smart layer and smart suitcase for structural health monitoring applications. vol. 4332, 98–106, SPIE. 21

Lin, X. & Yuan, F. (2001). Diagnostic lamb waves in an integrated piezoelectric sensor/actuator plate: analytical and experimental studies. *Smart Mater. Struct.*, **10**, 907–913. 18

Lin, X. & Yuan, F.G. (1999). Imaging the damage in the plate with migration technique. In *Proceedings of 2nd International Workshop on Structural Health Monitoring, Stanford University*. 38

Lobkis, O.I. & Weaver, R.L. (2000). Complex modal statistics in a reverberant dissipative body. *J. Acoust. Soc. Am.*, **108 (4)**, 1480–1485. 131

Lobkis, O.I. & Weaver, R.L. (2001). On the emergence of the green's function in the correlations of a diffuse field. *J. Acoust. Soc. Am.*, **110 (6)**, 301117. 79

Love, A.E.H. (1926). *Some Problems of Geodynamics*. Cambridge University Press, Cambridge. 13

Lowe, M.J.S. (1995). Matrix techniques for modeling ultrasonic waves in multilayered media. *IEEE Trans. Ultrason. Ferroelectr. Freq. Control*, **42**, 525542. 53

Mall, S. & Hsu, T.L. (2000). Electromechanical fatigue behaviour of graphite/epoxy laminate embedded with piezoelectric actuator. *Smart Materials and Structures*, **9**, 78–84. 18

Mallat, S. (1998). *A wavelet tour of signal processing*. London: Academic Press. 89, 91, 93, 160

Malyarenko, E.V. & Hinders, M.K. (2000). Fan beam and double crosshole lamb wave tomography for mapping flaws in aging aircraft structures. *Journal of Acoustic Society of America*, **108**, 1631–1639. 38

Marchi, L.D., Marzani, A., Speciale, N. & Viola, E. (2011). A passive monitoring technique based on dispersion compensation to locate impacts in plate-like structures. *Smart Materials and Structures*, **20**, 035021. 34

Matt, H. & di Scalea F., L. (2007). Macro-fibre composite piezoelectric rosettes for acoustic source location in complex structures. *Smart materials and Structures*, **16**, 1489–1499. 36

Meo, M. & Zumpano, G. (2005). Nonlinear elastic wave spectroscopy identification of impact damage on sandwich plate. *Compos Struct*, **71**, 469474. 32, 135, 142

Meo, M., Zumpano, G., Pigott, M. & Marengo, G. (2005). Impact identification on a sandwich plate from wave propagation responses. *Composite Structures*, **71**, 302–306. xi, 23, 35, 91

Michaels, J.E. & Michaels, T.E. (2007). Damage localization in inhomogeneous plates using a sparse array of ultrasonic transducers. *AIP Conference Proceedings*, **894**, 846–853. 36

Mindlin, R.D. (1959). *Waves and vibrations in isotropic, elastic plates*. J.N. Goodir and N. Hoff, Editors, Structural Mechanics, Pergamon Press, Oxford, 199232. 53

Misaridis, T. & Jensen, J.A. (2005a). Use of modulated excitation signals in medical ultrasound. part i. basic concepts and expected benefits. *Trans. Ultrason, Ferroelect, Freq. Contr.*, **52 (2)**, 177–191. 138, 139, 163, 166

Misaridis, T. & Jensen, J.A. (2005b). Use of modulated excitation signals in medical ultrasound. part ii. design and performance for medical imaging applications. *IEEE Trans. Ultrason, Ferroelect, Freq. Contr.*, **52 (2)**, 192–207. 163, 164, 169

Mitchell, R.L. & Rihaczek, A.W. (1968). Matched-filter responses of the linear fm waveform. *Aerospace and Electronic Systems, IEEE Transactions on*, **AES-4**, 417 –432. 168

Monkhouse, R.C., Wilcox, P.W., Lowe, M.S. & Dalton, P., R.-P. andCawley (2000). The rapid monitoring of structures using interdigital lamb wave transducers. *Smart Materials and Structures*, **9**, 753–780. 18

Moulin, E., Assaad, J., Delebarre, C., Kaczmarek, H. & Balageas, D. (1997). Piezoelectric transducer embedded in a composite plate: application to lamb wave generation. *Journal of Applied Physics*, **82 (5)**, 2049–2055. 18

Moussatov, A. & Gusev, V. (2003). Self-induced hysteresis for nonlinear acoustic waves in cracked material. *Phys. Rev. Lett.*, **90**, 124301. 31

Nayfeh, A. (1991). The general problem of elastic wave propagation in multilayered anisotropic media. *J. Acoust. Soc. Am.*, **89**, 15211531. 53

Newland, D.E. (1997). Practical signal analysis: do wavelets make any difference? In *Proceedings of DETC97 ASME Design Engineering Technical Conferences, Sacramento, CA*. 88

Nocedal, J. & Wright, S.J. (1999). *Numerical Optimization*. Springer Series in Operations Research (Berlin: Springer). 97

Ostrovsky, L. & Johnson, P.A. (2001). Dynamic nonlinear elasticity in geomaterials. *Riv. Nuovo Cim.*, **24**, 1–46. xii, 26, 28, 29, 30

Paget, C.A., Grondel, S., Levin, K. & Delebarre, C. (2002a). Damage detection in composites by a wavelet-coefficient technique. In *Proceedings of the First European Workshop Structural Health Monitoring*. 10

Paget, C.A., Levin, K. & Delebarre, C. (2002b). Actuation performance of embedded piezoceramic transducer in mechanically loaded composites. *Smart Materials and Structures*, **11**, 886–891. 18

Paget, C.A., Atherton, K. & OBrien, E. (2003). Triangulation algorithm for damage location in aeronautical composite structures. In *Proceeding of the 4th International Workshop on Structural Health Monitoring, Stanford, CA,*. 35

Papoulis, A. (1984). *Signal Analysis*. McGraw-Hill, New York. 76

Park, H.W., Kim, S.B. & Sohn, H. (2009). Understanding a time reversal process in lamb wave propagation. *Wave Motion*, **46**, 451 – 467. 41

Parot, J.M. (2008). Localizing impulse sources in an open space by time reversal with very few transducers. *App. Acoust.*, **69**, 311–324. 42

Pickering, S. & Almond, D.P. (2008). Matched excitation energy comparison of the pulse and lock-in thermography nde techniques. *NDT&E Int.*, **41**, 501–509. 147

Prada, C., Wu, F. & Fink, M. (1991). The iterative time reversal mirror: a solution to self focusing in pulse-echo mode. *J. Acoust. Soc. Am.*, **90**, 1119–29. 39

Prada, C., Mannevile, S., Spoliansky, D. & Fink, M. (1996). Decomposition of the time reversal operator: detection and selective focusing on two scatterers. *J. Acoust. Soc. Amer.*, **99**, 20672076. 39

Quek, S.T., Wang, Q., Zhang, L. & Ong, K.H. (2001). Practical issues in the detection of damage in beams using wavelets. *Smart Materials and Structures*, **10**, 1009–1017. 10

Quieffin, N. (2004). *Etude du rayonnement acoustique de structures solides: vers un systeme d' imagerie haute resolution*. Ph.D. thesis, University Paris VI. 131

Rayleigh, J.W.S. (1887). On waves propagated along the plane surface of an elastic solid. In *Proceedings of the London Mathematical Society, 17: 4-11*. 13

Reddy, J.N. (1984). A simple higher-order theory for laminated composite plates. *J. Appl. Mech.*, **51**, 745–752. 54

Roundy, S., Wright, P.K. & Rabaey, J. (2003). A study of low level vibrations as a power source for wireless sensor nodes. *Computer Communications*, **26**, 1131 – 1144, ubiquitous Computing. xi, 16, 17

Roux, P. & Fink, M. (2003). Green's function estimation using secondary sources in a shallow water environment. *J. Acoust. Soc. Am.*, **113**, 14061411. 79

Roux, P., Roman, B. & Fink, M. (1997). Time-reversal in an ultrasonic waveguide. *Appl. Phys.Lett.*, **70(14)**, 18111813. 78

Sabra, K.G., Srivastava, A., Lanza di Scalea, F., Bartoli, I., Rizzo, P. & S., C. (2008). Structural health monitoring by extraction of coherent guided waves from diffuse fields. *J. Acoust. Soc. Am.*, **123 (1)**. 121

Salamone, S., Bartoli, I., Di Leo, P., Lanza Di Scala, F., Ajovalasit, A., D'Acquisto, L., Rhymer, J. & Kim, H. (2010). High-velocity impact location on aircraft panels using macro-fiber composite piezoelectric rosettes. *Journal of Intelligent Material Systems and Structures*, **21**, 887–896. 36

Scalerandi, A.S.B.C.L.E., M .and Gliozzi, Masera, D. & Bocca, P. (2008). A scaling method to enhance detection of a nonlinear elastic response. *Appl. Phys. Lett.*, **92**, 101912. 40

Seydel, R. & Chang, F.K. (2001). Impact identification on stiffened composite panels: system development. *Smart Materials and Structures*, **10**, 354–369. xi, 22, 23, 35

Sholte, J. (1942). On the stoneley wave equation. In *Proc. Kon. Nederl. Akad. Wetensch, 45 (20-5): 159-164*. 13

Shorter, P. (2004). Wave propagation and damping in linear viscoelastic laminates. *J. Acoust. Soc. Am.*, **115**, 1917–25. 55

Sohn, G., H. andPark, Wait, J., Limbark, N.P. & Farrar, C.R. (2004). Wavelet-based active sensing for delamination detection in composite structures. *Smart Materials and Structures*, **13, No. 1**, 153–160. 24

Stoneley, R. (1924). Elastic waves at the surface of separation of two solids. In *Proceedings of the Royal Society of London, Series A, 106: 416-428*. 13

Studer, M. & Peters, K. (2003). Multi-scale sensing for damage identification. *Smart Materials and Structures*, **13**, 283–294. 25

Sung, D.U., Oh, J.H., Kim, C.G. & Hong, C.S. (2000). Impact monitoring of smart composite laminates using neural network and wavelet analysis. *Journal of Intelligent Material Systems*, **11**, 180–190. 35

Sutin, A., Libbey, B., Fillinger, L. & Sarvazyan, L. (2009). Wideband nonlinear time reversal seismo-acoustic method for landmine detection. *J. Acoust. Soc. Am.*, **125**, 19061910. 41

Tanter, M., Thomas, J.L. & Fink, M. (1998). Focusing and steering through absorbing and aberrating layers: Applications to ultrasonic propagation through the skull. *J. Acoust. Soc. Am.*, **103 (5)**, 24032410. 124

Tanter, M., Thomas, J.L. & Fink, M. (2000). Time reversal and the inverse filter. *J. Acoust. Soc. Am.*, **108 (1)**, 223234. 125, 126

TenCate, J.A., Smith, E. & Guyer, R.A. (2000). Universal slow dynamics in granular solids. *Phys. Rev. Lett.*, **85**, 10201023. 31

Teolis, A. (1998). *Computational Signal Processing with Wavelets*. Birkhauser, Boston,. 91, 162

Tobias, A. (1976). Acoustic emission source location in two dimensions by an array of three sensors. *Nondestruct. Test. Eval.*, **9**, 9–12. 34

Tverdokhlebov, A. & Rose, J. (1988). On green's function for elastic waves in anisotropic media. *J. Acoust. Soc. Am.*, **83**, 118121. 69

Tzou, H.S. (2003). *Piezoelectric Shells: Distributed Sensing and Control of Continua*. Kluwer Academic Publishers, Boston/Dordrecht. 16, 17, 102

Udd, E. (1994). *Fiber-optic Smart Structure*. Wiley Interscience, New York. 14

Ulrich, T.J., Johnson, P.A. & Sutin, A. (2006). Imaging nonlinear scatterers applying the time reversal mirror. *J. Acoust. Soc. Am.*, **119 (3)**, 1514–1518. 40

Ulrich, T.J., Johnson, P.A. & Guyer, R.A. (2007). Interaction dynamics of elastic waves with a complex nonlinear scatterer through the use of a time reversal mirror. *Phys. Rev. Lett.*, **98**, 104301. xii, 40

Ulrich, T.J., Sutin, T., A.-M. andClaytor, Papin, P., Le Bas, P.Y. & TenCate, J.A. (2008). The time reversed elastic nonlinearity diagnostic applied to evaluation of diffusion bonds. *Appl. Phys. Lett.*, **93**, 151914. 25, 41, 149

Van Den Abeele, K.E.A., Johnston, P.A. & Sutin, A. (2000). Nonlinear elastic wave spectroscopy (news) techniques to discern material damage, part i: nonlinear wave modulation spectroscopy (nwms). *Res. Nondestr. Eval.*, **12 (1)**, 17–30. 31, 32

Van Den Abeele, K.E.A., Sutin, A., Carmeliet, J. & Johnston, P.A. (2001). Micro-damage diagnostics using nonlinear elastic wave spectroscopy (news). *NDT&E International*, **34**, 239–248. 29

Viktorov, I.A. (1967). *Rayleigh and Lamb waves. Physical Theory and Applications*. Plenum Press New York. 13, 18, 47

Wang, L. & Yuan, F.G. (2005). Damage identification in a composite plate using prestack reverse-time migration technique. *Structural Health Monitoring*, **4 (3)**, 195–211. 39

Wang, L. & Yuan, F.G. (2007). Group velocity and characteristic wave curves of lamb waves in composites: Modelling and experiments. *Compos. Sci. Tech.*, **67**, 13701384. 54

Wang, W. & Chen, G. (2010). Ground motion effect on the performance of a neural network based structural health monitoring strategy. vol. 369, 299–299, ASCE. 25

Wapenaar, K., Fokkema, J. & Snieder, R. (2005). Retrieving the greens function in an open system by cross correlation: A comparison of approaches (l). *J. Acoust. Soc. Am.*, **118 (5)**, 27832786. 79

Weaver, R. (1982). On diffuse waves in solid media. *J. Acoust. Soc. Am.*, **71 (6)**, 160809. 79

White, P.H. (1969). Cross correlation in structural systems: Dispersion and nondispersion waves. *J. Acoust. Soc. Am.*, **45**, 1118–1128. 22

Whitney, J.M. & Pagano, N.J. (1970). Shear deformation in heterogeneous anisotropic plates. *J. Appl. Mech.*, **37**, 1031–36. 54

Wilcox, P. (2004). Modeling the excitation of lamb and sh waves by point and line sources. *AIP Conference Proceedings*, **700**, 206–213. 17

Wilcox, P., Castaings, M., Monkhouse, R., Cawley, P. & Lowe, M. (1997). An example of the use of interdigital pvdf transducers to generate and receive a high order lamb wave mode in a pipe. *Review of Progress in Quantitative Nondestructive Evaluation*, **16/A**, 919–926. 14

Wilkie, w.K., Bryant, R.G., High, J.W., Fox, R.L., Hellbaum, R.F., Jalink, A.J., Little, B.D. & Mirick, P.H. (2000). Low-cost piezocomposite actuator for structural control applications. In *Proc. SPIE 3991, 323*. xi, 19, 20, 21

Wu, F., Thomas, J.L. & Fink, M. (1992). Time-reversal of ultrasonic fields-part ii: Experimental results. *IEEE Trans. Ultrason. Ferroelectr. Freq. Control*, **39**, 567578. 76

Yang, W.X., Hull, J.B. & Seymour, M.D. (2004). A contribution to the applicability of complex wavelet analysis of ultrasonic signals. *NDT&E International*, **37**, 497–504. 89

Zaitsev, V.Y., Gusev, V. & Castagnde, B. (2002). Observation of the luxemburg-gorky effect for elastic waves. *Ultrasonics*, **40**, 627 – 631. 33

Ziola, S.M. & Gorman, M.R. (1991). Source location in thin plates using cross-correlation. *Journal of the Acoustic Society of America*, **90**, Journal of the Acoustic Society of America. 22

Zumpano, G. & Meo, M. (2007). A new nonlinear elastic time reversal acoustic method for the identification and localisation of stress corrosion cracking in welded plate-like structures a simulation study. *Int. J. Solids Struct.*, **44**, 366684. 39

Zumpano, G. & Meo, M. (2008). Damage localization using transient non-linear elastic wave spectroscopy on composite structures. *International Journal of Non-Linear Mechanics*, **43 (3)**, 217–230. 33